

CASE FILE COPY

TECHNIQUES APPLICABLE TO MASS SPECTROMETRY OF GASEOUS TRACE CONTAMINANTS

F. G. Satkiewicz

J. A. Myer

P. Warneck



Bedford, Massachusetts

INTERIM REPORT
CONTRACT NO. NAS12-641

Prepared for
NATIONAL AERONAUTICS AND SPACE ADMINISTRATION
ELECTRONICS RESEARCH CENTER
CAMBRIDGE, MASSACHUSETTS

May 1969

GCA-TR-69-4-N

TECHNIQUES APPLICABLE TO MASS SPECTROMETRY
OF GASEOUS TRACE CONTAMINANTS

F. G. Satkiewicz
J. A. Myer
P. Warneck

GCA CORPORATION
GCA TECHNOLOGY DIVISION
Bedford, Massachusetts

INTERIM REPORT

Contract No. NAS12-641

Principal Investigator
P. Warneck

May 1969

Prepared for
NATIONAL AERONAUTICS AND SPACE ADMINISTRATION
Electronics Research Center
Cambridge, Massachusetts

TABLE OF CONTENTS

<u>Section</u>	<u>Title</u>	<u>Page</u>
	SUMMARY	1
I	INTRODUCTION	3
II	EXPLORATION OF A CRYOGENIC SAMPLE HOLDER FOR THE GCA MICROPROBE BEAM SPECTROMETER	4
	1. Introduction	4
	2. Experimental Cryogenic Sample Holder	4
	3. Energy Window	7
	4. Results of the Evaluation of the Cryogenic Sample Holder	7
	5. Conclusions	42
III	CHARGE TRANSFER MASS SPECTROMETRY	44
	1. Introduction	44
	2. Charge Transfer Source Design Criteria	46
	3. The Feasibility Model Charge Transfer Ion Source	48
	4. Experiment Results	52
	5. Conclusions and Recommendations	77
IV	RESONANCE SCATTERING FOR HIGH AND ULTRA- HIGH VACUUM PRESSURE GAUGE CALIBRATION	78
	1. Introduction	78
	2. Theoretical Considerations	79
	3. Feasibility Calculations	82
	4. Apparatus	83
	5. Light Sources	84
	6. Results	87
	7. Conclusions	95
	REFERENCES	99

TECHNIQUES APPLICABLE TO MASS SPECTROMETRY OF GASEOUS TRACE CONTAMINANTS

By Peter Warneck

GCA Corporation, GCA Technology Division
Bedford, Massachusetts

SUMMARY

(1) In an exploratory study, an experimental cryogenic target holder for the GCA prototype ion microprobe mass spectrometer was built and tested to evaluate its use in the analysis of condensed gases and vapors. The holder was cooled to temperatures of about -180°C . The materials investigated were CO_2 , NH_3 , H_2O , and heptane. Argon ions were used as the primary (sputtering) ions, and mass spectra of secondary ions were observed. Two methods of sample deposition were employed: (a) the continuous deposition of material directed at the cooled target by a hypodermic inlet, while sputtering, and (b) sample deposition onto the cooled target prior to sputtering. Complete coverage of the sputtering area with sample material was achieved only in the second case. When the coverage was incomplete, large signals of ions indicating interaction of sample with the substrate material (tantalum, gold, copper) were observed. With a complete coverage, ammonia and water vapor gave rise to prolific cluster ion formation. Heptane did not show this effect. The specificity of sample-substrate interaction may have significant analytical application.

(2) The application of charge transfer as a process for ionizing a gas sample in the ion source of a mass spectrometer was investigated. The charge transfer ion source consisted of a discharge source as the primary ion generator, an interaction chamber to which both primary ions and sample gas are admitted and extraction and focusing electrodes for the processing of the remaining primary ions and generated secondary (sample) ions. The intensities of the secondary ions increase with increasing primary ion currents, with increasing sample concentration and with increasing residence time of the primary ions in the interaction chamber. The source configuration investigated requires extraction fields of 5 volts/cm or higher. At lower field strength the extraction efficiency decreases. Sensitivities achieved with the source are of the order of 10^{-8} amps/torr for the gases and vapors; CO_2 , CS_2 , NH_3 , C_6H_6 , N_2O , SO_2 . The sensitivities are several orders of magnitude lower than those observed for electron impact sources; however, no pronounced disadvantage results from the lower sensitivities, since the applicable sample pressures can be higher.

Two major problems remain: One is the perturbing influence of air and moisture impurities in the carrier gas upon the composition of the primary ion beam. The other is ionization of sample gas by processes occurring in addition to charge transfer, mainly interaction of sample gas with the boundary of the primary ion discharge source. To overcome these difficulties,

the test design will have to be modified. However, the basic applicability of charge transfer as the source of ions in analytical mass spectrometry has been demonstrated.

(3) Resonance scattering from xenon of the 1470\AA xenon resonance line has been investigated with respect to its use as a calibration technique for ultra-high vacuum gauges. It is shown that a suitable light source is the most important component in the overall system, because the profile of the emitted line determines the effective resonance scattering cross section. Three different light sources were investigated and compared to evaluate their suitability to resonance scattering: (a) a small dc capillary light source, (b) an ac pulsed (Tanaka) source, and (c) a microwave powered source. Optimum operating conditions were determined for each source. The microwave source operated with a window close to the discharge region was found to produce optimal scattering signals. In conjunction with an EMR uv photomultiplier detector used in the pulse counting mode it would enable the detection of xenon down to pressures of 1.5×10^{-11} torr. An even lower detection limit is anticipated when a Bendix Channeltron multiplier detector is employed.

I. INTRODUCTION

This report describes the progress achieved under Contract No. NAS12-641, which involves a study on the detection of gaseous trace contaminants. The effort is divided into three tasks which involve different experimentation and hence, are pursued independently. These three work areas may be specified as follows: (1) the investigation of a cryogenic target holder for the GCA solids analysis mass spectrometer for the purpose of gas solidification and analysis, (2) a study of the feasibility of utilizing charge transfer as the source of sample ionization in a gas analytical mass spectrometer, and (3) a feasibility study for the use of resonance scattering as a means of pressure gauge calibration in the ultra-high vacuum region. In the present report these items are treated separately, in the order given above. Thus Section II describes an exploratory cryogenic sample holder and gives test results obtained by carbon dioxide, ammonia, water vapor, and heptane. Section III deals with the concept of a charge transfer mass spectrometer ion source, gives design criteria and construction details of such a source, and results of an experimental investigation into its suitability. Section IV derives theoretically the optimum conditions for resonance scattering, describes a suitable apparatus, including light sources and detectors and finally, presents results of a study devoted to optimizing light source operating conditions for the required application.

II. EXPLORATION OF A CRYOGENIC SAMPLE HOLDER FOR THE GCA MICROPROBE BEAM SPECTROMETER

1. Introduction

The ion microprobe solids analysis mass spectrometer developed at GCA has proven to be a useful and sensitive tool in the analysis of solids. The basic feature of this instrument is the bombardment of the sample's surface with an intense beam of noble gas ions, usually argon ions, generated in a duoplasmatron source. The resulting sputtering of sample material gives rise to secondary ions which are characteristic of the sample material. These secondary ions are mass analyzed in a double focusing mass spectrometer and are detected with an electron multiplier unit. In conventional operation, the instrument is not suited for the analysis of gases. Thus, it was of interest to determine the modifications required to make gas analysis with this instrument feasible. The most logical approach appeared to develop a cryogenic sample platform as the base for the condensation of gases or gas mixtures that were to be analyzed. Secondary ions resulting from sputtering the condensate could then be analyzed in the usual manner. The following sections of this report describe first an experimental cryogenic sample holder, then the results obtained with it using simple condensable gases such as carbon dioxide, ammonia, water vapor and heptane.

2. Experimental Cryogenic Sample Holder

The sample holder must fit between the support rods of the duoplasmatron beam analyzer plates (3/4-inch maximum spacing), and provide a surface at 45 degrees to the incident beam to accommodate the elliptical sputtering area of about 1 x 0.7 cm. If the condensate is to be sputtered off a substrate, the substrate should (1) be resistant to sputtering, (2) produce ions which will not interfere with those of the sample, and (3) have a good thermal conductivity to accommodate the heat input from the ion bombardment. Tantalum meets these conditions fairly well, except that its thermal conductivity is poor. Copper and gold have good thermal conductivities, but their sputtering rates are higher than that of tantalum. In the present work, all three materials were used at various stages.

The principal features of the experimental sample holder are shown in Figures 1 and 2. The cryogenic holder was mounted onto a flange similar to that of the target holder normally used with the prototype instrument so that a simple exchange was made possible. Isolation of the target voltage was accomplished by Kovar to glass seals. Cooling was effected by passing tank nitrogen gas through a copper coil immersed in liquid nitrogen and then through a small glass tube concentric with the Kovar-glass assembly. In this manner, temperatures of -170° to -180° were attained as verified by measurement with a thermocouple.

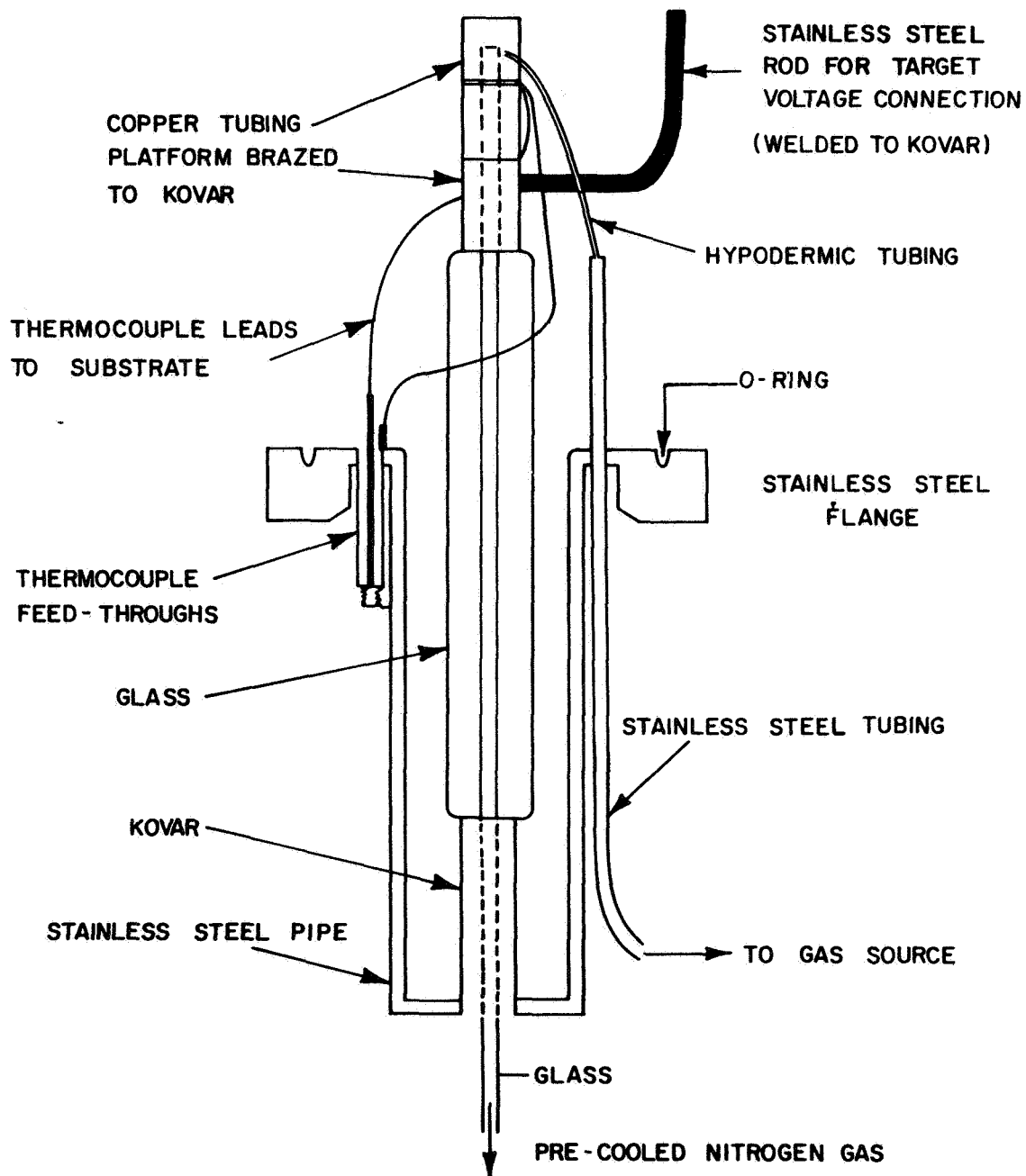


Figure 1. Cryogenic holder; side view.

018334-10E

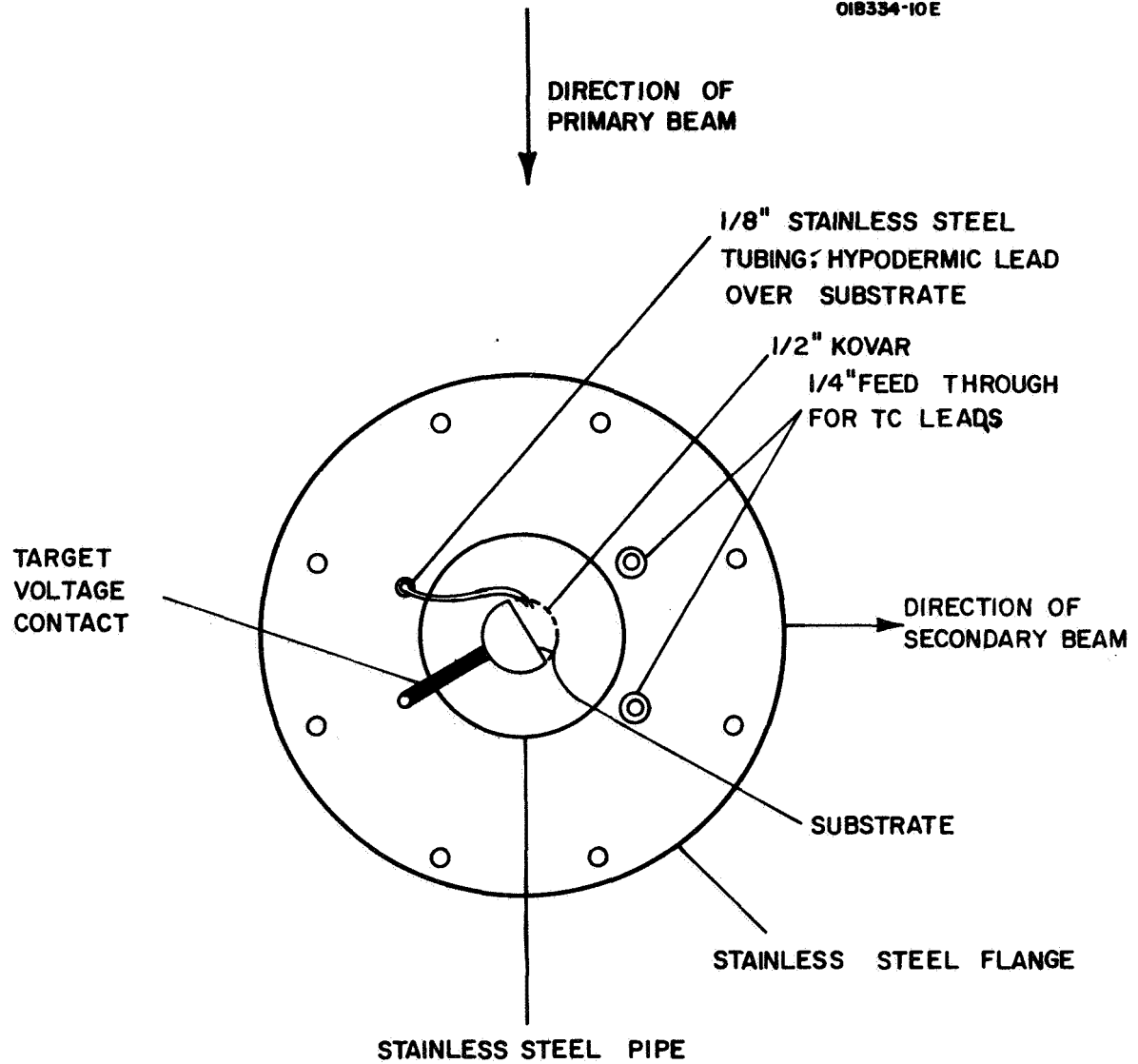


Figure 2. Preliminary cryogenic holder; front view.

In the initial experiments the gas or vapor to be studied was introduced through a stainless steel hypodermic tubing projecting into the cryogenic platform. In later experiments, the hypodermic manifold was removed and the sample gas was introduced into the target chamber directly with the pump valve closed, until a sufficient condensate had built up.

The target platform was copper sheet brazed to the Kovar cylinder. Onto the copper, a thin tantalum sheet was brazed. Subsequently, the tantalum was replaced by gold, and finally, in a series of experiments the copper platform was used directly. In all experiments, an argon ion beam was used. The beam was defocused to obtain a low sputtering rate and optimum heat dissipation.

3. Energy Window

In the following, use will be made of a specific feature of the GCA instrument, namely the selection of an "energy window" in the analysis of secondary ions. This term will be briefly discussed before the results are presented.

When the solid is sputtered, both neutral and ionized atomic and polyatomic fragments are generated. A study(Ref. 1) of the initial energies of the secondary ions for a number of species has shown that in general atomic ions have a broader energy distribution than polyatomic or molecular ions, i.e., a substantial number of atomic ions have high energies. This is shown in Figure 3 for Al^+ and Al_n^+ ions generated from the sputtering of an Al-Mg alloy with 12 keV Ar^+ . While the width of the energy band accepted by the mass spectrometer remains constant at 50 eV, one can select the average value of the accepted initial ion energies by an appropriate setting of the target holder potential. Thus, the mass analyses can be made to sample a 50 eV energy window along the energy distribution curve. This is shown as shaded areas in the figure. With the energy window at the lower initial ion energy portion of the distribution curves, polyatomic as well as atomic species are seen in the mass spectra. When the energy window is placed at the higher energy end of the curves, essentially only atomic ions are recorded in the spectra. By varying the energy window and following the intensity changes of selected peaks, interferences at certain masses can be evaluated, for example, $Si_2^+(56)$ versus $Fe^+(56)$. In addition, the polyatomic spectra provide an insight into bonding characteristics and with suitable calibrations can yield information about stoichiometry. In the following experiments, most of the spectra were obtained with the energy window set to $E_w = 0$ eV.

4. Results of the Evaluation of the Cryogenic Sample Holder

a. Carbon dioxide, simultaneous sputtering and sample deposition. - Figure 4 shows the effect of introducing a continuous flow of CO_2 through the hypodermic inlet over the nonrefrigerated Ta substrate. The secondary beam adjustments were such that a maximum intensity of the CO_2^+ peak was

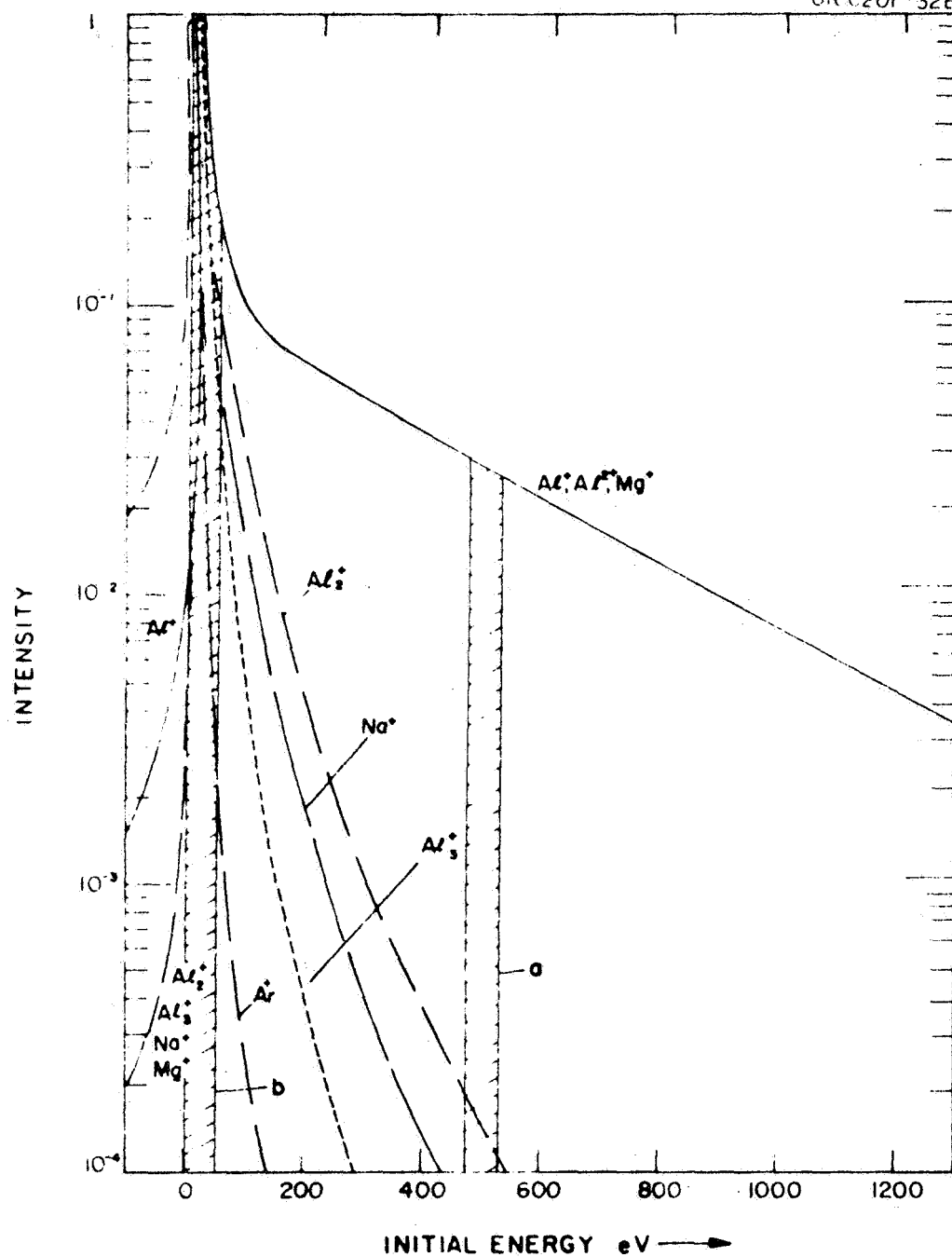


Figure 3. Energy distribution of Al^+ , Al^{2+} , Al_2^+ , Al_3^+ , Mg^+ , Na^+ , Ar^+ sputtered from an Al-Mg-alloy with 12 KeV Ar^+ . (All intensities normalized to "one".)

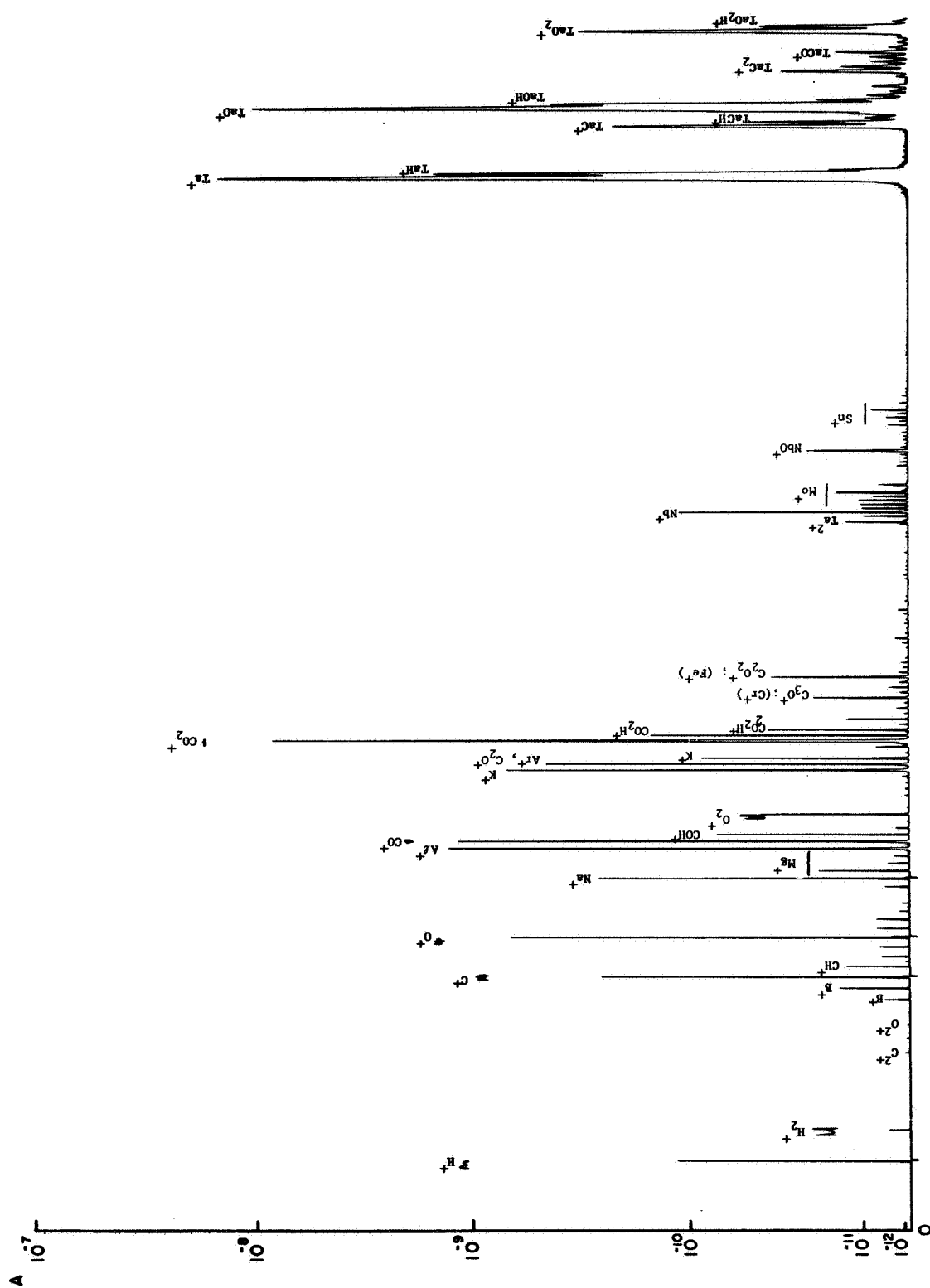


Figure 4. Polyatomic spectrum of carbon dioxide at $E_w = 0$ eV; (tantalum substrate above 25°C); 10 keV Ar^+ .

obtained. With the energy window set at 0 eV, the spectrum includes ions of thermal velocity. Figure 5 shows a similar spectrum obtained with an energy window of 20 eV, revealing a decrease of CO_2^+ , which is in accordance with expectation.

The spectrum in Figure 6 was obtained with CO_2 flow onto the refrigerated surface and the energy window at 0 eV. The presence of the substrate signal in the spectra indicates incomplete coverage of the substrate surface. That a significant interaction of CO_2 with the tantalum exists during sputtering in both the cryogenic and noncryogenic spectra is indicated by the large peaks due to TaO^+ , TaC^+ , TaC_2^+ , and TaCO^+ . In fact, the ratios of Ta^+ , TaO^+ , and TaO_2^+ almost correspond to those obtained in sputtering bulk Ta_2O_5 or tantalum in the presence of a high O_2 background. The cryogenic condition shows a significant increase in the TaCO^+ intensity which amounts to a seven-fold increase in the concentration of CO_2 at the surface. This "enrichment" factor is also evident in the ratios of the total intensities of the carbon-oxygen species taken at $E_w = 20$ eV for cryogenic and noncryogenic operation, shown in Table I. This table gives observed peak intensities for cryogenic and noncryogenic conditions as well as the intensity fractions of the species derived from CO_2 .

An examination of the 20-eV data shows no major differences in the polyatomic spectra in the noncryogenic versus cryogenic conditions indicating no appreciable intermolecular bonding forces exist between the CO_2 molecules chemisorbed or condensed on the tantalum surface.

To study the role of the substrate in the sputtering of carbon dioxide, the above experiments were repeated using gold as a substrate. For this purpose, the brazed tantalum sheet was removed from the cryogenic platform and a 0.005-inch thick gold foil applied to the copper substrate. Both surfaces were wetted with indium and pressed together subsequent to heating the assembly to the melting point of indium. Despite care, indium appeared in the spectra.

As previously, the carbon dioxide was introduced through the hypodermic manifold and a steady-state flow condition was maintained at a chosen pressure during the sputtering. Traces were taken at energy windows of 0 and 20 eV for both cryogenic and noncryogenic conditions. The spectra for the energy window set at 0 eV are shown in Figures 7 and 8. The intensities of the characteristic peaks were measured and are shown in Table II. Comparison of the sputtered ion intensity fractions for tantalum (Table I) and gold indicates less CO_2 interaction with gold. Ninety-two percent of the ion intensity associated with CO_2 on gold is CO_2^+ versus 62 percent for tantalum. The results suggest that ion fragments of CO_2 must originate mainly from CO_2 which is either condensed or chemisorbed on a solid surface, otherwise the ion intensity fractions would be the same in both cases.

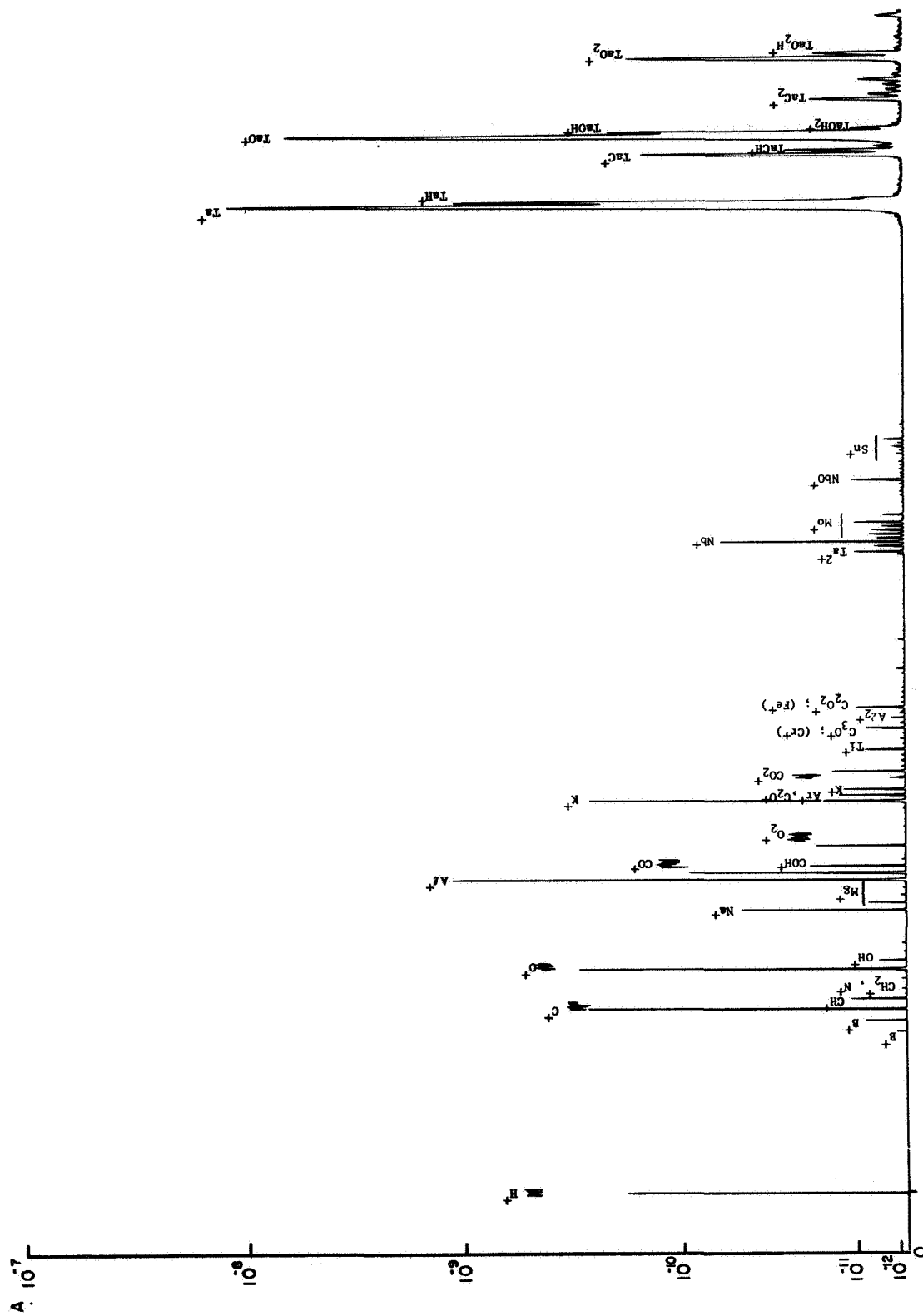


Figure 5. Polyatomic spectrum of carbon dioxide at $E_w = 20$ eV; (tantalum substrate above 25°C); 10 keV Ar⁺.

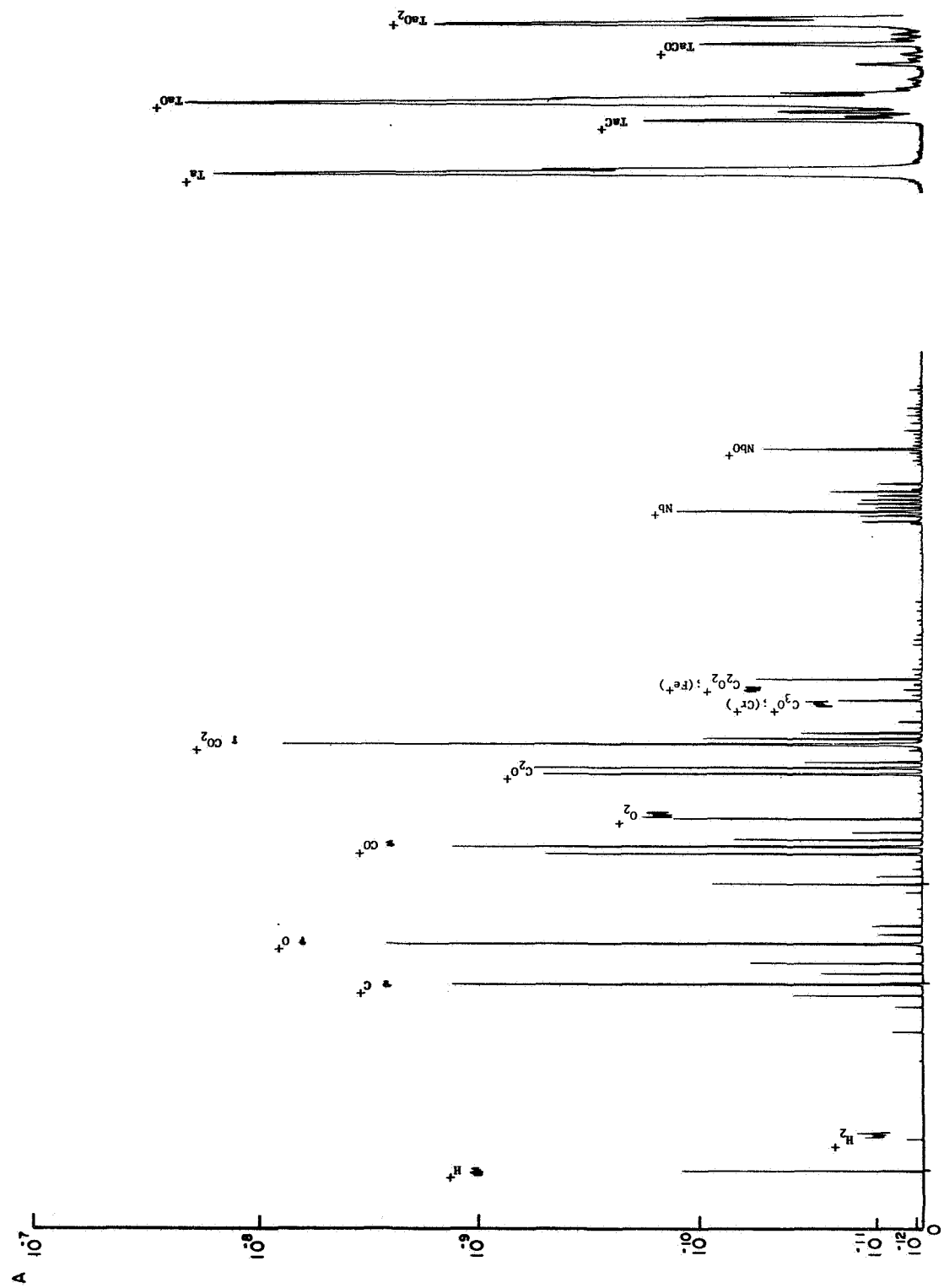


Figure 6. Polyatomic spectrum of carbon dioxide at $E_w = 0$ eV; (tantalum substrate at -170°C); 10 keV Ar^+ .

TABLE I

DISTRIBUTION OF IONS SPUTTERED FROM CARBON DIOXIDE ON A
TANTALUM SUBSTRATE; DEFOCUSED BEAM OF 10 keV Ar⁺

$E_w = 0 \text{ eV}$

Species, X ⁺	No Refrigerant; > 25°C		Refrigerant; - 170°C	
	$P_{\text{CO}_2} = 1.2 \times 10^{-6} \text{ mm}$		$P_{\text{CO}_2} = 1.1 \times 10^{-6} \text{ mm}$	
	$I_{\text{X}^+} \times 10^{10}$	$I_{\text{X}^+} / \Sigma I_{\text{X}^+}$	$I_{\text{X}^+} \times 10^{10}$	$I_{\text{X}^+} / \Sigma I_{\text{X}^+}$
C ⁺	9.0	0.066	27.0	0.11
O ⁺	14.0	0.10	65.0	0.25
CO ⁺	20.0	0.15	26.0	0.10
O ₂ ⁺	0.5	0.0037	1.5	0.0056
C ₂ O ⁺ (Ar ⁺)	4.5	0.033	5.5	0.021
CO ₂ ⁺	85.0	0.62	130.0	0.49
C ₃ O ⁺ (Cr ⁺)	0.23	0.0017	0.27	0.0011
C ₂ O ₂ ⁺ (Fe ⁺)	0.41	0.003	0.56	0.0022

$E_w = 20 \text{ eV}$

Species, X ⁺	No Refrigerant; > 25°C		Refrigerant; - 170°C	
	$P_{\text{CO}_2} = 1.2 \times 10^{-6} \text{ mm}$		$P_{\text{CO}_2} = 1.1 \times 10^{-6} \text{ mm}$	
	$I_{\text{X}^+} \times 10^{10}$	$I_{\text{X}^+} / \Sigma I_{\text{X}^+}$	$I_{\text{X}^+} \times 10^{10}$	$I_{\text{X}^+} / \Sigma I_{\text{X}^+}$
C ⁺	3.2	0.33	23.0	0.34
O ⁺	4.3	0.45	37.0	0.55
CO ⁺	1.2	0.13	3.0	0.045
O ₂ ⁺	0.28	0.029	0.42	0.0063
C ₂ O ⁺ (Ar ⁺)	0.14	0.015	0.37	0.0055
CO ₂ ⁺	0.25	0.026	2.7	0.040
C ₃ O ⁺ (Cr ⁺)	0.08	0.0083	0.09	0.0015
C ₂ O ₂ ⁺ (Fe ⁺)	0.1	0.01	0.20	0.003

NB. All spectra were obtained by adjusting secondary optics for maximum CO₂⁺ intensity.

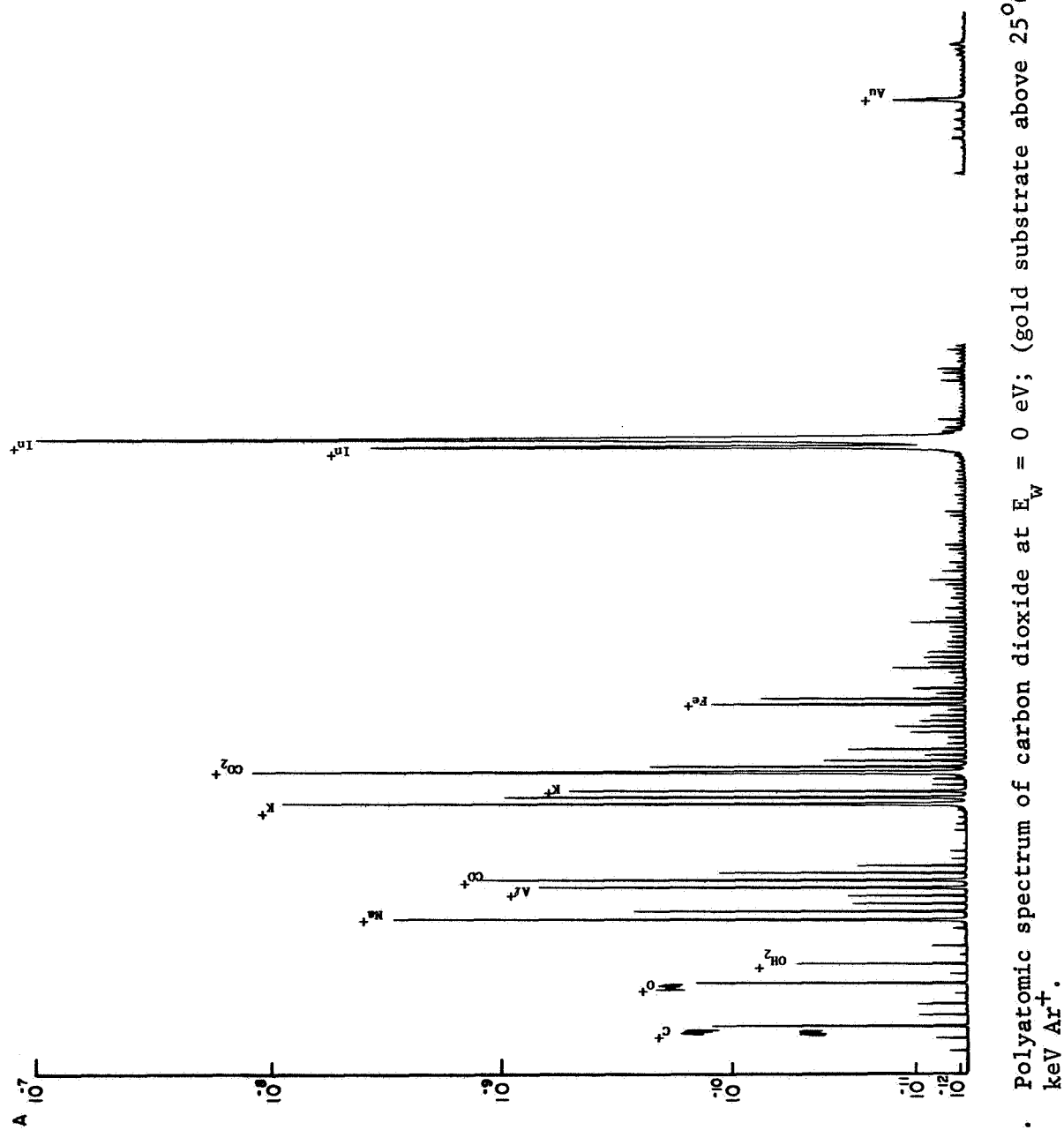


Figure 7. Polyatomic spectrum of carbon dioxide at $E_w = 0$ eV; (gold substrate above 25°C); 10 keV Ar^+ .

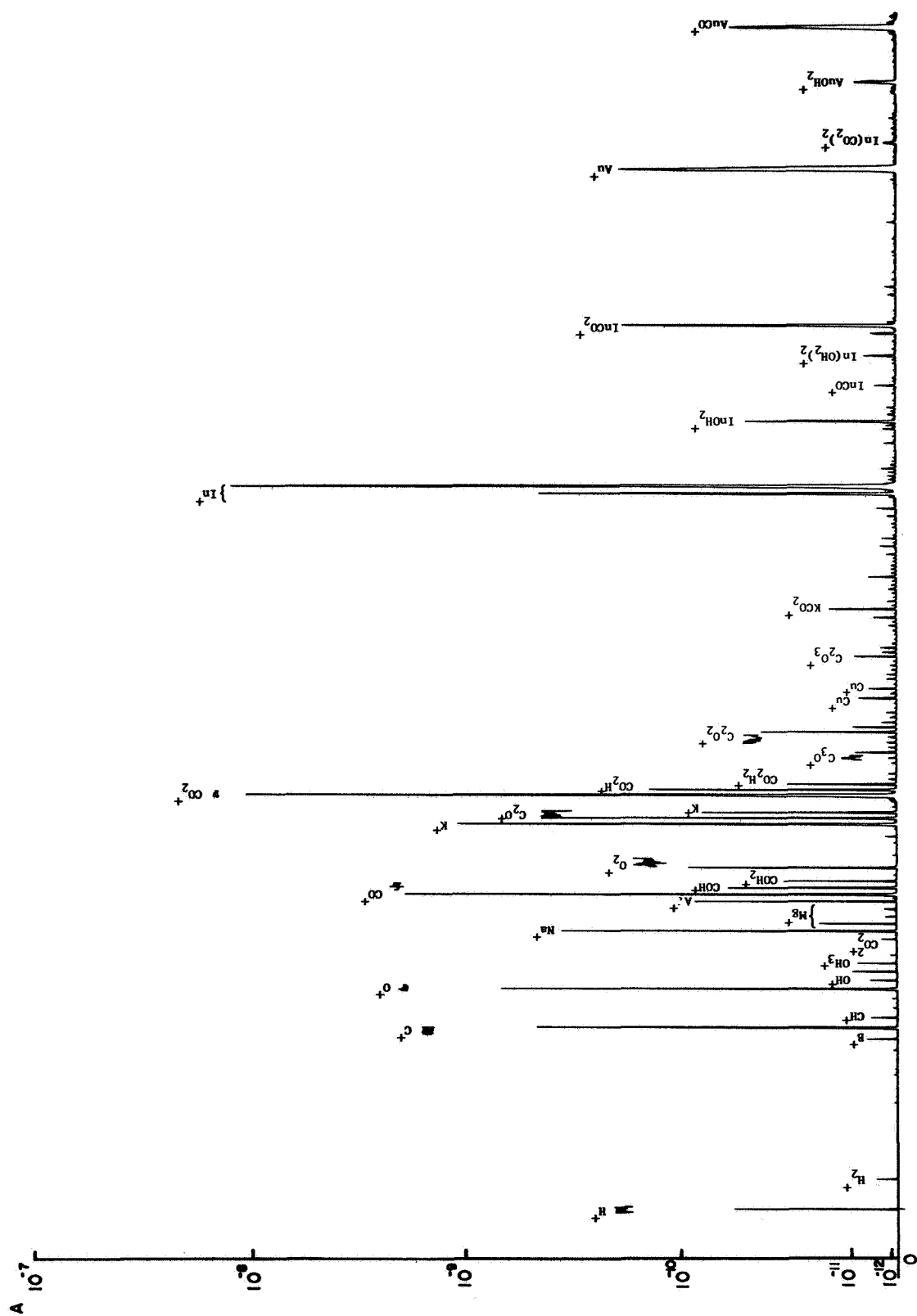


Figure 8. Polyatomic spectrum of carbon dioxide at $E_w = 0$ eV; (gold substrate at -170°C); 10 keV Ar^+ .

TABLE II

DISTRIBUTION OF IONS SPUTTERED FROM CARBON DIOXIDE ON A
GOLD SUBSTRATE; DEFOCUSED BEAM OF 10 keV Ar⁺

$E_w = 0 \text{ eV}$

Species, X ⁺	No Refrigerant;		Refrigerant;	
	$P_{\text{CO}_2} = 2 \times 10^{-6} \text{ mm}$ $I_{\text{X}^+} \times 10^{10}$	$I_{\text{X}^+} / \Sigma I_{\text{X}^+}$	$P_{\text{CO}_2} = 1.2 \times 10^{-6} \text{ mm}$ $I_{\text{X}^+} \times 10^{10}$	$I_{\text{X}^+} / \Sigma I_{\text{X}^+}$
C ⁺	1.0	0.007	16.0	0.072
O ⁺	1.4	0.01	20.0	0.09
CO ⁺	9.5	0.067	20.0	0.09
O ₂ ⁺	0.03	0.0002	1.4	0.006
C ₂ O ⁺ (Ar ⁺)	----	----	4.2	0.019
CO ₂ ⁺	130.0	0.92	160.0	0.72
C ₃ O ⁺ (Cr ⁺)	----	----	0.09	0.0004
C ₂ O ₂ ⁺ (Fe ⁺)	----	----	0.45	0.002
C ₂ O ₃ ⁺	----	----	0.09	0.0004

$E_w = 20 \text{ eV}$

Species, X ⁺	No Refrigerant;		Refrigerant;	
	$P_{\text{CO}_2} = 2 \times 10^{-6} \text{ mm}$ $I_{\text{X}^+} \times 10^{10}$	$I_{\text{X}^+} / \Sigma I_{\text{X}^+}$	$P_{\text{CO}_2} = 1.2 \times 10^{-6} \text{ mm}$ $I_{\text{X}^+} \times 10^{10}$	$I_{\text{X}^+} / \Sigma I_{\text{X}^+}$
C ⁺	----	----	20.0	0.48
O ⁺	----	----	18.0	0.43
CO ⁺	----	----	3.3	0.079
O ₂ ⁺	----	----	0.03	0.0007
C ₂ O ⁺ (Ar ⁺)	----	----	0.03	0.0007
CO ₂ ⁺	----	----	0.11	0.003
C ₃ O ⁺ (Cr ⁺)	----	----	0.03	0.0007
C ₂ O ₂ ⁺ (Fe ⁺)	----	----	0.08	0.002
C ₂ O ₃ ⁺	----	----	----	----

The role of primary energy in the distribution of sputtered species from CO_2 was examined with the energy window $E_w = 0$ eV. A constant flow of CO_2 and refrigerant was maintained. After each change in the primary voltage, readjustment of the secondary ion optics was made to obtain maximum CO_2^+ peak intensity. The results are shown in Figures 9 and 10. These figures show that the majority of the intensity fractions decrease with increasing energy. This is particularly true for C^+ and CO^+ . The intensities of CO_2^+ , however, increase. The most pronounced increase occurs in the CO_2^+ intensity fraction for gold on the substrate, which varies two orders of magnitude. Figure 10 shows that the intensity increase of the total ion intensity versus primary energy departs radically from linearity above 6 keV for the carbon dioxide gold system. The fact that the spectra obtained with $E_w = 0$ eV consist of peaks derived from sputtering of CO_2 condensed on the substrate, CO_2 chemisorbed on it, CO_2^+ formed by interaction with the vapor, makes it difficult to derive a detailed explanation for the observed behavior. In addition, it must be recognized that increasing the primary ion energy also increases the heat input to the sputtered sample. However, it is clear that lowering the primary ion energy does not decrease the amount of fragment ion formation as might be anticipated.

The specificity of gas-substrate interactions is demonstrated in Figure 8. The sputter ion yield for indium is larger than that of gold. The complexing of indium with H_2O , present either as a contaminant in the CO_2 or in the target chamber, is more pronounced than that with gold, whereas the formation of AuCO^+ is favored relative to InCO^+ . The InCO_2^+ complex is the major species in the indium interaction. Gold may act similarly but the corresponding peak was not in the observable mass range.

b. Ammonia, simultaneous sputtering and sample deposition. — Since carbon dioxide has a finite vapor pressure at -170°C , a more condensable gas was used next, to evaluate the cryogenic holder. Ammonia appeared to be a suitable choice.

The experiments were conducted with the gold substrate. Ammonia was introduced in the same manner as CO_2 and spectra taken under cryogenic and noncryogenic conditions were compared. The results are shown in Tables III, IV, and V and in Figures 11 and 12. The ease with which an H atom is removed from NH_3 is evidenced by the fact that NH_2^+ is the predominant species in the noncryogenic case. The presence of more complex polyatomic ions in the spectra suggests stronger intermolecular bonding forces in solid ammonia versus solid carbon dioxide.

The sum of the sputtered ion intensities of CO_2 and NH_3 are compared in Table III. A significant reduction of the NH_3 intensity is evident for the cryogenic case of NH_3 on gold. On the other hand, very large peaks of $[\text{Au}(\text{NH}_3)]^+$ and $[\text{Au}(\text{NH}_3)_2]^+$ are now observed. The much lower intensities of these species in the noncryogenic case may be attributed to the possibility that ammonia molecules impinging on the sputtered

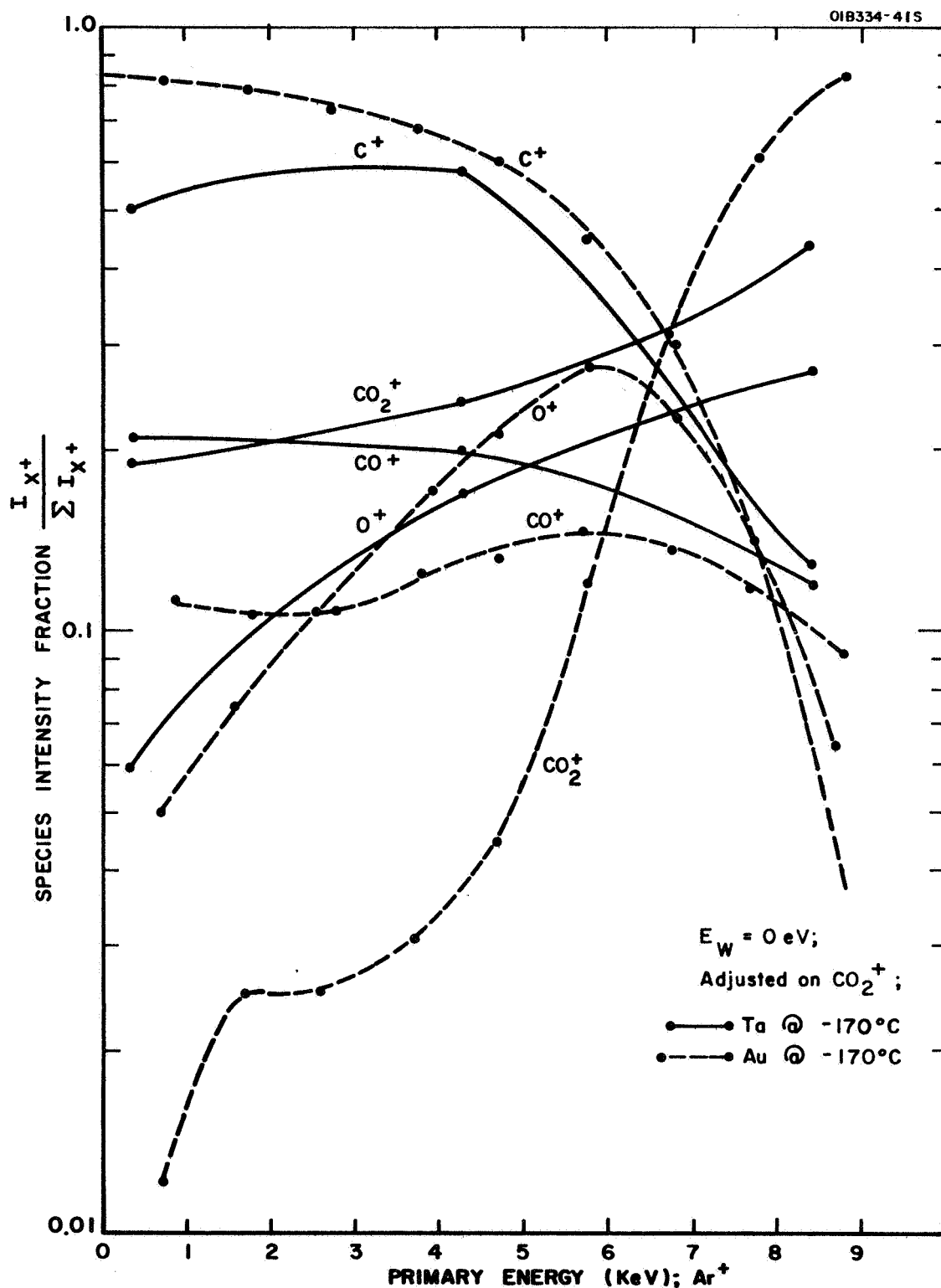


Figure 9. Distribution of species sputtered from solid CO_2 .

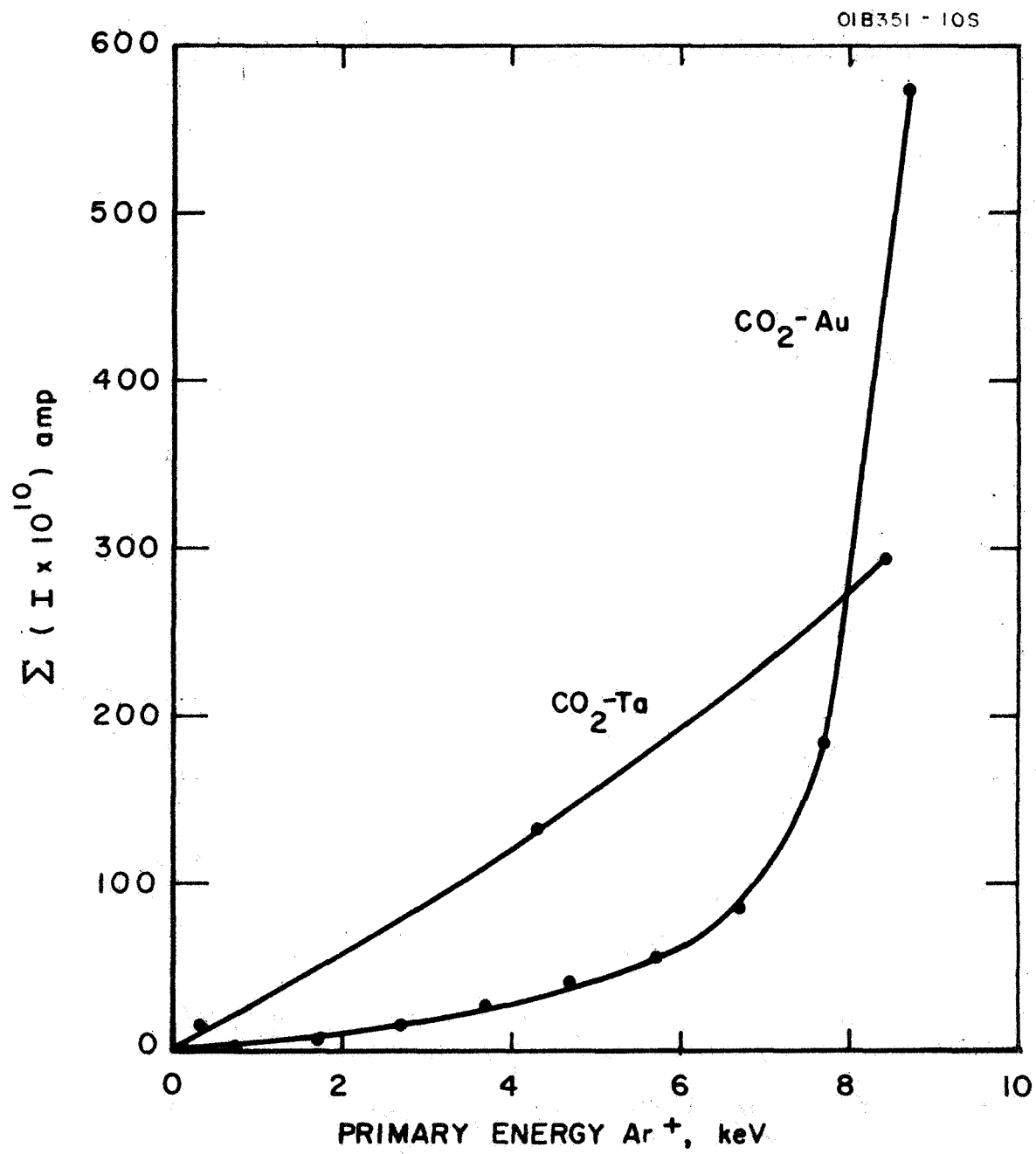


Figure 10. Total ion intensity from sputtered $\text{CO}_2(\text{s})$.

TABLE III

COMPARISON OF TOTAL ION INTENSITIES; $E_w = 0$ eV

System	Sum of Ion Intensities, $I \times 10^{10}$ amp	
	Noncryogenic	Cryogenic
Ta - CO ₂	134	256
Au - CO ₂	142	223
Au - NH ₃	1290	162

TABLE IV

DISTRIBUTION OF IONS SPUTTERED FROM AMMONIA ON A GOLD SUBSTRATE;
DEFOCUSED BEAM OF 10 keV Ar⁺; $E_w = 0$ eV; $P_{\text{NH}_3} = 1.3 \times 10^{-6}$ mm

Species, X ⁺	No Refrigerant		Refrigerant; $\sim -170^\circ\text{C}$	
	$I_{X^+} \times 10^{10}$	$I_{X^+} / \Sigma I_{X^+}$	$I_{X^+} \times 10^{10}$	$I_{X^+} / \Sigma I_{X^+}$
H ⁺	11.0	0.0009	~ 2.8	~ 0.02
H ₂ ⁺	8.5	0.0066	~ 3.4	~ 0.02
N ⁺	3.0	0.0023	1.5	0.0093
NH ⁺	3.5	0.0027	0.45	0.0028
NH ₂ ⁺	680.0	0.54	27.0	0.17
NH ₃ ⁺	310.0	0.24	25.0	0.15
NH ₄ ⁺	2.4	0.0019	11.0	0.068
N ₂ ⁺	270.0	0.21	90.0	0.56
N ₂ H ⁺	1.3	0.0001	0.760	0.0047

NB. All spectra were obtained by adjusting for maximum NH₂⁺ intensity.

TABLE V

DISTRIBUTION OF IONS SPUTTERED FROM AMMONIA ON A GOLD SUBSTRATE;
 DEFOCUSED BEAM OF 10 keV Ar^+ ; $E_w = 25\text{-}40$ eV; $P_{\text{NH}_3} = 1.3 \times 10^{-6}$ mm

Species, X^+	No Refrigerant		Refrigerant; $\sim -170^\circ\text{C}$	
	$I_{X^+} \times 10^{10}$	$I_{X^+} / \Sigma I_{X^+}$	$I_{X^+} \times 10^{10}$	$I_{X^+} / \Sigma I_{X^+}$
H^+	0.95	0.79	1.5	0.59
H_2^+	----	----	0.05	0.019
N^+	0.13	0.11	0.28	0.11
NH^+	0.08	0.066	0.42	0.16
NH_2^+	0.04	0.033	0.25	0.10
NH_3^+	0.005	0.004	0.12	0.047
NH_4^+	----	----	0.03	0.012
N_2^+	0.005	0.004	0.012	0.0047

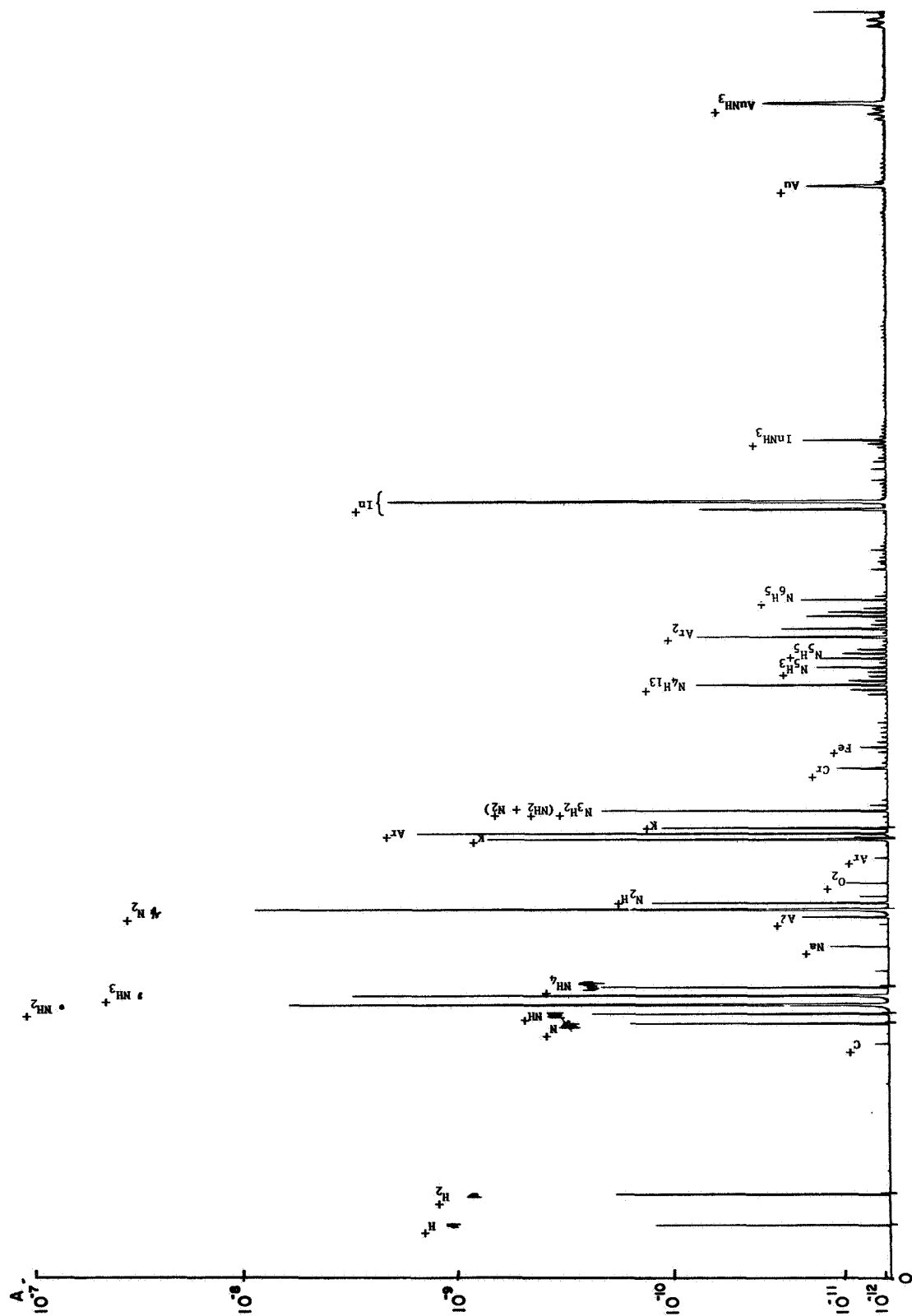


Figure 11. Polyatomic spectrum of ammonia; $E_w = 0$ eV; (gold substrate at approximately 30°C); 10 keV Ar^+ .

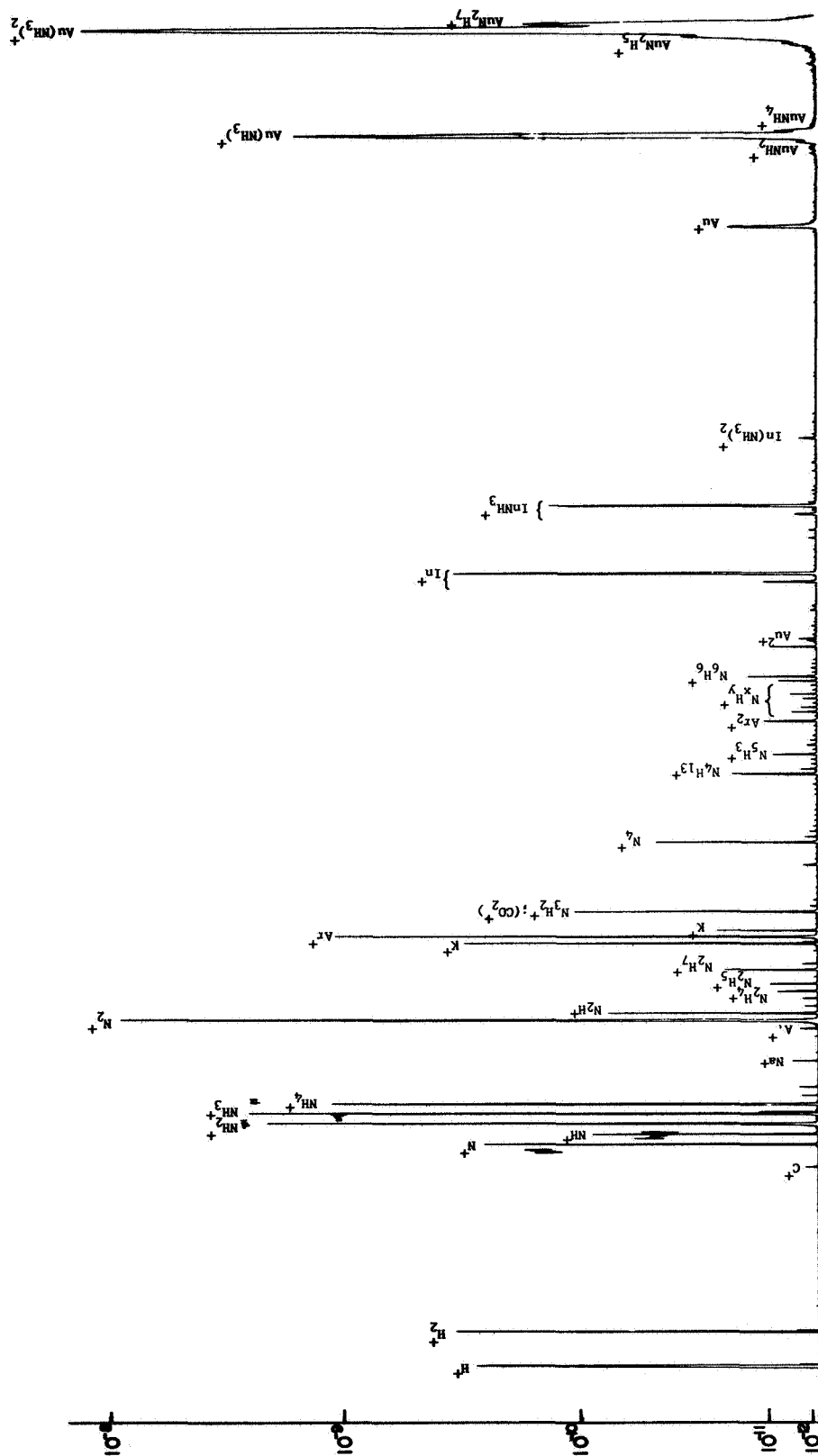


Figure 12. Polyatomic spectrum of ammonia at $E_w = 0$ eV; (gold substrate at -170°C); 10 keV Ar^+ .

substrate are not chemisorbed but fragmented and the fragments do not associate to any degree with the sputtered gold ions or atoms or with the gold surface. The possibility of fragmentation or dissociation may explain the very large N_2^+ intensities observed in the spectra. The N_2^+ peak decreases upon refrigeration which makes it unlikely that it is due to gaseous ammonia cluster formation. The absence of a significant O_2^+ peak also indicated that N_2^+ does not result from an interaction with residual air in the target chamber. If the N_2^+ ions result from the fragmentation of ammonia at the substrate surface, far less fragmentation or dissociation should occur at lower temperatures due to the build up of a chemisorbed phase on the gold. Sputtering of such a surface would then yield the complex ions directly, with a resulting decrease in the N_2^+ peak.

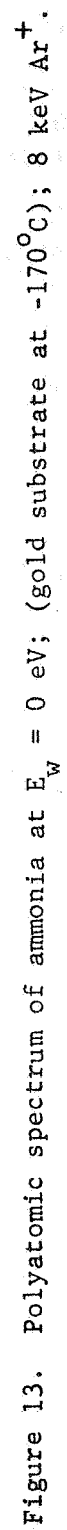
Similar to CO_2 , a small shift in the energy window towards higher initial energies showed the expected change in ion distribution to atomic and simple polyatomic ions such as H^+ , N^+ , and NH^+ , as is evident from Table V.

As previously stated, substrate peaks were present in all spectra indicating that the sputtered area was incompletely covered with condensate despite a constant flow of the gas over the cryogenic holder.

c. Ammonia, sputtering subsequent to sample deposition. — To improve the coverage of the target area with condensate, the hypodermic inlet was removed and in subsequent experiments the gas or vapor was deposited onto the refrigerated sample holder prior to the sputtering experiment. For this purpose the valve isolating the target chamber from the pump was closed and the sample gas was introduced to the chamber for some time until a sufficient deposit had been achieved. The gas or vapor source was then turned off, pumping was resumed and the sputtering process commenced. It is of interest to note that elimination of the hypodermic inlet also eliminated a possible perturbation of the electric field sampling the ions because the inlet was at ground potential, whereas the target area and the adjacent focusing elements are kept at higher potentials.

Immediately following the change in procedure, a spectrum of ice was taken which will be discussed subsequently. With ammonia, difficulties were experienced due to arcing. Nevertheless, a spectrum could be obtained which is shown in Figure 13. This spectrum shows some difference when compared to the equivalent spectrum obtained with dynamic gas flow conditions (Figure 12), particularly with respect to N_2^+ and NH_3^- gold complexes. However, because of the experimental difficulties present, additional modifications of the target holder were applied and the differences in the spectra were not further investigated.

The excessive arcing was determined to be caused by the proximity of the target holder to other electrodes nearby. A high vapor pressure of ammonia due to insufficient thermal conduction of the target substrate



probably contributed to the problem. Hence, the cryogenic efficiency for condensing ammonia was improved by removing the gold substrate thereby exposing the copper base. A thorough cleaning removed remaining impurities. To minimize the fields responsible for the arcing, the cryogenic platform was moved back so that spacing to the ion extraction electrode was increased. Also, all sharp edges of the holder were rounded off.

The copper platform was sputtered first without refrigerant to establish the background (or substrate) composition. Ammonia was then introduced under dynamic flow conditions ($P_{\text{NH}_3} = 2 \times 10^{-6}$ mm) into the target chamber, and the spectrum from interaction of Cu and NH_3 was established for noncryogenic operation. The resulting gas-solid interaction spectrum is shown in Figure 14. A number of Cu- NH_3 complex polyatomic ions can be seen. The ion intensity distribution is shown in Table VI along with the distribution previously found for NH_3 on Au. A significant difference is evident, particularly in the H^+ intensity. It is noteworthy that this is the largest H^+ intensity observed in our experience in sputtering a large number of compounds including AlH_3 . The spectrum reveals a high degree of chemical interaction. Visible evidence for reaction was noticed later when the copper platform was removed from the target chamber. A black deposit in the sputtering zone was evident as well as underneath the copper platform. Since the primary ion beam delivered a few watts and since the copper platform is thermally insulated in a vacuum, the temperature of the copper holder could be well above 30°C . Thus, the role of substrate temperature in the observed interaction is unresolved. Nevertheless no deposit was observed on the top of the copper platform adjacent to the sputtered area. Following the gas-solid interaction experiment, the substrate was cooled and spectra taken while sputtering without admission of NH_3 . Examination of these spectra reveal increased intensities of N^+ , O^+ , O_2^+ , N_2^+ , and Ar^+ and the presence of Cu- NH_3 and Cu- O_2 - H_2O complexes. The former indicates the increased concentration of background gas accommodated on the refrigerated surface, and the latter the residue of substrate surface reactions which took place with the noncryogenic gas-solid experiment.

Ammonia was introduced into the evacuated but isolated target chamber until a visible coating of solid NH_3 was observed; the flow was then shut out and the sputtering recommenced. In the first trials, scanning from mass 1 to 65 showed many sputtered NH_3 peaks, but the presence of large Cu^+ peaks indicated either that the coverage was still incomplete or that the NH_3 sputtered away or volatilized very quickly. Accordingly, the NH_3 loading was increased. The evidence of substantial peak intensities in the higher mass range indicated deposition consistent with complete coverage. Secondary beam adjustments were made until steady peaks were observed, whereupon spectra were taken. The result is shown in Figures 15a and b. The scale of the abscissa was expanded to show the peaks more clearly. In addition, the acceleration voltage was lowered to extend the mass range.

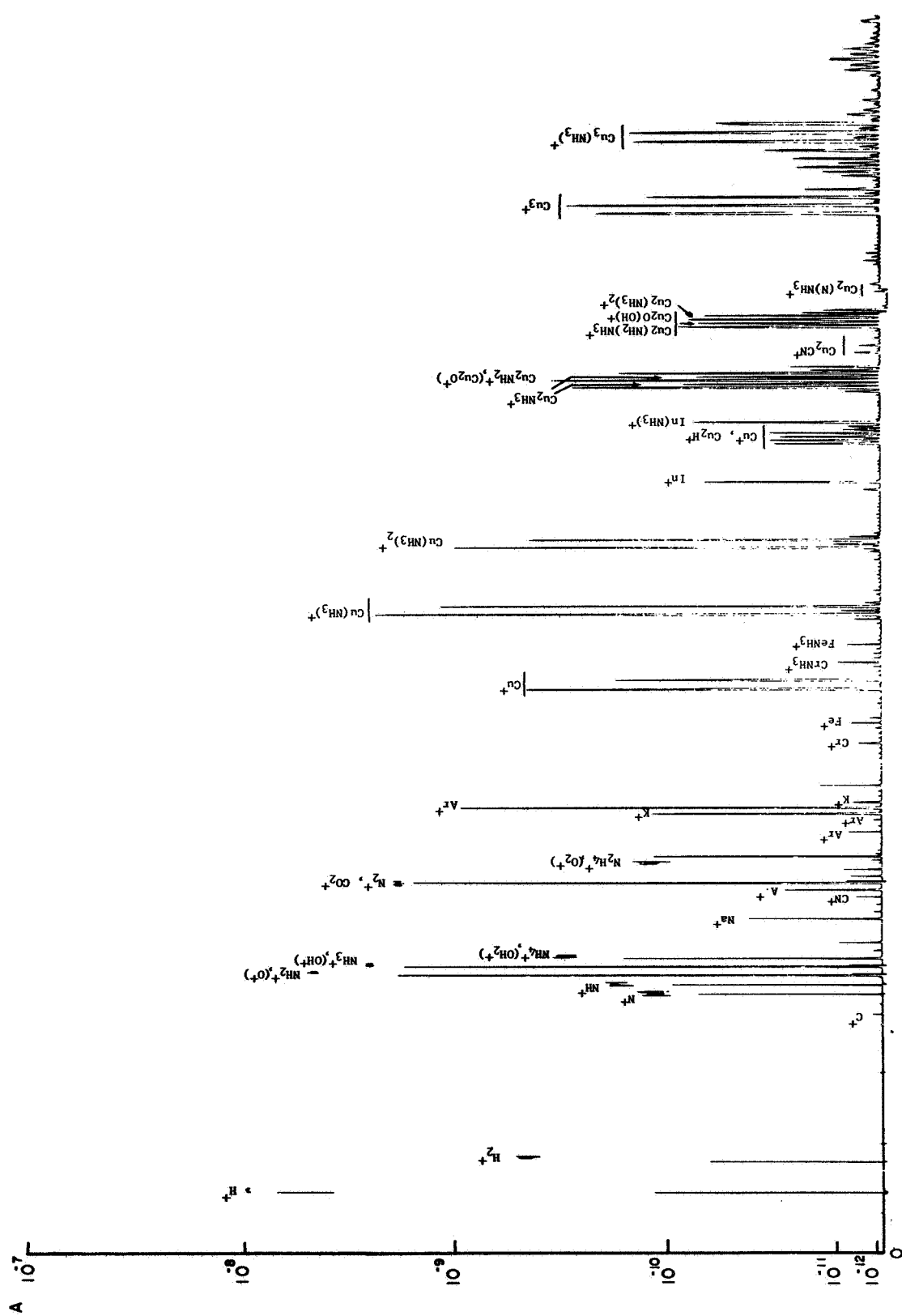


Figure 14. Polyatomic spectrum of ammonia at $E_w = 0$ eV; (copper substrate above 25°C); 10 keV Ar^+ .

TABLE VI

DISTRIBUTION OF IONS SPUTTERED FROM AMMONIA (COPPER SUBSTRATE);
 DEFOCUSED BEAM OF 10 keV Ar^+ ; $E_w = 0$ eV; $P_{\text{NH}_3} = 2 \times 10^{-6}$ mm

Species, X^+	No Refrigerant $I_{X^+} \times 10^{10}$ amps	$\left(\frac{I_{X^+}}{\Sigma I_{X^+}} \right)_{\text{Cu}}$	$\left(\frac{I_{X^+}}{\Sigma I_{X^+}} \right)_{\text{Au}}$
H^+	100.0	0.48	0.0009
H_2^+	4.7	0.023	0.0066
N^+	1.2	0.0058	0.0023
NH^+	1.8	0.0087	0.0027
NH_2^+	50.0	0.24	0.54
NH_3^+	27.0	0.13	0.24
NH_4^+	3.1	0.015	0.0019
N_2^+	19.0	0.092	0.21
N_2H^+	0.06	0.0003	0.0001

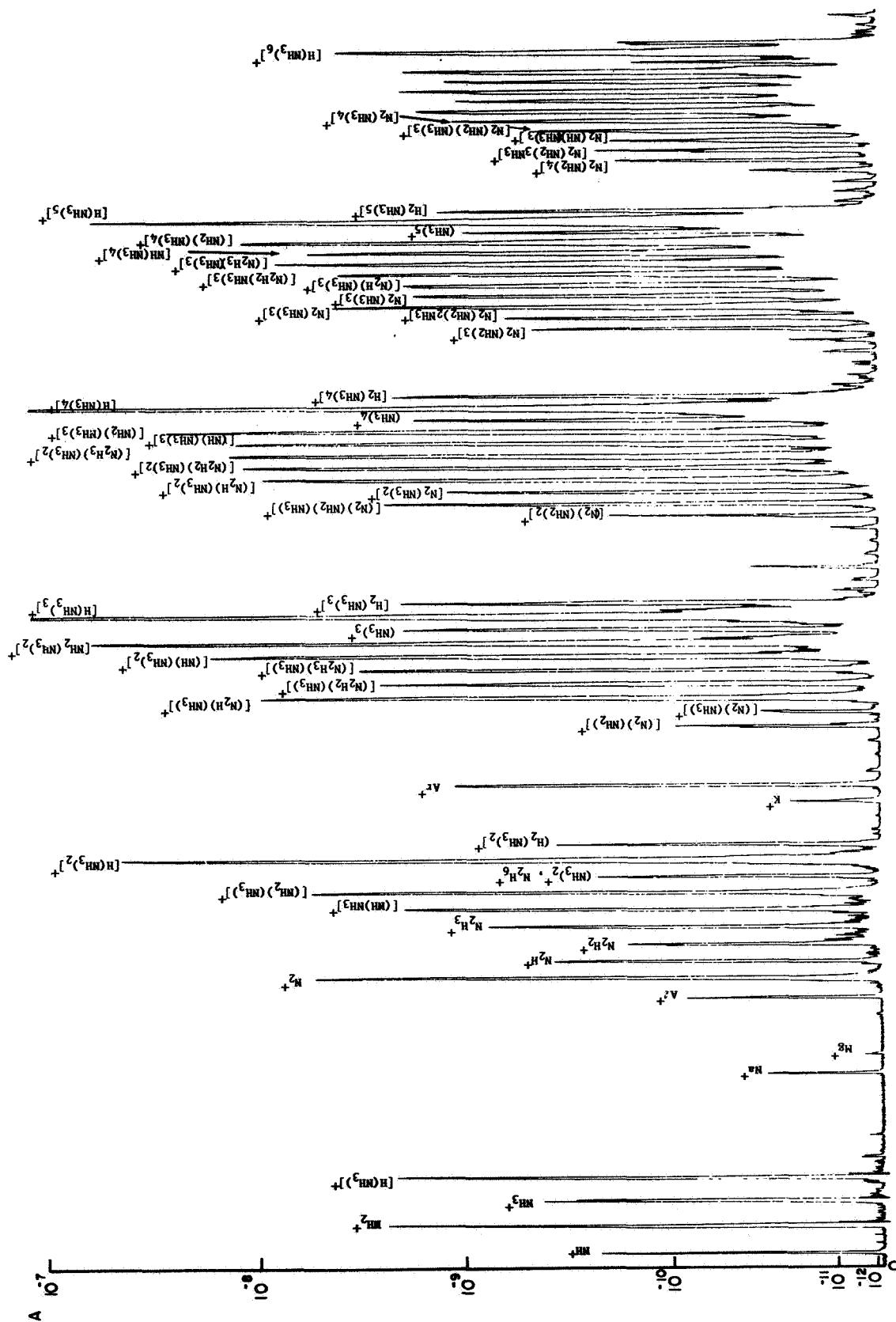


Figure 15a. Polyatomic spectrum of ammonia at $E_w = 0$ eV; (copper substrate at -170°C); 7 keV Ar^+ .

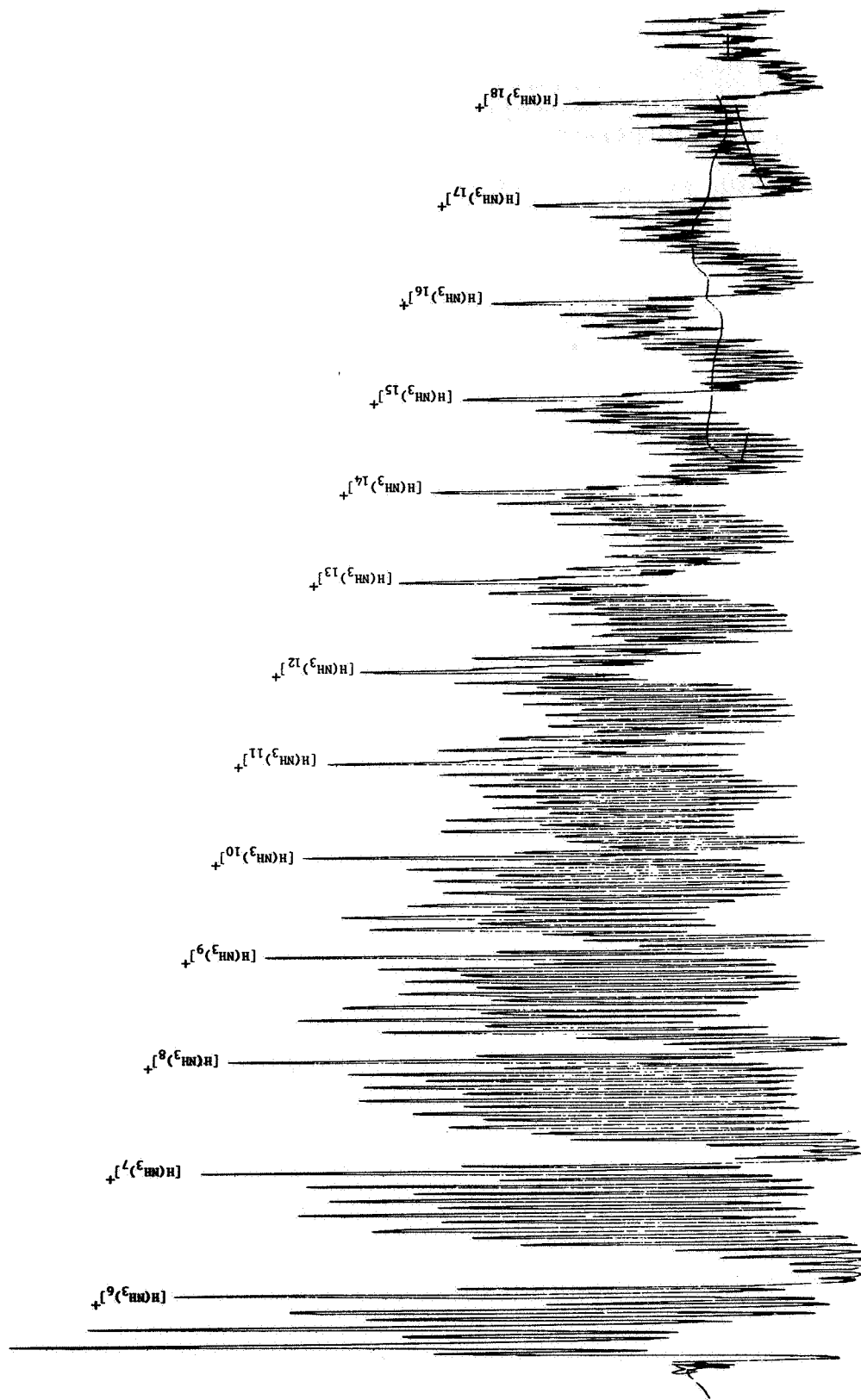


Figure 15b. Polyatomic spectrum of ammonia at $E_w = 0$ eV; (copper substrate at -170°C); 7 keV Ar^+ .

The peaks were identified and labeled to the point where obvious periodicity was established involving additional NH_3 molecules and sputtered fragments. The specific designation of each peak was made with reference to fragment units which appeared in the highest intensity at the lower masses. Thus the mass peak at 76 amu was identified as $[\text{N}_2(\text{NH}_2)_3]^+$ rather than $(\text{N}_3(\text{NH}_3)_2)^+$, since no N_3^+ peak was observed at mass 42 whereas the NH_2^+ and N_2^+ peaks have considerable intensity. The identification of this particular peak as $[(\text{N}_2)(\text{NH})(\text{NH}_2)(\text{NH}_3)]^+$ appears unlikely. In Figure 16 the intensities of the $[\text{H}(\text{NH}_3)_X]^+$ species are plotted against the cluster number X. No correction was made for the effect of ion mass on the response of the ion multiplier detector although a correction would tend to raise the intensities at higher masses. The rather remarkable intensities and the slow decay with increasing mass of these fragments preclude formation of these species in a gaseous phase.

The change in the spectra when refrigerant flow was stopped was followed while observing the target chamber pressure. A change in the nature of the sputtered species was observed. (See Figure 17) The characteristic protonated polymolecular complexes have almost disappeared (i.e. $[\text{H}(\text{NH}_3)_3]^+$ etc.), but substrate - NH_3 fragment complexes are present in large intensities. This behavior differs from the ice-gold substrate case discussed below where showthrough of the substrate did not disturb the protonated polymolecular water complexes. This provides additional evidence for the chemical activity of copper and ammonia. The drastic change in the spectrum also evidences that the ion adducts $[\text{H}(\text{NH}_3)_X]^+$ are sputtered from the solid, since the surface concentration of ammonia was still large as the ammonia was being vaporized.

d. Ice, sputtering subsequent to sample deposition. - Although it appears that complicated polyatomic spectra arise from sputtering condensed phases, the possibility of identifying molecular species in polycomponent gas mixtures through complexes derived from substrate-gas interaction warranted further investigation. Since water is the major condensable in practical systems, its role as a substrate with respect to the other condensables was examined.

Water was introduced onto the cryogenic holder covered with the gold substrate, using the modified approach already outlined. After loading from an external source, sputtering was started. Charge-up of the ice occurred, manifested by fluctuations in peak intensities. Such variations normally occur when a variable surface charge exists. This condition stabilized with time and the spectrum shown in Figure 18 was obtained. Its examination shows an extensive proliferation of hydrated protons. Also the lack of substrate signal indicated that a complete coverage of the target substrate was achieved. It is apparent that the presence of so many polyatomic ions precludes its use as a substrate.

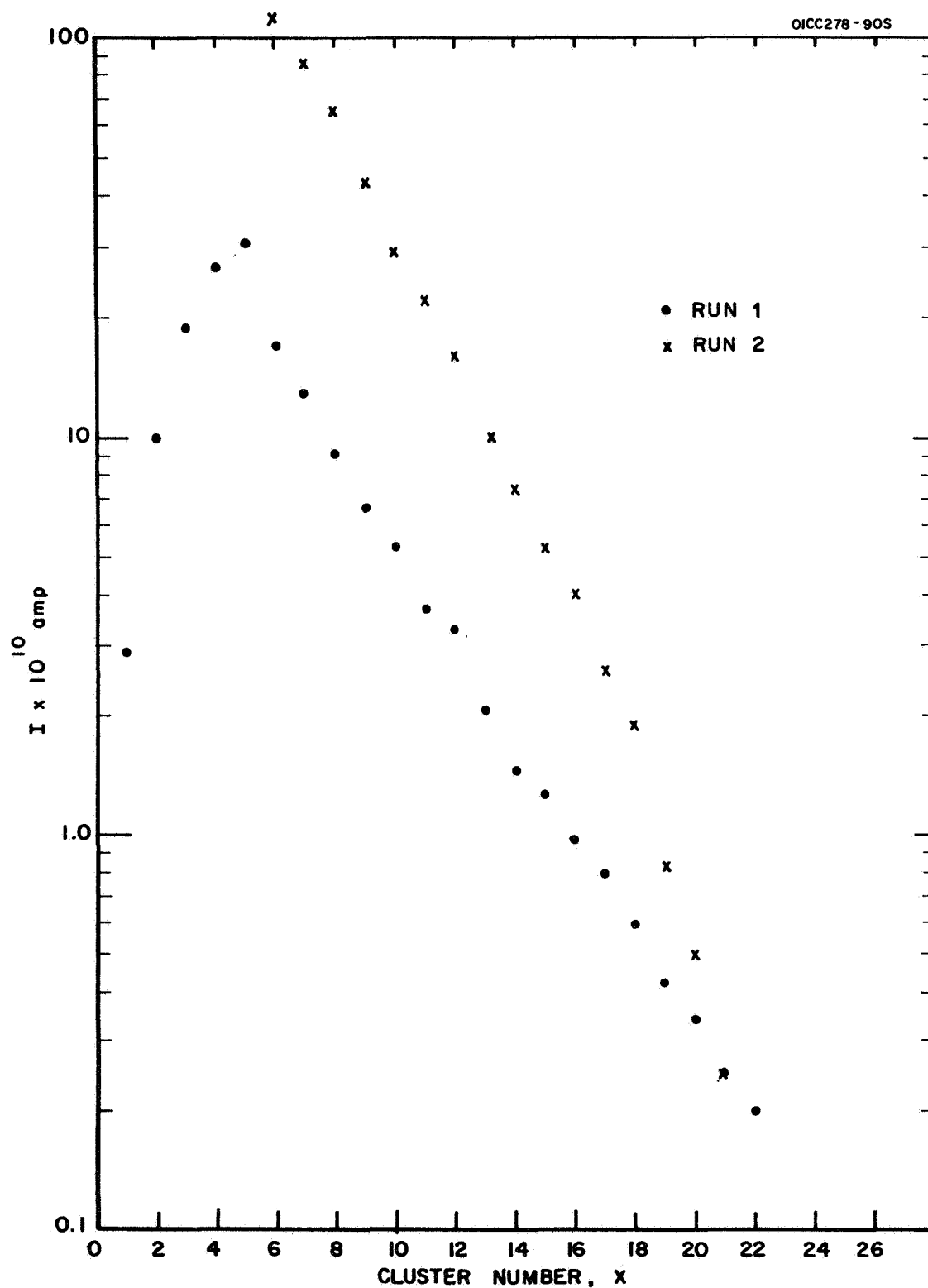


Figure 16. Cluster intensity of $[\text{H}(\text{NH}_3)_x]^+$ vs cluster number.

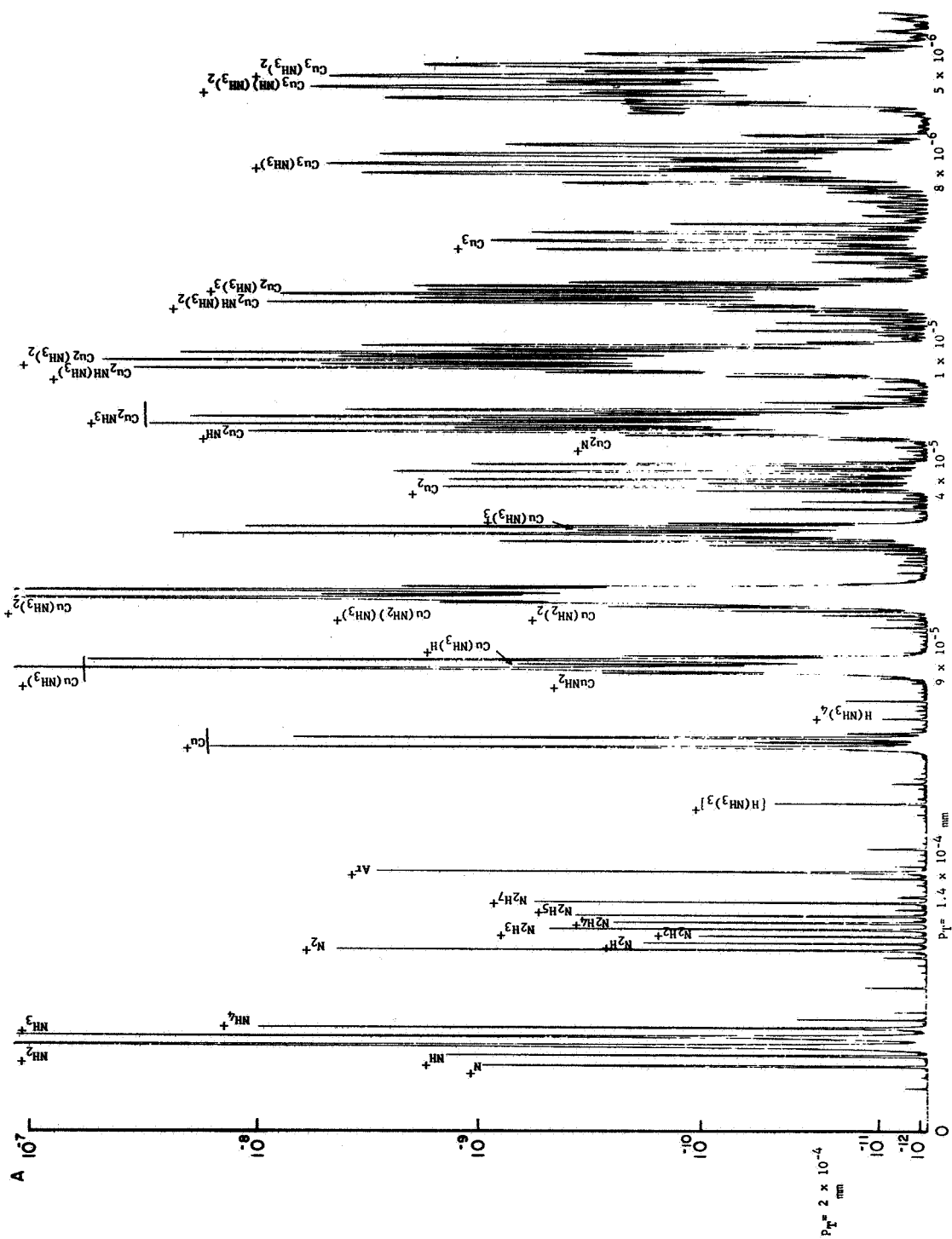
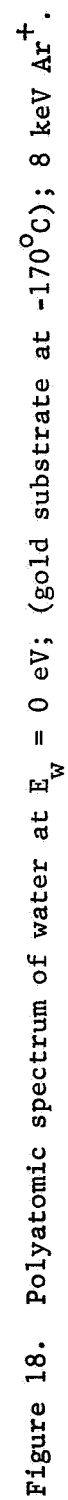


Figure 17. Polyatomic spectrum of ammonia with termination of cryogenic condition (copper substrate).



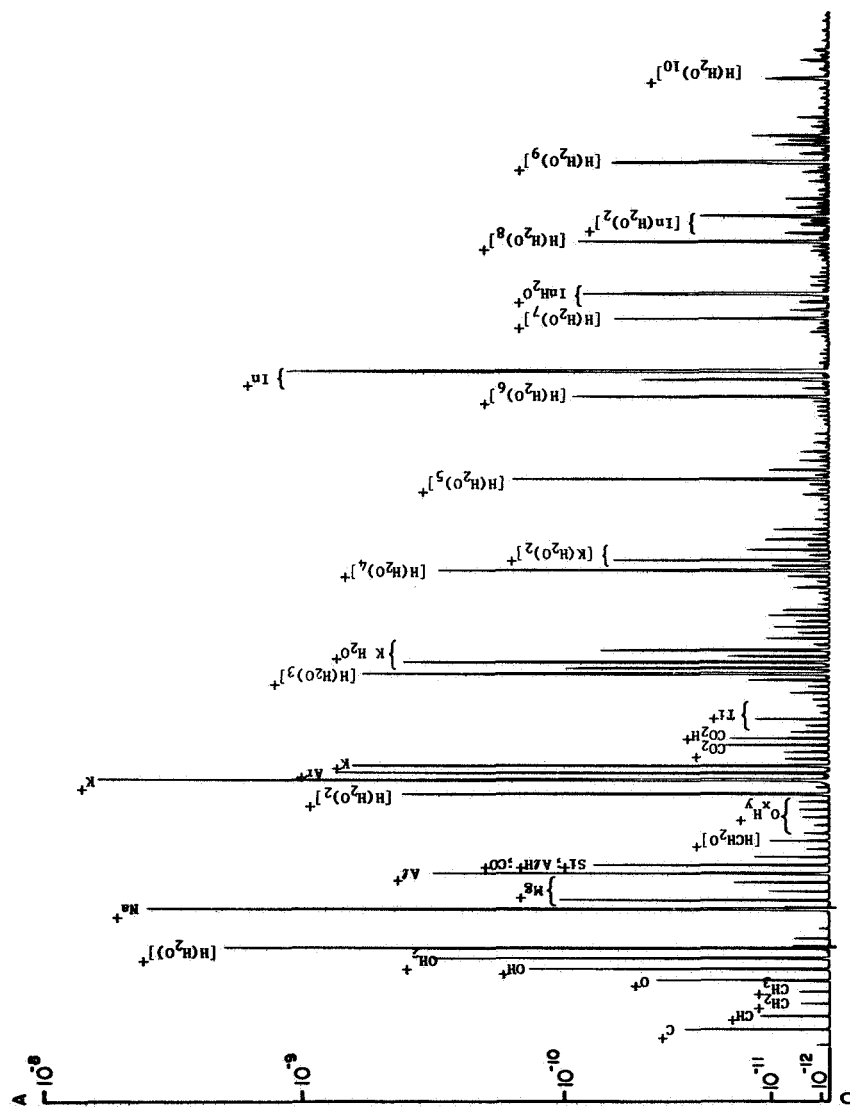
As the ice was sputtered, substrate was exposed; Figure 19 is a spectrum obtained under these conditions. The ice species are still evident, but complexes with the substrate such as KH_2O^+ , InH_2O^+ have also appeared. Milne and Greene (Ref. 2) have observed water clustering in "wet" argon following adiabatic expansion through nozzles. The isentropic temperature in their experiment was calculated to be 3.2°K . The clusters were $(\text{H}_2\text{O})_X$ or $(\text{H}_2\text{O})_X^+$ upon subsequent ionization. Their cluster intensities versus cluster number are very similar to those obtained by sputtering ice as shown in Figure 20. The common denominator here is that in both experiments the vibrational and rotational degrees of freedom were reduced. Accordingly, it is indicated that the prerequisite for cluster formation is indeed a low temperature, and not just a simple evaporation of ice.

The spectrum of ice shown in Figure 18 may be useful in rationalizing the presence of molecules such as H_3O^+ and H_5O_2^+ in the D-region. In a recent paper, Narcisi (Ref. 3) discusses mechanisms that have been proposed for explaining the presence of ice crystals in this region. Impacts between cosmic rays and ice crystallites could result in many ions.

In the present laboratory experiment, argon ions of high energy have revealed a specific fragmentation pattern. It appears likely that an analogous situation is occurring in the D-region. The peak-intensity ratios of H_3O^+ and H_5O_2^+ measured in the ionosphere are not very different from the ratios observed in the sputtering experiments. Unfortunately, the spectrometer used in the ionosphere experiment did not cover the next hydrate at mass 55. It would be of interest to sputter ice with 2 keV protons to make a more analogous comparison to high-energy particles expected in the ionosphere.

e. Heptane, sputtering subsequent to sample deposition. - The sputtering of heptane was investigated with the copper substrate to determine the role of the dipole moment in the formation of substrate complexes as well as the origin of the sputtered species from the solid state. As previously the spectrum of the vapor-substrate system was obtained first without refrigerant flow. It is shown in Figure 21. Although the heptane fragmentation pattern is observed, there is no evidence of substrate-heptane or heptane fragment complexes. The production of ion fragments may arise from collisions with the sputtered copper surface, or fragmentation from the interaction with the primary beam. The lack of specific complexes with the substrate is noteworthy as it precludes the possibility of utilizing this aspect in the analysis of condensable hydrocarbons.

Heptane was then condensed according to the outlined procedures, and sputtered; a typical spectrum is shown in Figure 22. The distribution of fragments is quite different from that shown in Figure 21 (see Table VII). In particular the intensities of C^+ , C_2^+ , C_3^+ , etc. are much higher and their distribution is reminiscent of the graphite spectrum. The relative



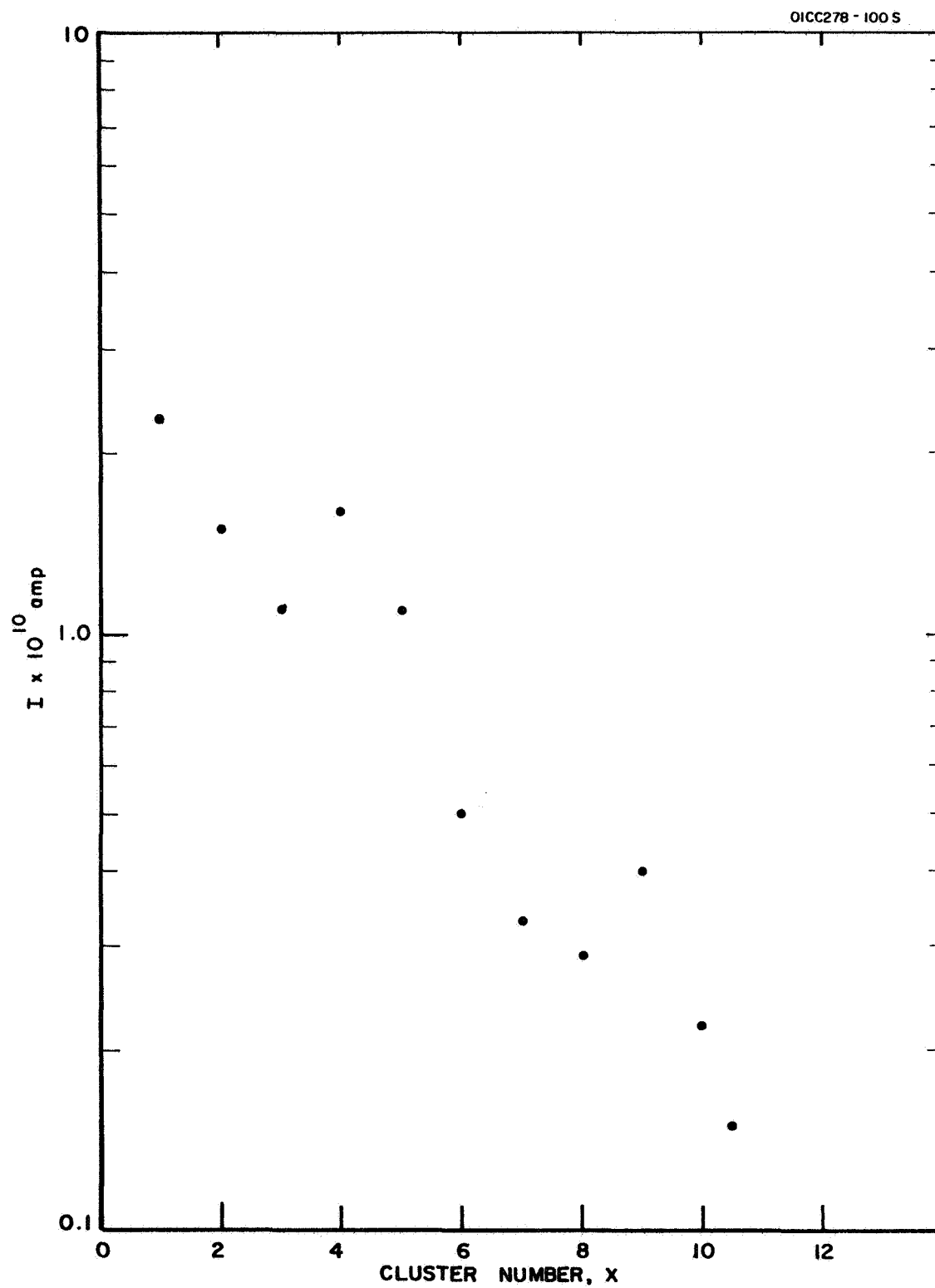


Figure 20. Cluster intensity of $[\text{H}(\text{H}_2\text{O})_x]^+$ vs cluster number.

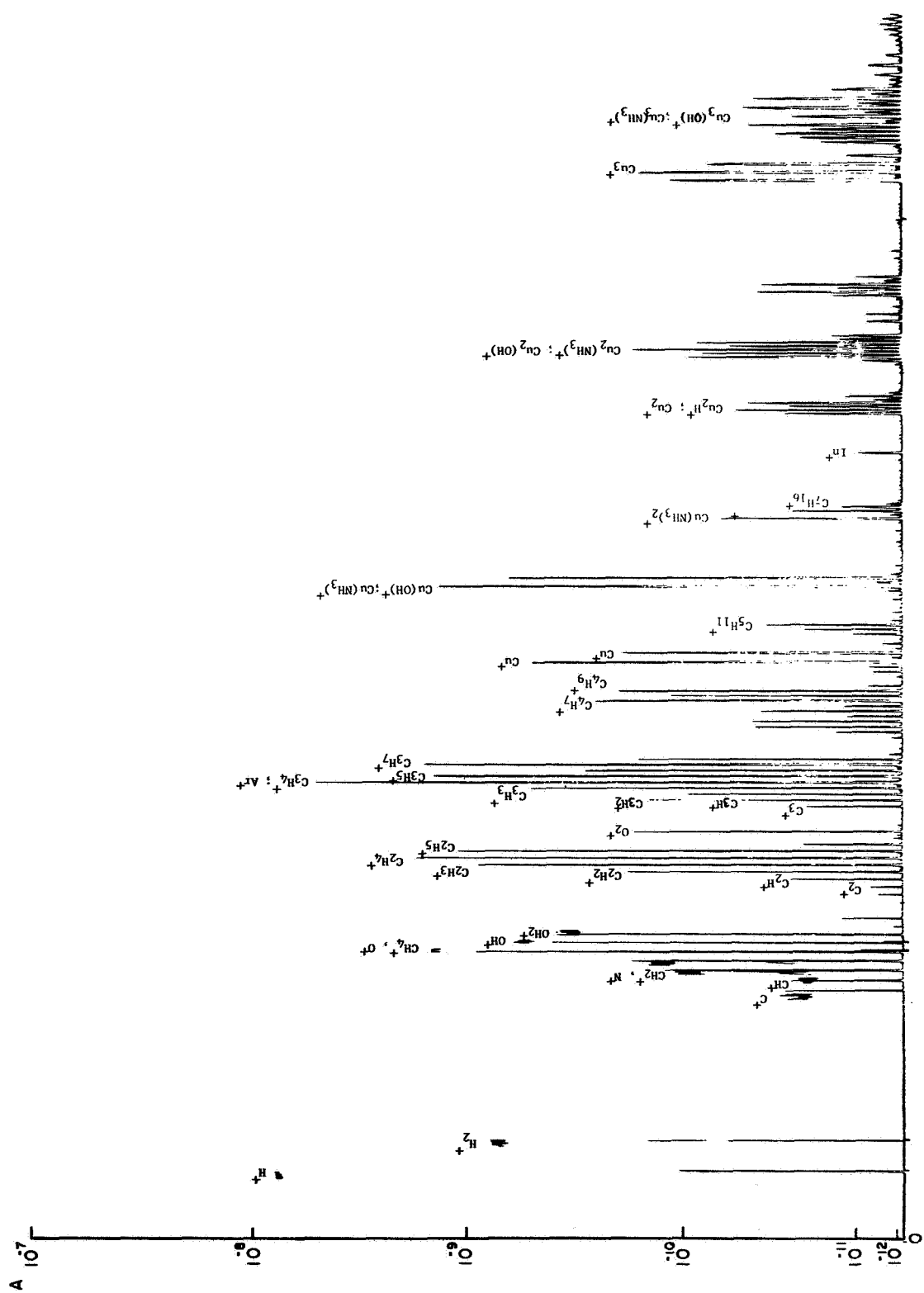


Figure 21. Polyatomic spectrum of heptane at $E_w = 0$ eV; (copper substrate above $25^\circ C$); 8 keV Ar^+ .

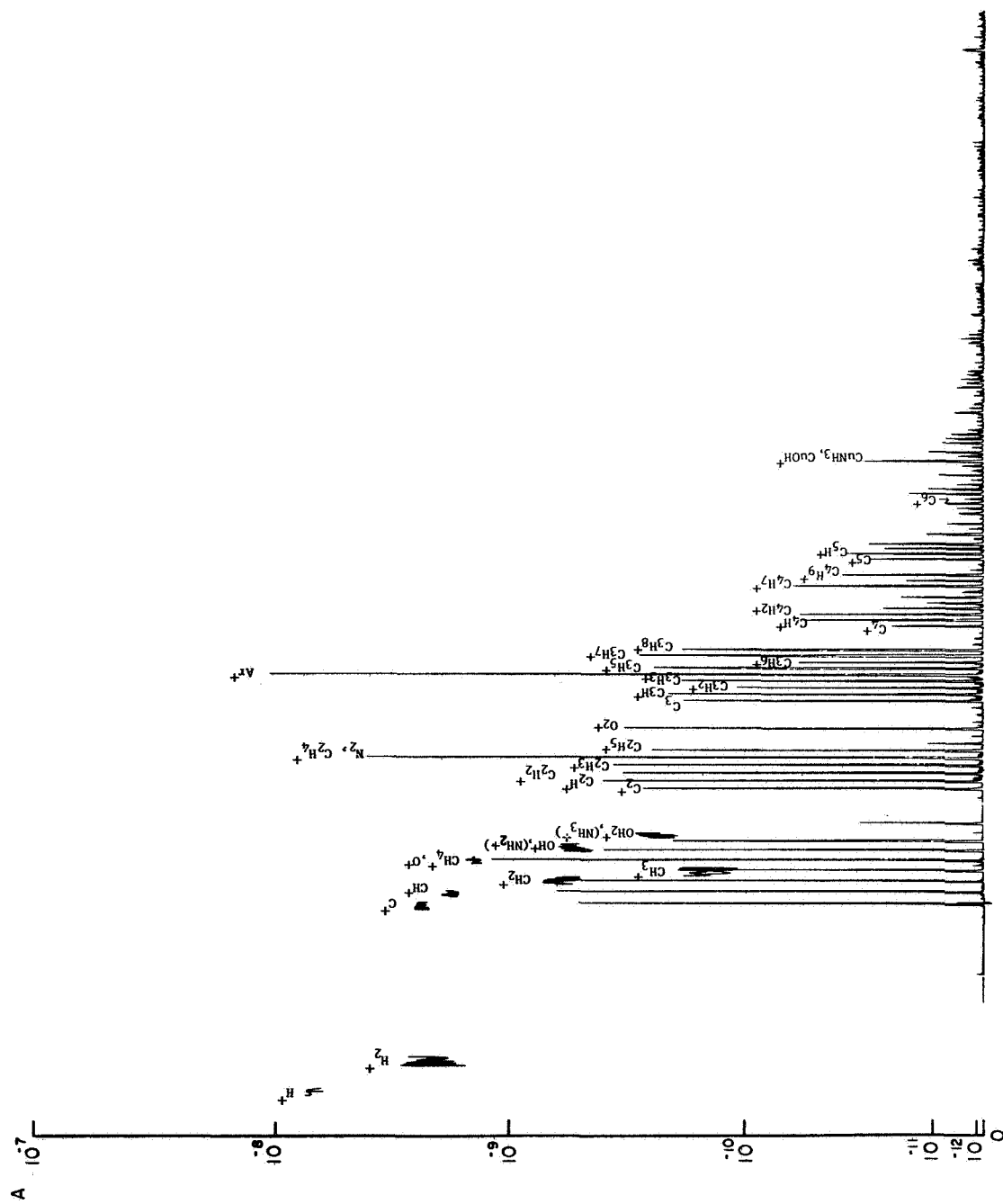


TABLE VII
INTENSITY DISTRIBUTION OF IONS SPUTTERED FROM HEPTANE
ON COPPER; 8 keV Ar⁺

Species, X ⁺	Refrigerant		No Refrigerant	
	I _{X⁺} × 10 ¹⁰	I _{X⁺} / ΣI _{X⁺}	I _{X⁺} × 10 ¹⁰	I _{X⁺} / ΣI _{X⁺}
H ⁺	76	0.40	86	0.49
H ₂ ⁺	22	0.12	7.5	0.046
C ⁺	25	0.13	0.26	0.0016
CH ⁺	18	0.095	0.24	0.0015
CH ₂ ⁺	6.5	0.035	1.0	0.006
CH ₃ ⁺	1.5	0.008	1.3	0.008
CH ₄ ⁺ + (O ⁺) 15*			15	
C ₂ ⁺	2.8	0.015	0.06	0.00037
C ₂ H ⁺	4.1	0.022	0.31	0.0019
C ₂ H ₂ ⁺	3.4	0.018	1.9	0.012
C ₂ H ₃ ⁺	3.7	0.020	9.0	0.055
C ₂ H ₄ ⁺ + (N ₂ ⁺) 43			17	
C ₂ H ₅ ⁺	2.5	0.013	11	0.067
C ₃ ⁺	1.9	0.01	0.25	0.0015
C ₃ H ⁺	2.2	0.012	0.53	0.0032
C ₃ H ₂ ⁺	1.1	0.0059	0.95	0.0058
C ₃ H ₃ ⁺	1.9	0.01	5.1	0.031
C ₃ H ₄ ⁺ + (Ar ⁺) 110			53	

TABLE VII (continued)

Species, X^+	Refrigerant		No Refrigerant	
	$I_{X^+} \times 10^{10}$	$I_{X^+} / \Sigma I_{X^+}$	$I_{X^+} \times 10^{10}$	$I_{X^+} / \Sigma I_{X^+}$
$C_3H_5^+$	2.5	0.013	14	0.086
$C_3H_6^+$	0.59	0.0031	2.9	0.018
$C_3H_7^+$	2.9	0.015	17	0.10
$C_3H_8^+$	1.9	0.01	1.6	0.0098
C_4^+	0.2	0.0011	0.02	0.000012
C_4H^+	0.55	0.0029	0.14	0.00086
$C_4H_2^+$	0.58	0.0031	0.46	0.0028
$C_4H_3^+$	0.22	0.0012	0.47	0.0029
$C_4H_4^+$	0.11	0.00058	0.11	0.00067
$C_4H_5^+$	0.18	0.00095	0.42	0.0026
$C_4H_6^+$	0.04	0.00021	0.11	0.00067
$C_4H_7^+$	0.62	0.0032	2.6	0.016
$C_4H_8^+$	0.17	0.0009	1.2	0.0074
$C_4H_9^+$	0.38	0.0020	2.0	0.012
C_5^+	0.27	0.0014	0.01	0.000061
C_5H^+	0.36	0.0019	0.06	0.0004
$C_5H_2^+$	0.22	0.0012	0.06	0.0004
$C_5H_3^+ + (Cu^+) 0.28$			5.0	
$C_5H_{11}^+$	0.07	0.00037	0.42	0.0026
C_6^+	0.03	0.00016	0.02	0.000012
C_6H^+	0.10	0.00053	0.01	0.000061

* Numbers to the left of the column were not included in the sum of of the intensities because of the interference.

intensities of C_X^+ in graphite, heptane (solid), and silicon carbide are shown in Figure 23 (Ref. 4). Both graphite and heptane show higher intensities for odd values of X, whereas this is not seen for silicon carbide. The similarity between graphite and heptane is not too surprising when one considers the existence in both cases of strings or closed loops of adjacent C atoms (not so for SiC). The fact that polymolecular ions $(C_7H_{16})_X^+$ are not observed in the spectra of solid heptane is consistent with the lack of intermolecular bond strength expected in a condensed hydrocarbon.

5. Conclusions

An exploratory device for condensing gases and vapors (cryogenic holder) for use in the sputter-ion source mass spectrometer at GCA was designed, constructed, and evaluated with selected molecules. The ultimate purpose of this assembly was to concentrate condensable impurities from an atmosphere and to identify them from the characteristic sputtering pattern.

The conclusions are that when complete coverage of the substrate is achieved the sputtering of polar molecules such as H_2O and NH_3 yield characteristic ion clusters proliferating over a large mass range. The sputtering of nonpolar molecules yield characteristic fragment ions without any evidence for the formation of clusters. Both the above effects in themselves suggests that the method of sputtering is not a promising analytical method for the specific identification of a complex mixture of impurities.

However, with incomplete coverage a number of gases yielded specific substrate-gas interaction complexes such as $[In(H_2O)]^+$, $[Au(NH_3)_2]^+$, $[TaCO]^+$ which suggests the possibility of gas identification utilizing the combination of ion generation by sputtering and the recognition of such selected chemical interactions. The intensity of the above species were considerably enhanced with cryogenic operation. For the experimental conditions utilized, the complex ion intensities were higher or of the same order as the sputtered fragment ions of the molecules.

The above phenomenon may be restricted to polar molecules. Certainly, the nonpolar heptane did not result in such complexes. At the present time it is not known whether the molecular dipole moment is a prerequisite for complex formation, or whether suitable substrates for developing such complexes in the case of nonpolar molecules can also be found. More experimentation is required to resolve this problem.

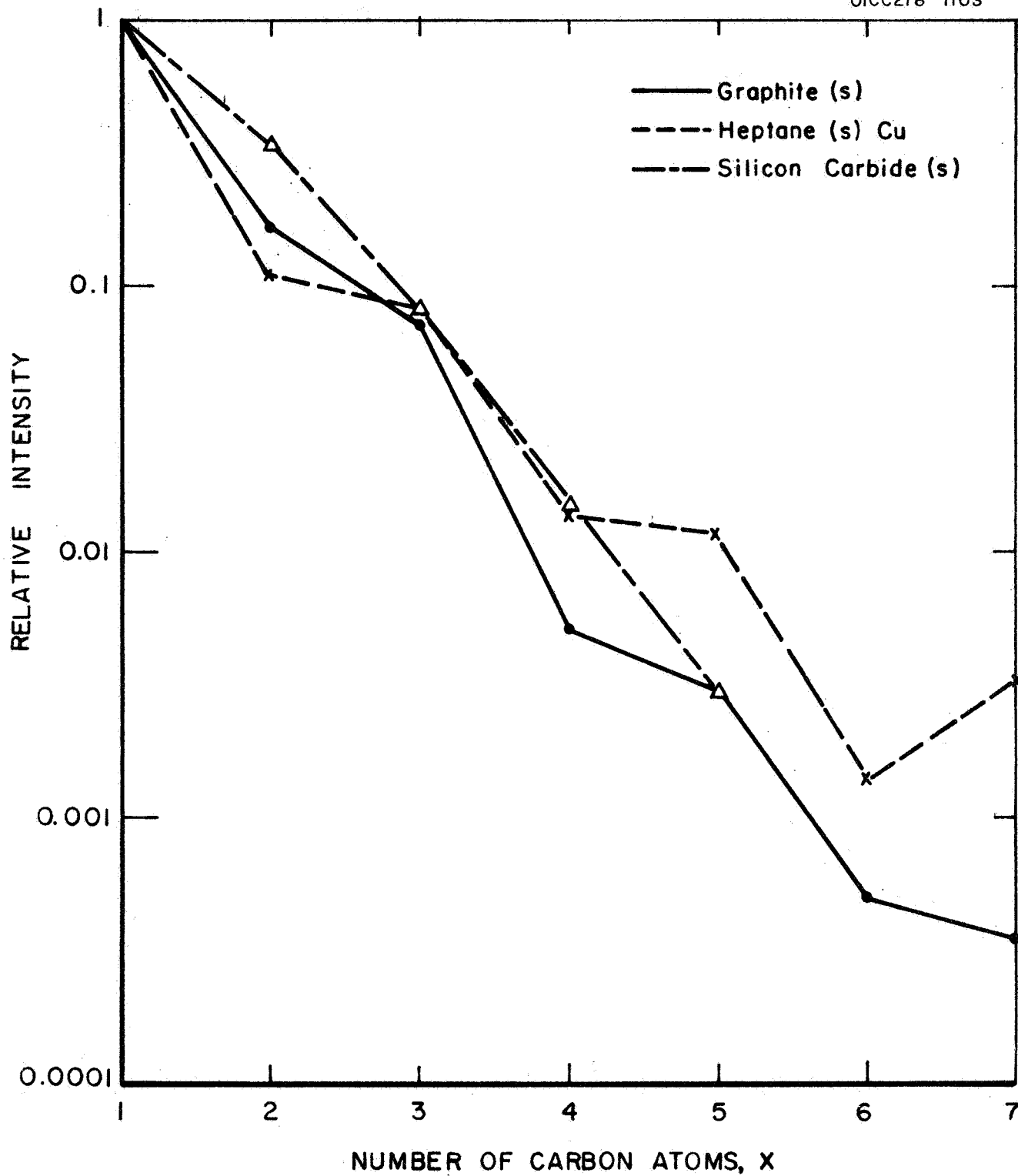
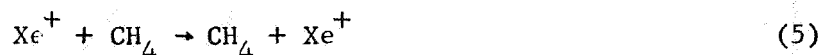


Figure 23. Relative intensities of C_X^+ from the sputtering of various carbon bearing species.

III. CHARGE TRANSFER MASS SPECTROMETRY

1. Introduction

This section deals with a new concept in analytical mass spectrometry; the utilization of charge transfer processes as the source of the ionization of the gas sample. At low kinetic energies, charge transfer and other selected ion-neutral reactions are very efficient processes, many of them occurring upon essentially every collision, provided an exothermic reaction path is available. To illustrate this principle, consider the interactions of argon, krypton and xenon ions with methane:



If the reactants under consideration are in their ground states, then the reactions of argon and krypton ions are exothermic by virtue of the fact that the recombination energies (Ref. 4) of both ions exceed the ionization energy of methane. Indeed, the energy provided by argon ions is high enough to cause the methane ion initially formed to undergo fragmentation, thereby leading to the indicated reaction channels. With krypton ions the energy is insufficient to give methane fragments, and with xenon there is not even enough energy available to ionize the methane molecule unless the energy deficiency is made up by kinetic energy. This example makes apparent that by an appropriate choice of the primary ionic reactant, the formation of fragment ions can be suppressed in favor of the parent ion of the substance to be ionized. In view of the experience that in analytical mass spectrometry using conventional electron impact ion sources, extensive fragmentation is a major difficulty in analyzing complex gas mixtures, it is evident that a source of ionization that minimizes fragmentation would have a considerable practical value. While krypton ions seem to be the appropriate choice of an ionizing agent for methane, other primary ions might prove more suitable in the analysis of other compounds and their mixtures. In Table VIII are listed the ionization potentials of a variety of organic materials to illustrate that many of

TABLE VIII
IONIZATION POTENTIALS OF SOME ORGANIC COMPOUNDS

PARAFFINS		OLEFINS AND ACETYLENES	
Methane	12.98	Ethylene	10.5
Ethane	11.65	Propylene	9.73
i-Butane	10.57	1 Butene	9.58
n-Butane	10.63	1.3 Butadiene	9.07
i-Pentane	10.32	t-1-Butene	9.13
n-Pentane	10.35	C-2-Butene	9.13
2,2 Dimethylbutane	10.06	3-Methyl-1-Butene	9.51
Cyclopentane	10.53	1 Pentene	9.50
2,3 Dimethylbutane	10.02	2-Methyl-1-Butene	9.12
2 Methylpentane	10.12	Cyclopentene	9.01
n-Hexane	10.10	Cyclohexane	8.95
n-Heptane	10.08	4 Methylcyclohexane	8.91
Cyclohexane	9.88	Acetylene	11.41
Methylcyclohexane	9.85	Propyne	10.36
AROMATICS			
m-Xylene	8.56	Benzene	9.25
p-Xylene	8.45	Toluene	8.82
o-Xylene	8.56	Ethylbenzene	8.76

them have ionization energies below 10.5 eV. For these, the 14.0 eV recombination energy of Kr^+ will give rise to substantial fragmentation, whereas a source of ionization not exceeding 10.5 eV (e.g., mercury ions) should lead to relatively simple spectra. In the following section of the report, the particular requirements to be considered in designing a charge transfer ion source are discussed. Subsequently, a source configuration adopted for feasibility studies and the associated test apparatus are described, the results obtained with this new source are presented and recommendations for improvements are given.

2. Charge Transfer Source Design Criteria

The two principal components of a charge transfer ion source are a source of the required primary ions and a chamber in which interaction with the sample gas occurs. The two units must be sufficiently isolated from each other so that the entering of sample gas and its ionization in the primary ion source is precluded. For a discussion of the events taking place in the charge transfer region consider a box with apertures at opposite walls, one for the entrance of the primary ions, one for the withdrawal of both primary and secondary ions. If the spacing of the walls is d , and the velocity of the primary ions is v , the time they need to traverse the chamber is $\tau = d/v$. During this time interval, the primary ion intensity, I_1 , decreases due to charge transfer and the secondary ion intensity, I_2 , increases correspondingly. From the reaction rate law

$$-dI_1 = dI_2 = kI_1 n dt \quad (6)$$

one finds after the time $t = \tau$

$$I_1 = I_0 \exp(-kn\tau) \quad (7)$$

$$I_2 = I_0 [1 - \exp(-kn\tau)]$$

Here, I_0 is the initial primary ion intensity, n is the number density of the neutral reactant, and k is the reaction rate coefficient.

For near thermal ion energies, k is approximately independent of the ion velocity. Its magnitude is of the order of $k \approx 10^{-9} \text{ cm}^3/\text{molecule sec}$. For analytical purposes, it is desirable that the secondary ion intensity is linear with the sample gas number density in the charge transfer region. This condition requires that $kn\tau \leq 0.2$, because then the exponential function can be approximated by $\exp(-kn\tau) \approx 1 - kn\tau$ so that

$$I_2 = I_0 kn\tau \quad (8)$$

In the absence of collisions, the velocity of primary ions in the mass range 30 to 100 amu, having energies 0.1 to 1.0 eV, is approximately $v = 10^5$ cm/sec. The transit time of such ions in a space 1 cm deep is $\tau = 10^{-5}$ sec. The above conditions, therefore, leads to an upper limit of the sample gas density of $n = 2 \times 10^{13}$ molecules/cm³ if the charge transfer rate coefficient is $k = 10^{-9}$ cm³/molecule sec, or $n = 2 \times 10^{14}$ molecules/cm³, if $k = 10^{-10}$ cm³/molecule sec. Such number densities correspond to partial pressures of 1 to 10 millitorr.

The assumption of constant primary ion velocity is justified only if the charge transfer region is free from electric fields. Moderate fields, up to 10 V/cm, are however required to obtain reasonable collection efficiencies for the secondary ions formed in the transfer chamber. At the relatively low pressures mentioned above, the collector field may result in an acceleration of the primary ions to unacceptably high energies, giving rise to the occurrence of endothermic charge transfer processes. This problem can be avoided by the use of an inert carrier gas to raise the total chamber pressure to values such that the primary ions make many collisions and thereby lose most of the energy gained from the field during their acceleration between collision. The minimum required pressure for this mechanism is about 5×10^{-2} torr. The motion of the ions then consists of a drift in the direction of the electric field with a velocity $v = AE/p$, which is proportional to the electric field strength E and inversely proportional to the carrier gas pressure p . Superimposed upon the ionic motion of drift is diffusion in the lateral and longitudinal directions. The observable secondary ion intensity in this case is given by

$$I_2 = CI_0 k n \tau = CI_0 k n d p / AE \quad (9)$$

where C is the applicable ion collection efficiency. It is appropriate to restate the provisions for which this expression is valid: $p \geq 5 \times 10^{-2}$ torr; and $k n d p / AE \leq 0.2$. Since with these conditions the charge transfer reactions do not seriously deplete the initial primary ion intensity, the derived expression is also valid for each component of a sample gas mixture, where one should note that the value for the rate coefficient k will differ for each secondary ion producing process.

In deriving Equation (9), it was tacitly assumed that the number density of the sample gas is uniformly distributed throughout the charge transfer chamber. If the sample is mixed with the carrier gas prior to entering the chamber, a uniform density distribution is achieved automatically. If, however, both gases enter separately, the time required for the mixing of both components must be shorter than the average residence time of the sample gas in the charge transfer region. In the absence of turbulence the mixing time is given by the speed of diffusion of the sample into the carrier gas. For a total gas pressure of 0.2 torr, mixing by diffusion is estimated to take 2.5×10^{-3} sec if the chamber diameter is 2.5 cm.

This time constant decreases with decreasing pressure. The average residence time of the sample gas is given by the ratio of the volume of the chamber and the sample gas volume flow rate, which in turn is governed by the orifices in the chamber through which the gases effuse into the surrounding vacuum. An appropriate choice of chamber volume and orifice diameter, therefore, will ensure an adequate residence time of the sample gas in the chamber. For example, if the gas escapes through the main orifice by free molecular flow, the volume flow rate is $\pi a^2 \bar{c}/16$, where a is the diameter of the orifice and $\bar{c} \approx 4 \times 10^4$ cm/sec is the average molecular thermal velocity. To achieve a sample gas residence time ten times greater than the diffusion time constant, $\Delta t = 2.5 \times 10^{-3}$ requires that

$$\frac{16V}{\pi a^2 \bar{c}} \geq 2.5 \times 10^{-2}, \quad \text{or} \quad a^2 \leq 5.1 \times 10^{-3} V \quad (10)$$

With a chamber volume of $V = 5 \text{ cm}^3$, the maximum allowable orifice diameter is calculated to be $a = 1.6 \times 10^{-1} \text{ cm}$.

3. The Feasibility Model Charge Transfer Ion Source

Since the secondary ion intensity is directly proportional to the primary ion intensity, it is clear that the sensitivity of the device is dependent mainly on the available primary source intensity. The desired high ion fluxes can be produced both with electron impact and with gas discharge sources. In the present feasibility study, it was decided to make use of a gas discharge source, because this type of ion source operates at higher pressures than common electron impact sources, so that the possibility of its contamination by back diffusing sample gas is reduced. The operating pressure in the discharge is even higher than the pressures required in the charge transfer region, thus allowing a direct flow of carrier gas from the discharge through the charge transfer region. Facility of construction and handling are additional aspects favoring the use of a discharge ion source in the experimental evaluation of the charge transfer mass spectrometer concept.

The layout of the feasibility model ion source is shown in Figure 24. The two types of discharge tubes shown in Figure 25 were employed. One was a 1.28-cm diameter quartz-pyrex tube epoxied end-on to an aluminum disc, the other used a Kovar-pyrex joint welded to a stainless steel disc, the Kovar cylinder being shielded by a ring-sealed, 8-mm diameter pyrex tube. Both discharge tubes were fitted at the opposite end with a positive electrode and the gas inlet. The gas was introduced through a stainless steel leak valve and first passed a liquid nitrogen cooled trap before it entered the discharge. The inlet tubulation was pyrex with Kovar terminals joined by stainless steel Swagelok fittings. The

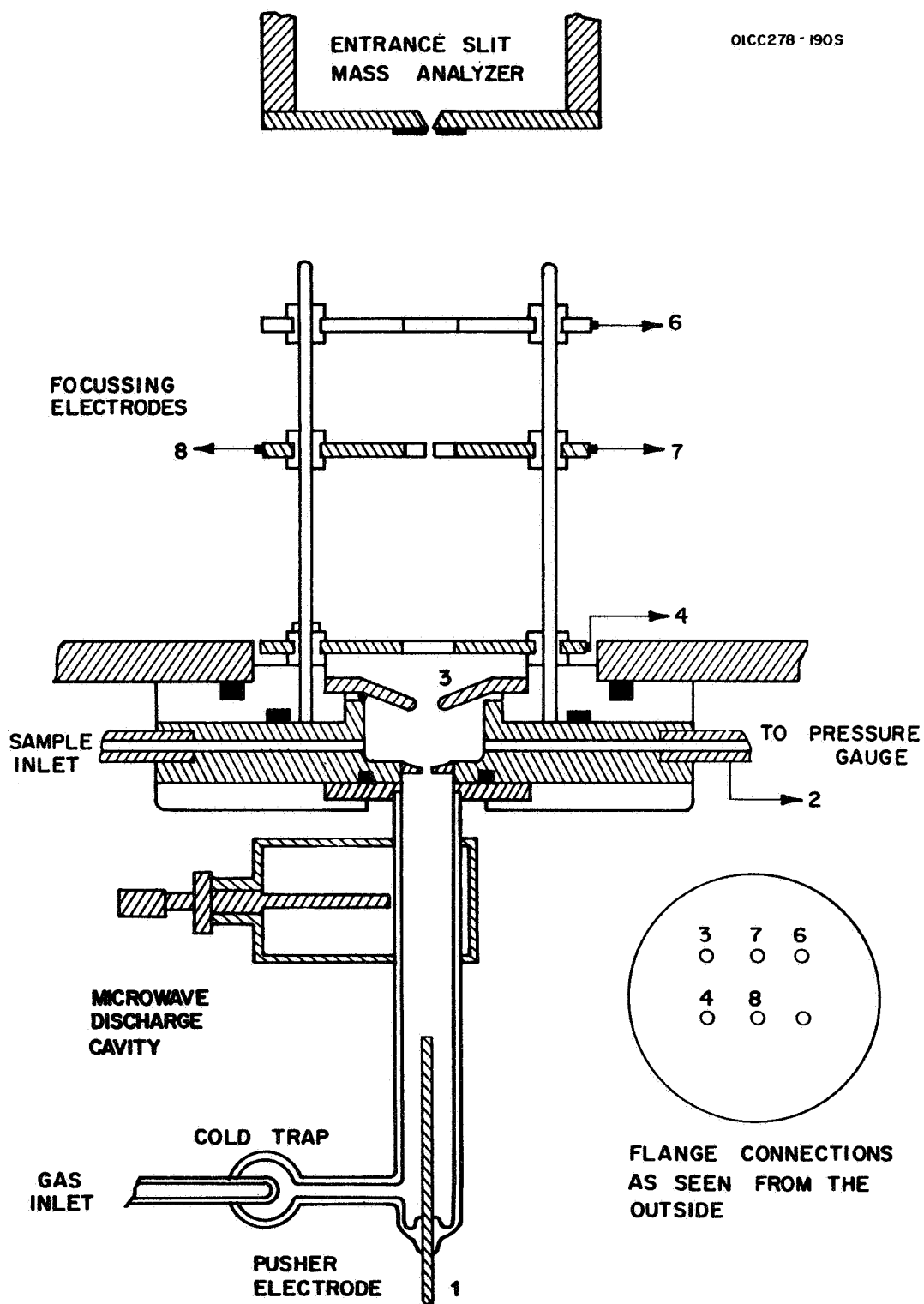


Figure 24. Charge transfer ion source.

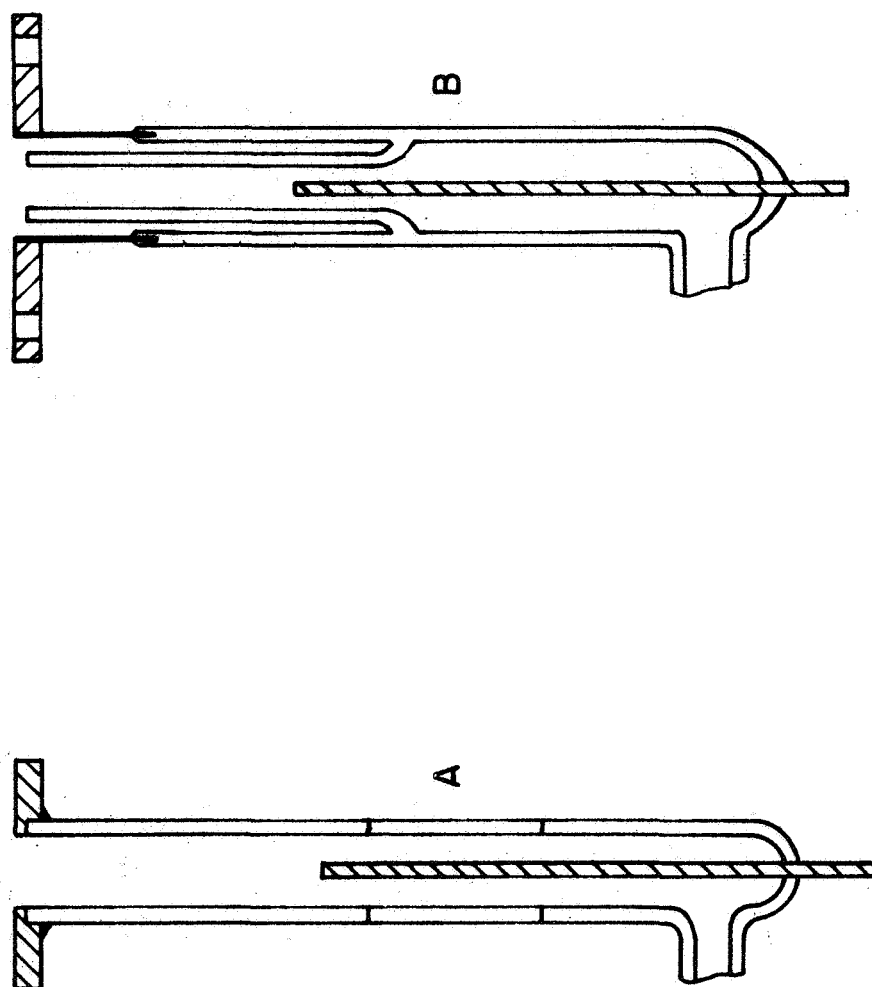


Figure 25. Discharge tubes. A - quartz-pyrex graded seal epoxied to aluminum disc
 B - Kovar-pyrex seal welded to stainless steel plate.

discharge was powered either by a 2450-Mc ac field applied with an Evenson (Ref. 5) cavity as shown in Figure 24, or by a sufficiently high dc field to produce a cold cathode discharge. Cooling was provided by a compressed air stream.

The charge transfer chamber is housed in a stainless steel flange to which the discharge tube is joined with a conventional O-ring seal. Ions from the discharge enter the charge transfer space through an orifice contained in a threaded insert, to facilitate its replacement when required. Throughout most of the experiments, the orifice was a cylindrical channel of equal length and width, about 0.06 cm. Incorporated in the chamber flange are two outer connections, one leading to a leak valve to introduce the sample gas, the other leading to a McLeod gauge via a cold trap so that the chamber pressure can be monitored. Because of the high potential applied to the chamber, the lead connections were nylon tubing fastened with Swagelok fittings.

Ions are extracted from the charge transfer space by a weakly converging electric field provided by an indented extraction plate. Its central orifice was 0.14-cm diameter. After passage of this orifice, the ions are accelerated and focused onto the entrance of a 180-degree magnetic analyzer by an assembly of 1.28-cm diameter aperture stainless steel plates acting as an immersion lens system. The last two plates are fitted with horizontal and vertical deflectors to achieve directional focusing. Their potentials are negative with respect to ground, to avoid the reverse acceleration and focusing of electrons formed by the ion beam at the mass spectrometer entrance slit. The three plates are mounted on four threaded rods with the aid of nylon bushings as insulators. The entire assembly is supported by a nylon spacer flange which also insulates the chamber flange from ground. For the purpose of testing the charge transfer source, the device was mounted to the access port of a 5-inch diameter chamber with six bolts insulated with nylon bushings. The chamber was evacuated with a 4-inch oil diffusion pump. Electrical connections were made, as far as necessary, through an auxiliary side flange. A Veeco ionization gauge monitored the pressure. A 180-degree magnetic mass analyzer was connected to a flange opposite the ion source. This instrument had 1-mm diameter entrance and exit apertures. It was evacuated with a 2-inch diffusion pump. Ions were collected in a simple Faraday cage preceded by a low energy suppressor grid which could be grounded when not in use. Ion currents were measured with a Keithley electrometer and mass spectra were displayed with an X-Y recorder.

With this ion source design, the discharge gas also serves as the carrier gas in the charge transfer space. Pressures typical for its operation were: approximately 1 torr in the discharge, 0.1 torr in the transfer chamber, 10^{-4} torr in the accelerator region, and 10^{-6} torr in the mass analyzer.

The ion acceleration potentials were derived from a 1250V dc power supply in conjunction with a string of resistors forming a voltage divider. In addition to adjustable potentials for proper focusing, the voltage across the charge transfer chamber was adjustable to a maximum of 100 V. The corresponding electric field in that region was 0 to 100 V/cm. The discharge voltage was provided by a separate circuit yielding 0 to 550 V with a 10-mA current capacity.

4. Experimental Results

a. Exploratory investigations. - Preliminary tests of the charge transfer ion source were performed to explore suitable pressure ranges, orifice sizes and electric fields. In these experiments, argon was used as the carrier gas. According to expectation, Ar^+ ions were the main contributor to the observed mass spectra, but in addition a large number of other ionic species were also present. They could be traced to impurities caused by minor air leaks and outgassing. Specifically, the epoxy seal of the discharge tube A in Figure 25 initially used was a source of leaks. It was first substituted by a black wax joint which produced an airtight seal but gave rise to a large impurity peak at mass number 30 presumably caused by off-gassing of ethane. The black wax was subsequently replaced by "torr seal," a high vacuum epoxy distributed by Varian Associates, whereupon the mass 30 peak was essentially eliminated. Other still remaining impurities indicated in the mass spectra could be reduced to a reasonable level by a cleaning of the entire ion source with an organic solvent and by tightening all suspected air leaks. In addition, the O-rings employed in the assembly of the ion source were left unlubricated.

With these measures, mass spectra similar to those shown in Figure 26 were observed. These traces, obtained with the discharge operated in the dc mode, are characterized by contributions at mass numbers 18, 19, 28, 32, and 41 in addition to the expected argon ion peak at 40 amu, pointing to a remaining contamination by air and by water vapor. A portion of the impurities, particularly water vapor, was introduced with the carrier gas, because passing the argon through a liquid nitrogen cooled trap before it entered the discharge reduced the size of the peaks at mass numbers 18, 19, and 41. The detrimental effect of carrier gas contamination clearly called for a suitable purification of the introduced argon. Several measures were applied in an effort to achieve a satisfactory elimination of impurities, but none brought the desired improvement. These measures included the substitution of Airco argon by Matheson purified argon, and the use of various traps on the high pressure side of the argon inlet line to reduce the moisture content. Drierite (CaCl_2), corrugated copper cooled by liquid nitrogen, and baked zeolite were used in the traps. However, the mass number 18 and 41 peaks were not reduced below the level already achieved with the simple liquid nitrogen trap located between the argon inlet valve and the discharge tube. It thus appears that the residual water vapor and air impurities are not introduced with the argon itself, but are released from the walls of the

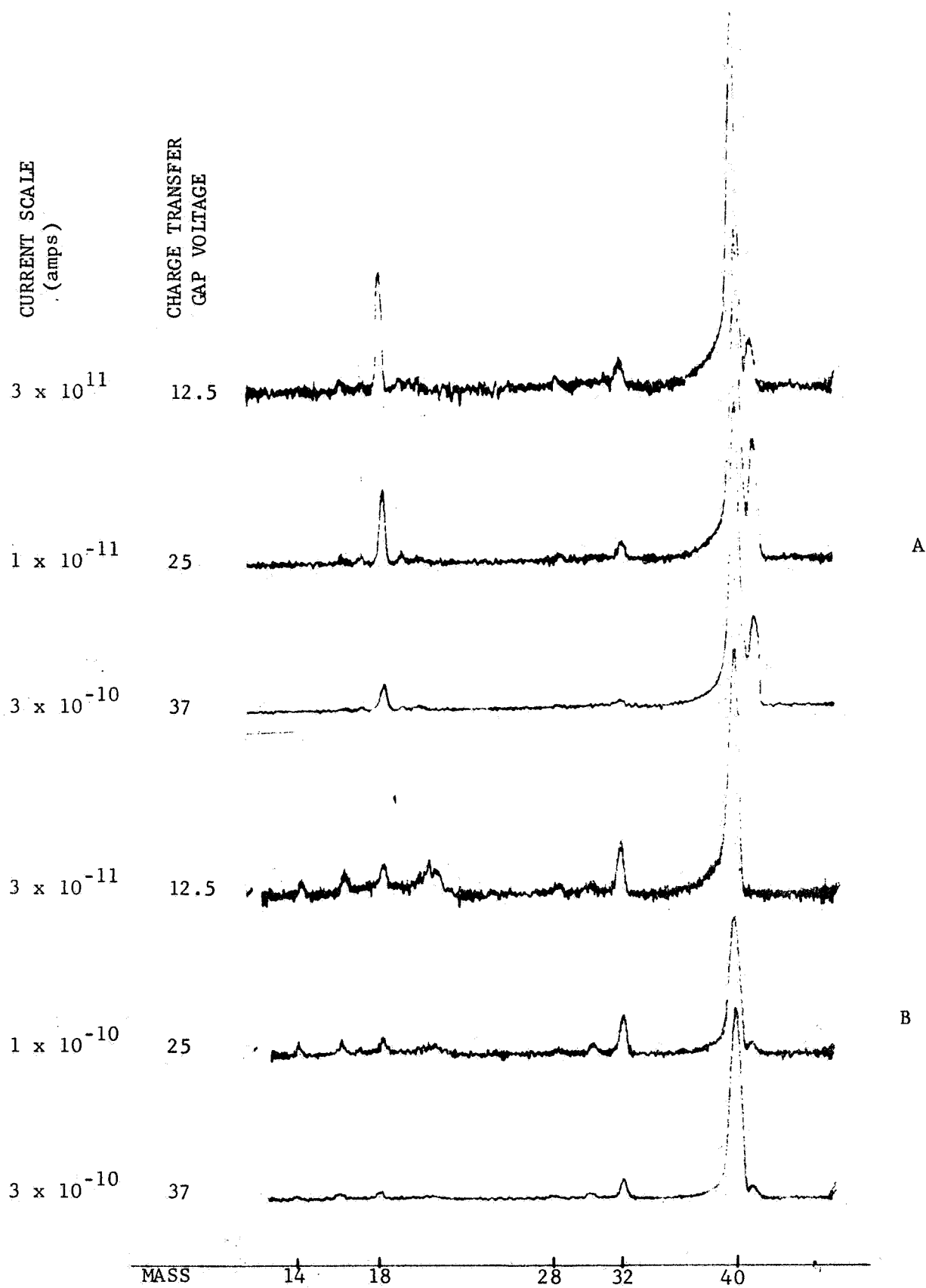


Figure 26. Mass spectra obtained with argon carrier gas and dc discharge, for three different charge transfer gap voltages. A: gas entered directly, B: gas passed through liquid nitrogen trap before entering discharge.

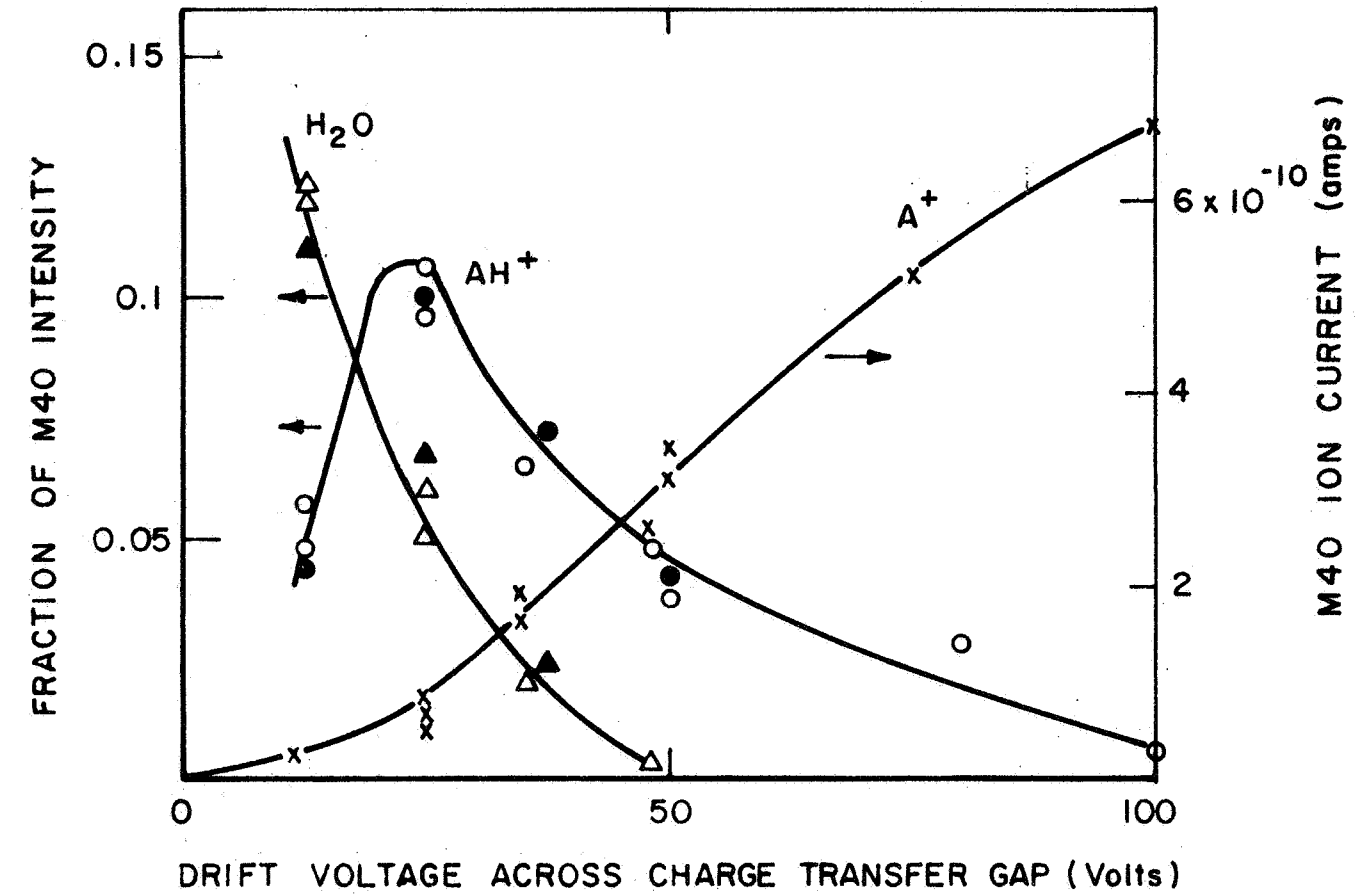
inlet line and the discharge tube by outgassing. This possibility could not be further explored in the present series of experiments, because the ion source, discharge tube and inlet system are not bakeable so that an acceleration of the outgassing process by heating was precluded.

The most likely processes responsible for the formation of the water impurity ions are

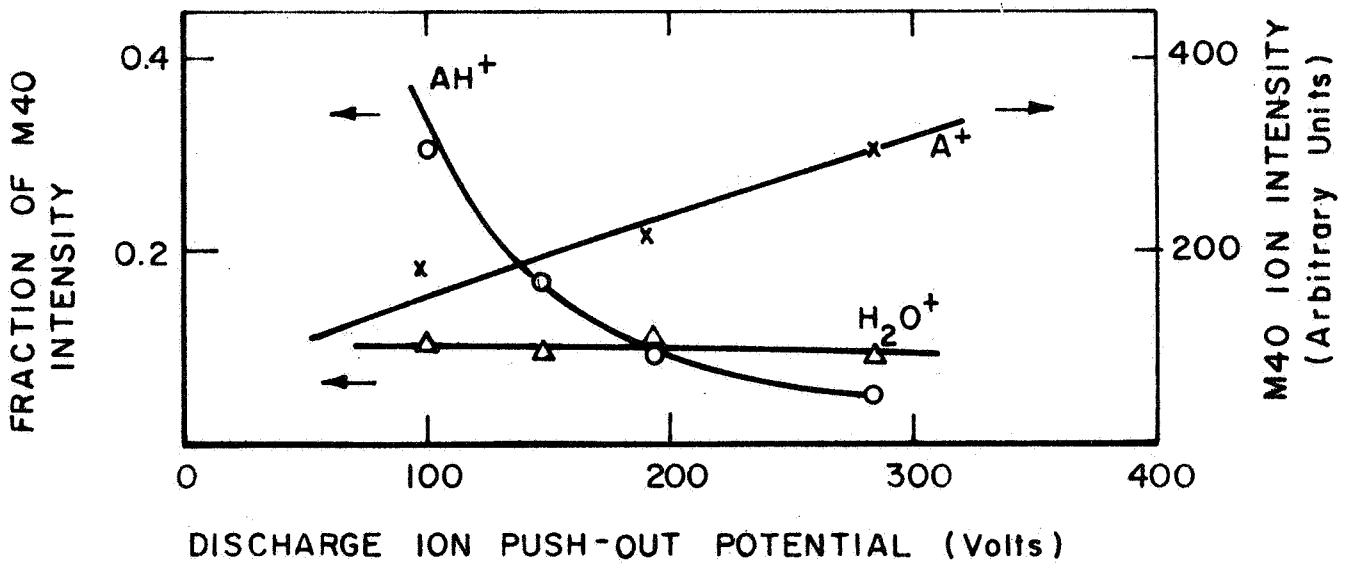


These reactions can occur both in the discharge region and in the charge transfer space. To investigate the location of impurity ion formation a series of experiments was performed in which the ratio of ion currents M18/M40 and M41/M40 was observed as a function of the electric fields applied to the discharge and the charge transfer regions. The results are shown in Figures 27a and 27b.

Decreasing the drift voltage across the charge transfer gap increases the residence time of the primary ions, so that the probability of ionic reactions in this region is enhanced. As Figure 27a demonstrates, the relative intensities of both the H_2O^+ and the AH^+ ions increase with decreasing charge transfer gap drift voltage, thereby indicating the formation of both ions by one of the above reactions in this region. Also shown in Figure 27a is the absolute intensity observed for A^+ which is known to have its origin in the discharge region. The argon ion intensity decreases with decreasing drift voltage due to the decreasing collection efficiency of ions from the charge transfer region. The opposite behavior for H_2O^+ shows that this ion originates mainly in the transfer gap and not in the discharge. The observation that the AH^+ ion intensity goes through a maximum and then decreases again with decreasing gap voltage, whereas the H_2O^+ ion intensity increases further indicates a complex relationship between both ions. No simple explanation for this behavior can be given. One possibility, evidence for which is discussed below, is the formation of AH^+ in both the discharge region and the charge transfer space. A marked influence of the electric field in the charge transfer region on the sampling of ions from the discharge could then result in the observed behavior. Another possibility is that the reaction responsible for AH^+ formation is endothermic, so that its occurrence requires additional kinetic energy which the argon ions must gain from the electric field. Evidently, these complications do not apply to the formation of H_2O^+ which is thus recognized as a simple charge transfer.



(a)



(b)

Figure 27. Ion intensities for A^+ , AH^+ , and H_2O^+ as function of (a) charge transfer gap voltage and (b) discharge ion push-out voltage observed with argon carrier gas.

To determine the influence of the electric field in the discharge region upon the formation of AH^+ and H_2O^+ , the discharge was operated with microwave excitation. This mode of operation avoids the complication by the cathode fall region (see below) that exists in the dc discharge, and it thereby allows more uniform field conditions. Similar to the situation in the charge transfer gap, a lowering of the electric field strength increases the residence time of the ions in the discharge region thus providing an increased reaction probability leading to formation of secondary ions. As Figure 27b demonstrates, the M18/M40 ratio of intensities remained essentially constant when the discharge push-out potential is decreased from 280 to 100 volts, but the AH^+ ion intensity increased significantly. These results make apparent that in addition to the formation of AH^+ in the charge transfer space there occurs a generation of this ion in the discharge region under favorable conditions.

The presence of water and air impurities in the primary ion source has the undesirable side effect that in addition to ion formation by low energy charge transfer and other interactions of the principal primary ion, A^+ , there occurs also the formation of fragment ions of the impurities by other ionization processes. In Figure 26, such fragment ions appear at mass numbers 16, and 14 corresponding to the ions O^+ and N^+ whose formation requires energies greater than 18.8 and 24.0 eV, respectively. Since the recombination energy of the primary argon ions is only 15.5 eV, they cannot be responsible for the production of either O^+ or N^+ unless the necessary additional energy is acquired by acceleration in an electric field. Figure 26 shows qualitatively, that varying the field in the charge transfer region has a negligible effect upon the ion intensities of mass numbers 14 and 16 so that these ions must have their origin in the discharge region.

Both electron and ion impact may contribute to O^+ and N^+ formation. In this respect, it is of interest that in the dc mode of operation ions are withdrawn from the cathode fall region in which the ions are accelerated toward the cathode in a relatively high electric field so that a sufficient electron yield results upon their impact. The electrons in turn are accelerated in the opposite direction and produce ions by impact with neutral gas molecules. Thus there exists a relatively high probability for fragmentary ion production. The microwave discharge, on the other hand, does not require a source of electrons at a boundary surface, since electrons are produced by volume ionization due to electron collisions. Consequently, the cathode fall field is eliminated and the ions do not acquire energy appreciably in excess of thermal kinetic energy.

A comparison of both modes of discharge operation, shown in Figure 28, nevertheless demonstrates that the high frequency discharge generates fragmentary impurity ions with an abundance at least as high as the dc discharge. Accordingly, it appears that excess kinetic energy of primary ions is not the major mode of fragment ion formation and the major process probably is electron impact ionization. However, different field

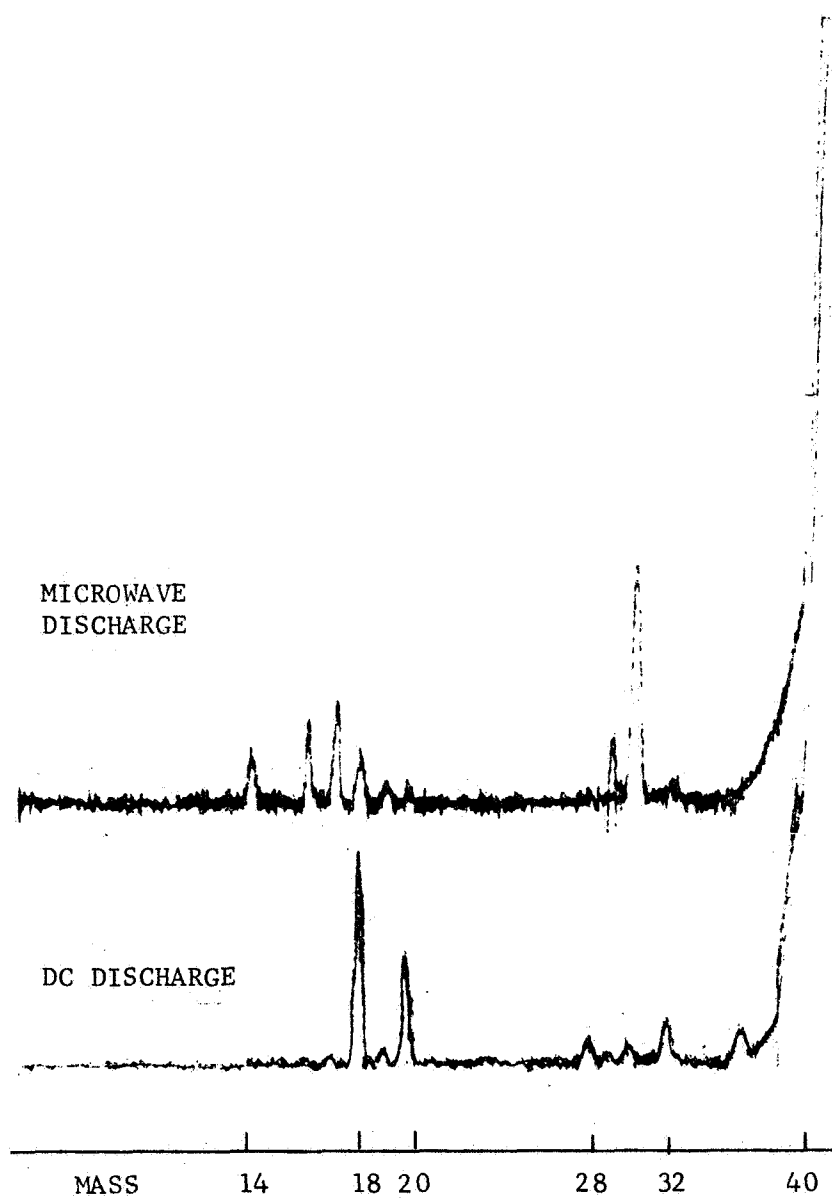


Figure 28. Comparison of microwave and dc discharge mass spectra under otherwise similar conditions.

configurations in the vicinity of the ion sampling orifice may also contribute to the observed effect. More consideration will be given to this problem in a subsequent section.

Since both the fragment and the nonfragment ions resulting from air and water impurities inherent to argon are detrimental to the concept of the charge transfer ion source, the use of other carrier gases was explored. Helium, having a higher potential than argon was found to enhance the contamination of the mass spectrum, whereas with krypton the situation was improved. All subsequent experiments were then performed using krypton as the carrier gas.

In Figure 29 a series of spectra is shown using a microwave excited krypton discharge yielding Kr^+ as the primary ion. The various krypton isotopes at mass $M = 80, 82, 83, 84, 86$ are not resolved, but the intensity maximum coincides with that of the most abundant isotope at mass number 84. Again, water impurity is in evidence in the primary ion spectrum, despite the fact that krypton passes a liquid nitrogen-cooled trap before it enters the discharge. The addition of CO_2 to the drift-space results in the appearance of a peak at mass number 44, corresponding to CO_2^+ . When air is added, the following new ions are apparent: $M = 18, 28, 29$, and 32. A small CO_2 peak from the previous run still remains.

The signals at mass number 18, 32, and 44 correspond to the ions H_2O^+ , O_2^+ , and CO_2^+ , respectively. Their formation by way of charge transfer is expected. The M29 peak is due to N_2H^+ which can be formed via proton transfer from the primary KrH^+ impurity ion. The M28 peak undoubtedly is due to N_2^+ , but since the recombination energies of the krypton $^2\text{P}_{1/2}$ and $^2\text{P}_{3/2}$ ions are only 14.0 and 14.66 eV (Ref. 4), whereas the ionization potential of nitrogen is 15.5 eV, the nitrogen ion cannot be formed by simple thermal charge transfer.

The uppermost trace in Figure 29 shows that when the ion push-out potential in the discharge is decreased, the M28 decreases also whereas the M29 peak increases. The first observation indicates that N_2^+ is formed by interaction of nitrogen with the discharge, but a discussion of this point will be deferred. The second observation is probably due to an increase in the primary KrH^+ concentration resulting from a longer residence time of krypton ions in the discharge region at lower push-out fields. This is similar to the mechanism of AH^+ formation in the argon discharge discussed previously.

b. Primary source strength. — In the discharge the total ion current density is given by $j = env$ where $e = 1.6 \times 10^{-19}$ coulomb is the ionic charge, $n \approx 10^{10}$ ions/cm³ is the ion density in the discharge, and v is the drift velocity. For fields around $E/P = 100$ V/cm-torr, drift velocities are $v \approx 10^5$ cm-sec so that the expected current density is $j = 10^{-4}$ amps/cm². With an exit orifice diameter of 0.06 cm, the corresponding

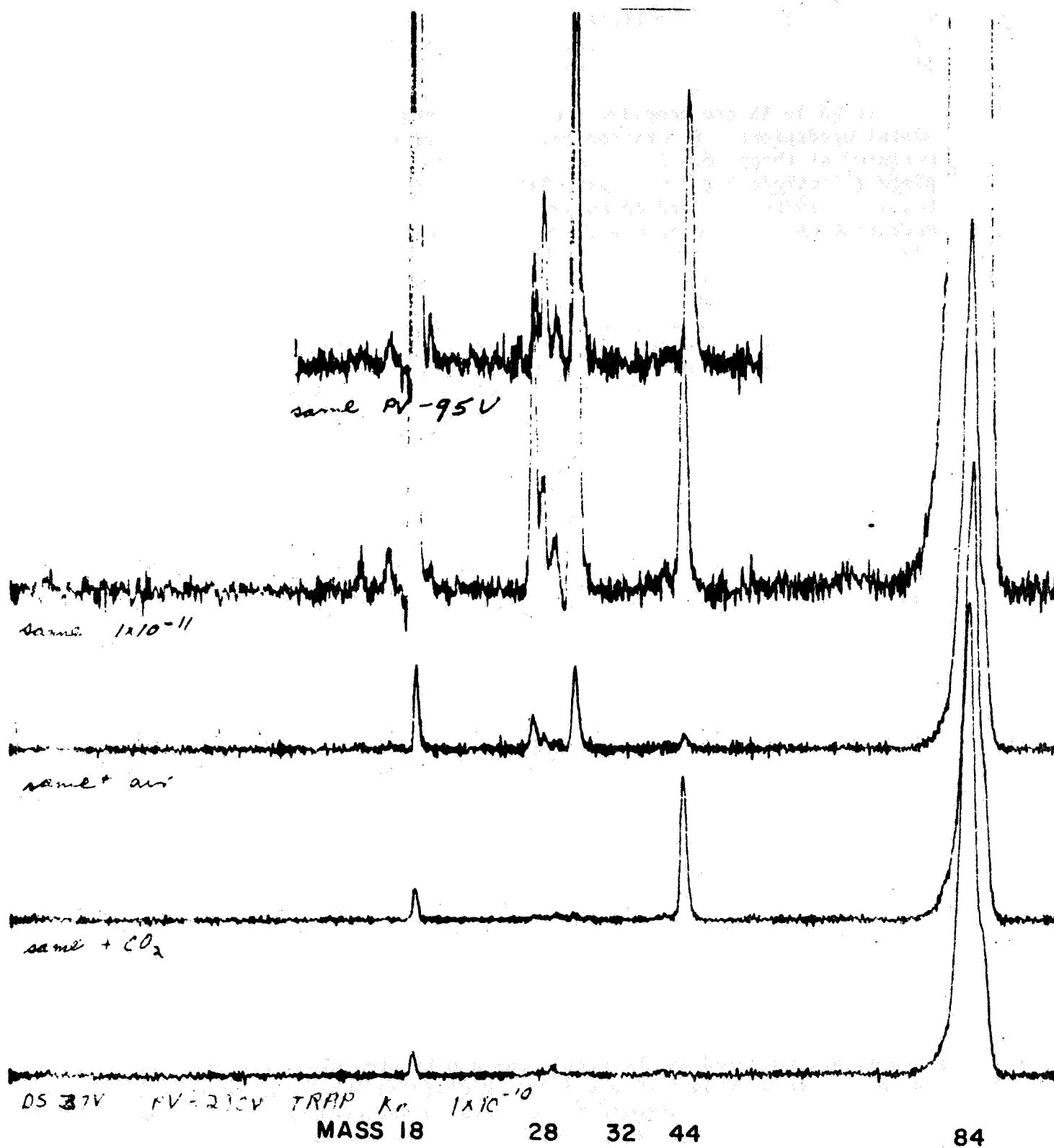


Figure 29. Mass spectra obtained with krypton microwave discharge. From bottom: without sample in, with CO_2 added, with air added.

area is $3 \times 10^{-3} \text{ cm}^2$, or about one-thousandth of the total metallic area accessible to the discharge current. Accordingly, a primary ion current of the order of 10^{-7} amps was expected to enter the transfer region.

In Table IX are compiled ion currents measured for various experimental conditions with krypton being the carrier gas. Ion currents were measured at three locations: at the charge transfer chamber extraction plate (electrode No. 3 in Figure 24), at the first focusing plate (electrode No. 4 in Figure 24), and on an auxiliary electrode placed behind the mass spectrometer entrance aperture. Currents measured on the first focusing plate were negligible compared with those on the other two electrodes and are omitted from Table IX. It is evident that most of the ions entering the charge transfer regions are discharged on the ion extraction plate and that only a fraction of them are withdrawn and focused into the mass spectrometer, regardless of the field conditions either in the discharge or in the charge transfer chamber. A considerable spread of the primary ion beam is thereby indicated. With microwave excitation, the current intensity of the primary ions is of the order of 10^{-7} amps as was anticipated. That for dc discharge operation is a factor of ten lower. The considerable spread of the primary ion beam must be largely due to charge repulsion. The ion density at the discharge orifice can be estimated as $n_1 \approx 10^{10} \text{ ions/cm}^3$. The corresponding electric fields are as high as 300 V/cm. Spreading of the ion beam by lateral diffusion is comparatively slow, and cannot explain the observed effect. Increasing the ion extraction field and decreasing the pressure improves the ion collection efficiency, but both measures also reduce the primary ion residence time in the charge transfer chamber so that the probability of charge transfer decreases. The dc glow discharge which generates a lower primary ion current than the microwave discharge provides a collection efficiency ten times better by comparison. This observation supports the assumed mechanism of ion beam spreading by charge repulsion, since the lower ion concentrations generated from the dc discharge would cause less broadening of the ion profile than the high ion densities resulting from the microwave plasma.

c. Secondary ion intensities and behavior. — In Section III,2 a formalism was developed for the functional behavior of the intensity of secondary ions resulting from primary ion interaction with the sample gas in the charge transfer space. According to Equation (9), the secondary ion intensity would be proportional to the sample gas pressure and to the total (carrier gas) pressure in the charge transfer region, and it would be inversely proportional to the electric field. To compare the predicted with the actually observed behavior of secondary ion intensities, a series of experiments was performed in which the variation of ion intensities with the indicated parameters was investigated. For this purpose, air was used as the sample gas and krypton was the carrier gas. The major secondary ions observed were H_2O^+ (M18), N_2H^+ (M29) and O_2^+ (M32). The molecular nitrogen ion at mass number 28 appeared also, but it will be shown subsequently that this ion does not originate in the

TABLE IX

PRIMARY ION INTENSITIES FOR VARIOUS EXPERIMENTAL CONDITIONS

Discharge Condition	Microwave Excitation				DC Discharge a
	a	a	a	b	
Discharge dc potential (volts)	0	470	470	470	550
Charge transfer, drift potential (volts)	25	25	100	100	25
Ion current extraction plate (amps)	1.5×10^{-7}	7×10^{-7}	1×10^{-6}	1.4×10^{-6}	2.5×10^{-8}
Ion current entering mass spectr. (amps)	5×10^{-11}	3×10^{-10}	5×10^{-10}	7×10^{-10}	8×10^{-11}

(a) Pressure in the charge transfer chamber about 0.18 torr.

(b) Pressure in the charge transfer chamber about 0.09 torr.

charge transfer region. Hence, it will be considered separately. The reactions thought responsible for the formation of the three major ions are



Two of these are plain charge transfer processes, while the interaction with nitrogen results in a proton transfer.

Figure 30 shows the influence of the air sample pressure upon the intensity of the secondary ions. As predicted, a linear relationship is observed. It is of interest to note that the H_2O^+ and the O_2^+ intensities are almost equal, even though the concentration of H_2O must be much less than that of oxygen. Evidently the rate of charge transfer to H_2O is much greater than that to oxygen. Although the rates for Reactions (9) and (11) are not available, it can be estimated from a simple theory (Ref.6) and from comparison with argon ion reactions (Ref. 7,8) that water reacts about 20 times faster than oxygen. If the reaction rates are assumed to be $k(\text{H}_2\text{O}) = 2 \times 10^{-9}$ and $k(\text{O}_2) = 1 \times 10^{-10}$, one calculates a water vapor content of one percent which corresponds to about 50-percent humidity. This is a reasonable value.

Figure 31a gives the variation of secondary ion intensities with the drift voltage applied to the charge transfer gap. At values less than 50 volts, the ion intensities first increase as expected, then reach a maximum followed by a sharp decrease. The decrease at low drift voltages is interpreted as a decreasing collection efficiency of ions withdrawn from the charge transfer region. In Figure 31b the same data are plotted versus the inverse of the applied voltage to show that the ion intensities exhibit a linear behavior at inverse voltage values up to one-tenth, corresponding to drift voltages greater than 10 volts, in agreement with the prediction made according to Equation (9). To obtain this result, the ion collection efficiency must have remained reasonably constant in the voltage domain greater than 10 volts.

Figure 32 shows the dependence of the ion intensities on the carrier gas pressure. Since in this experiment the carrier gas pressure was varied by adjusting the krypton gas flow, the data are complicated by the possibility of a simultaneous variation of the primary ion intensity. Indeed, the observed primary ion intensity varies by a factor of about two, but this variation must be partially due to a decreasing collection efficiency with increasing pressure, because the ion beam spreads as the residences

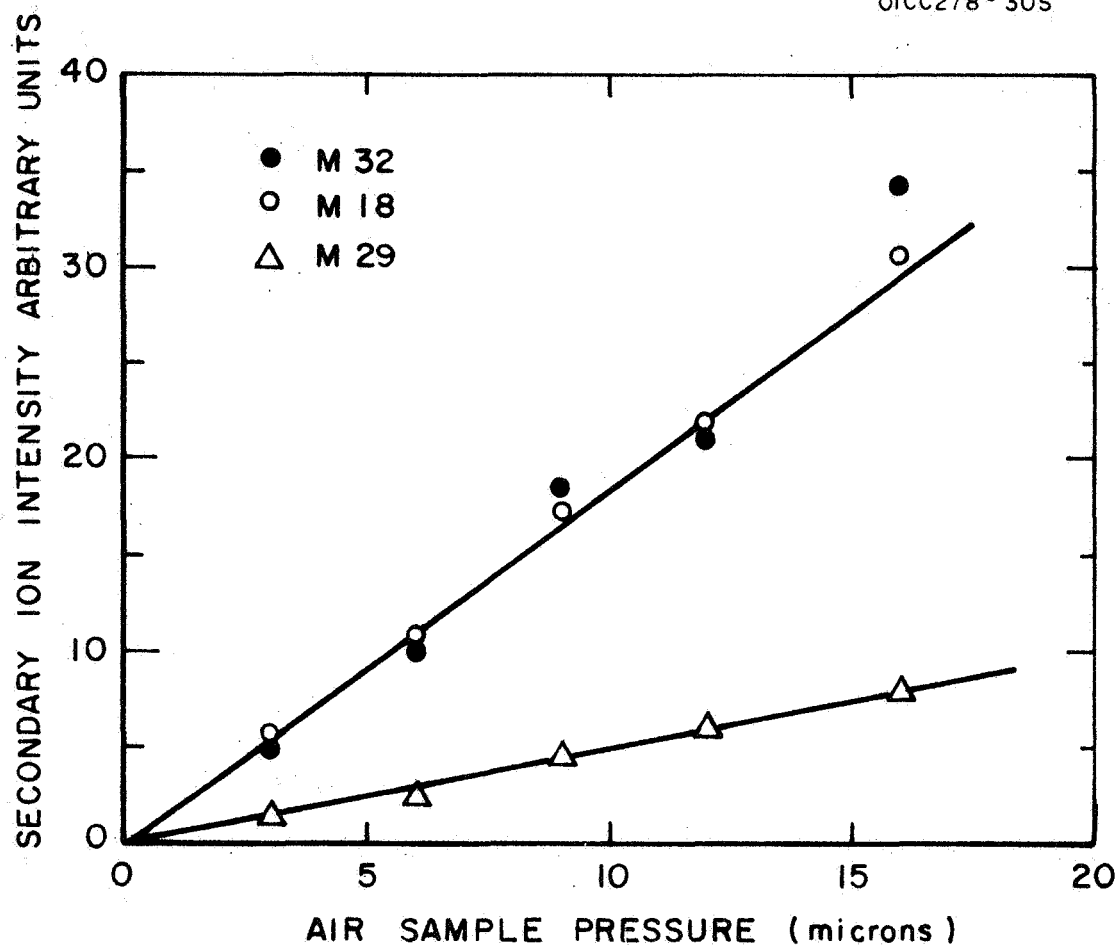


Figure 30. Dependence of secondary ion intensities on sample pressure with air as sample gas.

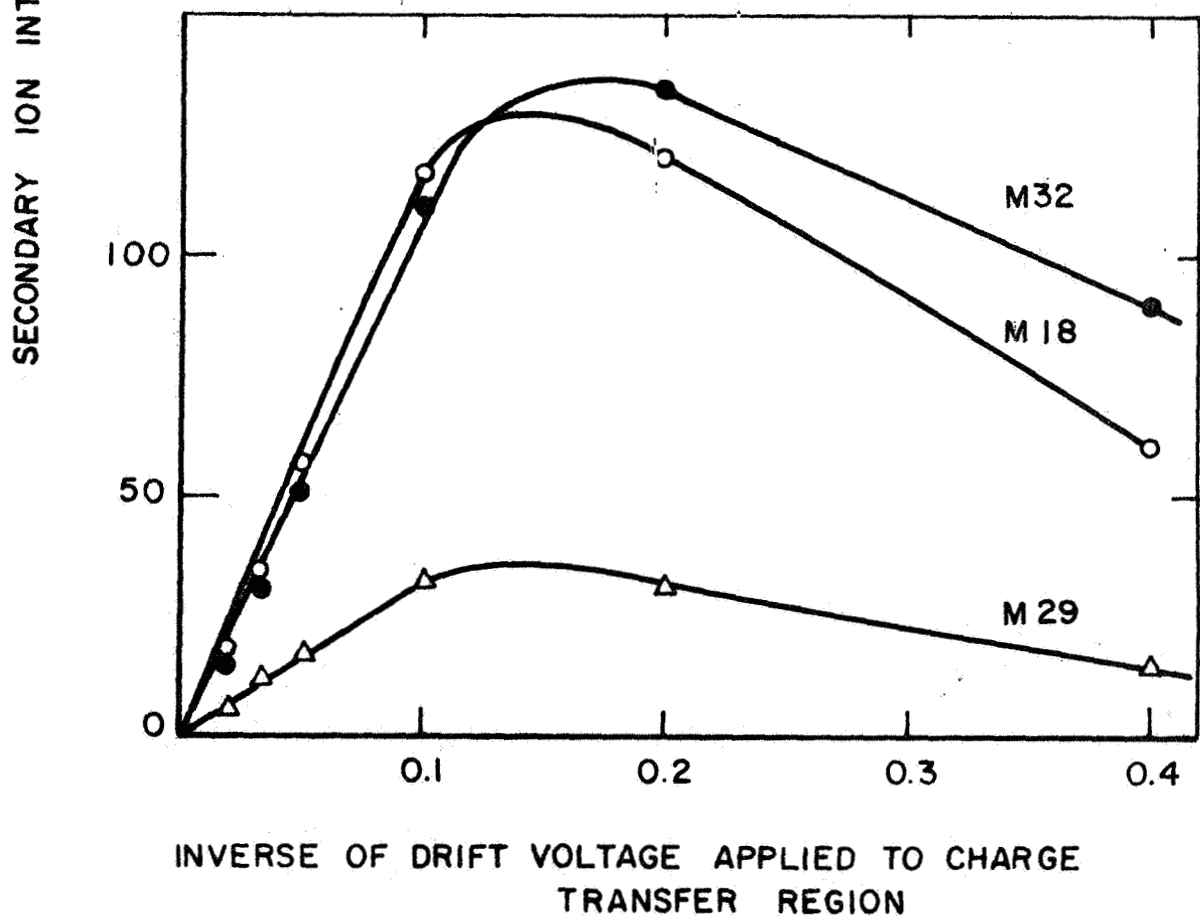
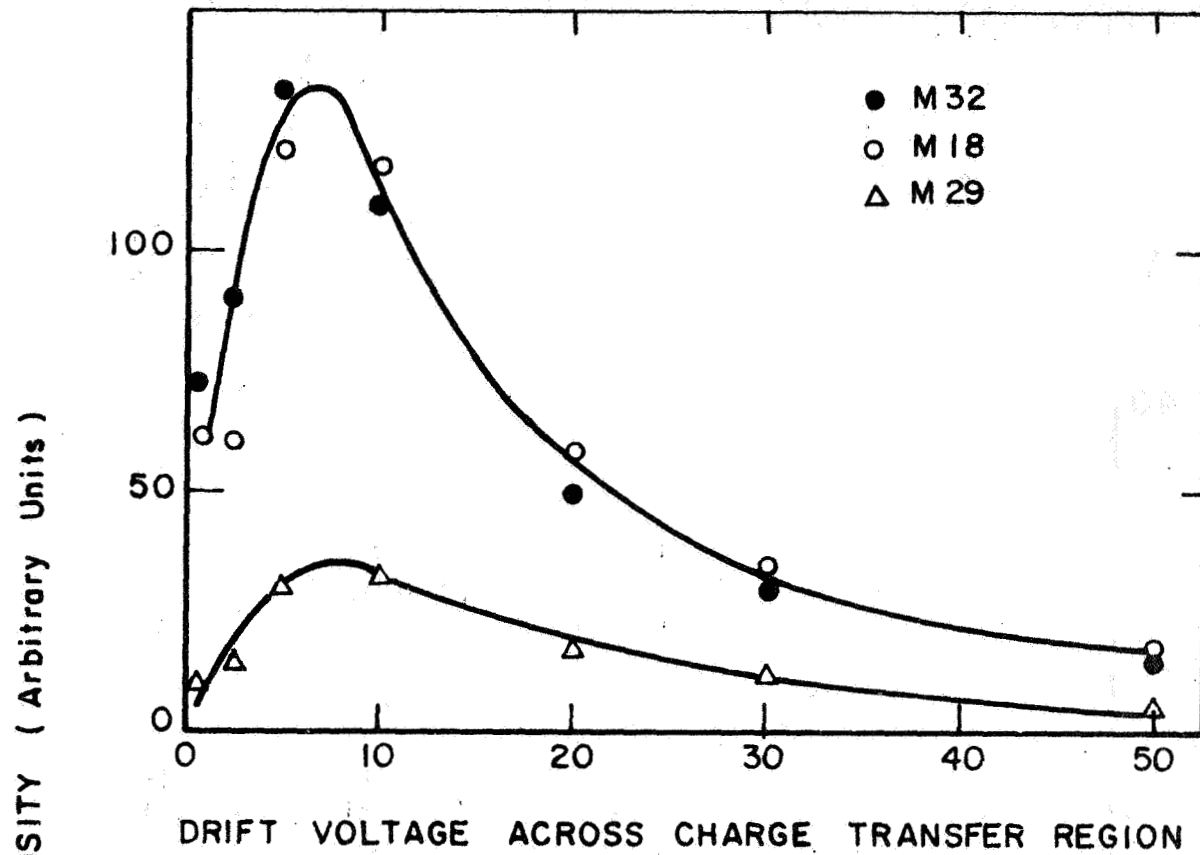


Figure 31. Variation of secondary ion intensities with drift voltage, and inverse drift voltage, respectively, applied to charge transfer gap. Air sample, krypton carrier gas.

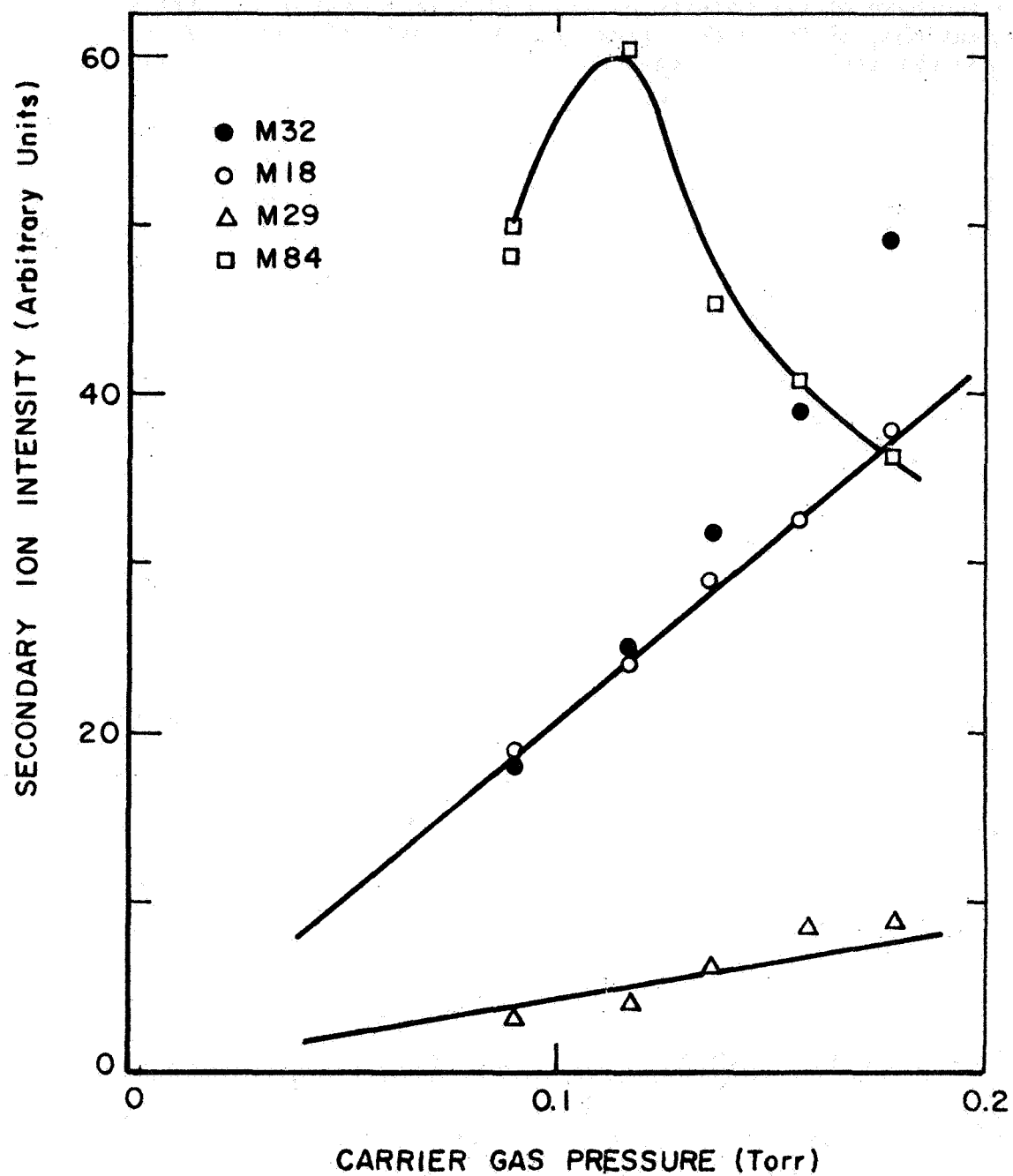


Figure 32. Dependence of primary and secondary ion intensities on krypton carrier gas pressure in the charge transfer region with 10 microns of air sample gas added.

time is increased. The secondary ion intensity, H_2O^+ , is quite linear with pressure, arguing against the importance of primary ion intensity variation. However, the intensities observed for O_2^+ and N_2H^+ are less linear with pressure. In the case of O_2 , the effect is caused in part by the introduction of source air impurity with the krypton which results in an increase of the background level at mass number 32. Despite these complications, it is evident from Figure 32 that the secondary ion intensities approximate the functional behavior with carrier gas pressure predicted by Equation (9).

From these results it can be concluded that the variation of secondary ion intensities with the three basic parameters: sample concentration, electric fields strength, and carrier gas pressure, are well described by Equation (9). Since in turn this equation rests upon the physical description of the processes responsible for secondary ion formation in the charge transfer region, it is demonstrated that the charge transfer ion source here tested operates according to the applied physical principles.

The usefulness of the charge transfer ion source as an analytical device depends to a large extent on the achieved sensitivity. In mass spectrometry, the sensitivity is often expressed as the ion current in amps per torr of sample pressure admitted, and these units will be used also here.

Sensitivities were determined using microwave excitation of krypton applying a push-out potential of 400 volts. The pressure in the charge exchange region was adjusted to 0.11 torr. With these conditions the primary ion intensity leaving the charge transfer region was maximized and amounted to 2×10^{-10} amps when the applied drift voltage was 30 volts. A variety of samples including carbon dioxide, carbon disulfide, nitrous oxide, ammonia, benzene and sulfur dioxide were investigated. Carbon dioxide and nitrous oxide were admitted directly to the ion source, but the other samples were prepared in flasks containing about 10 percent of the sample with helium as a buffer. The dilution with helium avoided as excessive loading of the charge transfer ion source and the resulting nonlinearities of ion currents at sample gas pressures sufficient for measurement with the McLeod gauge. The sample pressure admitted to the source was left below 10 microns so that it amounted to less than 10 percent of the total gas pressure. The sensitivities obtained for the present peaks are shown in Table X. They are of the order of 10^{-8} amps/torr. For comparison, it is noted that sensitivities for electron impact ionization typically are 10^{-5} amps/torr. Thus, the present sensitivities are by three orders of magnitude lower. However, electron-impact sources usually operate at sample pressures less than 10^{-4} torr, whereas the present device employs sample pressures up to 10^{-2} torr. The higher usable sample pressures compensate to a considerable extent the lower sensitivity. If in addition, a better extraction of ions from the drift region can be achieved, the usable ion currents available with the present device would compare very favorably with the ion currents achieved by electron impact.

TABLE X

SENSITIVITY OF CHARGE TRANSFER SOURCE FOR SEVERAL
SAMPLE GASES WITH KRYPTON PRIMARY IONS

Sample Gas	Pressure (Torr)	Mass of Parent Peak	Ion Current 10^{-11} (amps)	Sensitivity 10^{-8} amp/torr
Carbon dioxide	0.005	44	6.0	1.2
10% Carbon disulfide in helium	0.006	76	4.8	8.0
Nitrous Oxide	0.003	44	5.5	1.8
8% benzene in helium	0.015	78	8.8	7.3
9% ammonia helium	0.003	17	1.7	6.1
11% sulfur dioxide in helium	0.003	64	2.7	8.3

Several other factors must also be considered. Losses in the magnetic spectrometer used in these experiments amount to about 60 percent. These are not considered in Table X so that the ion currents emerging from the source are higher. In addition, it should be noted that the drift voltage and the carrier gas pressure in the charge transfer region were not optimized. These favorable factors are offset by the observation that with the present arrangement the microwave discharge resulted in enhanced fragment ion formation. In this respect, the use of the dc discharge was found more favorable, even though it is less intense. On the basis of these comments, it appears that the values listed in Table X provide a realistic assessment of attainable sensitivities.

d. Ionization processes other than charge transfer. — The overriding feature of the concept of charge transfer from ions having low kinetic energy as a technique for sample ion production in a mass spectrometer is the energy limitation imposed upon the charge transfer process by the recombination energy of the primary ion and the associated limitation of fragment ion formation. While the experiments discussed in the previous sections have demonstrated the feasibility of the method, they have also exposed an unexpectedly high production rate of fragment ions and of ions with ionization energies above that of the primary ions. This clearly undesirable effect made it necessary to investigate more systematically its origin so that appropriate remedies could be determined and applied.

Among a variety of possible causes for the formation of fragment ions are (1) a penetration of the plasma boundary into the charge transfer region; (2) tertiary reactions producing new species; (3) collisions of ions with excess kinetic energy; (4) back diffusion of sample gas into the discharge region; (5) reactions of doubly charged ions. These possibilities will be discussed below.

The direct interaction of the boundary of the discharge with the sample can take various forms depending upon the field and gas flow conditions in the vicinity of the orifice connecting the discharge and the charge transfer regions. The qualitative features of this interaction are exhibited by the data shown in Table XI which compares peak intensities observed with the microwave discharge and the dc discharge for several discharge field conditions with and without sample to the charge transfer region. The carrier gas was argon, the sample gas air, and the pressure and field in the charge transfer region were kept constant at 0.155 torr and 30 volts/cm, respectively. The main reactions are



TABLE XI

COMPARISON OF ION INTENSITIES FOR MICROWAVE AND DC DISCHARGE
WITH ARGON CARRIER AND AIR AS SAMPLE GAS

Type of discharge operation		Microwave			DC	
Push-out voltage		0		400	500	
Air sample pressure		0	10	10	0	10
Ion Intensity at Mass Number	14	6	6	5	-	6
	16	7	7	5	-	6
	17	2	2	2	-	1
	18	10	16	24	21	28
	19	27	47	2	-	3
	20	-	-	-	9	2
	28	7	27	91	2	41
	29	7	14	20	-	21
	30	135	160	12	4	4
	32	18	62	104	6	90
	33	-	15	-	-	2
	40 est	950	900	2300	1700	1700
	41	450	290	115	56	67
N_2^+ / O_2^+		-	0.46	0.98	-	0.45



The proton transfer from AH^+ is pronounced only when the push-out field in the (microwave) discharge is small so that a considerable intensity of AH^+ is produced by virtue of the enhanced interaction of argon ions with water vapor in the discharge. This effect is discussed in Section III,4,a. Of particular interest here is the relatively probability of charge transfer to nitrogen and oxygen. The ratio of ion intensities N_2^+/O_2^+ obtained with the dc discharge is $N_2^+/O_2^+ = 0.46$. That with the microwave discharge is $N_2^+/O_2^+ = 0.45$, when the applied push-out potential is zero, but the intensity ratio increases to $N_2^+/O_2^+ = 0.98$, when a high push-out potential of 400 volts is applied. The first two values are in perfect agreement with each other, despite the different discharge conditions, indicating that charge transfer is the predominant process of N_2^+ and O_2^+ formation. The observed value of $N_2^+/O_2^+ = 0.46$ is also consistent in magnitude with the approximately known values for the involved rate coefficients (Ref. 7). The increase of the N_2^+/O_2^+ value with increasing ion push-out field in the case of microwave excitation, therefore, points to an additional ionization process caused by a forced penetration of the plasma into the charge transfer region. Plasma intrusion is possible because the plasma forces between ions and electrons resist their separation and only after their concentration is sufficiently reduced by the spreading of the plasma will they move independently of each other so that they can be separated by the electric field. The resulting presence of electrons in the reaction region makes electron impact the most probable process of sample gas ionization in addition to charge transfer. This conclusion is similar to that reached in Section III,4,a on different grounds. Another conceivable process, the increase of the kinetic energy of the primary ions in the fringe field of the plasma cannot be made responsible for the increase in nitrogen ionization because the ions are accelerated most while passing the cathode fall region of the dc discharge without, however, causing the relative N_2^+ intensity to increase.

A further example for the different action of the microwave and the dc discharge is shown in Figure 33 which displays spectra obtained with krypton as the carrier gas and sulfur dioxide as the sample. The upper two traces were obtained with microwave excitation. They demonstrate a considerable fragmentary ionization by peaks of M48 (SO^+) and 32 (O_2^+ and/or S^+). In the lower traces, obtained with dc discharge operation, the fragment peaks are absent. Nevertheless, ionization other than by charge transfer must also occur with the dc discharge in view of the nitrogen ionization observed when air is used as a sample and krypton is the

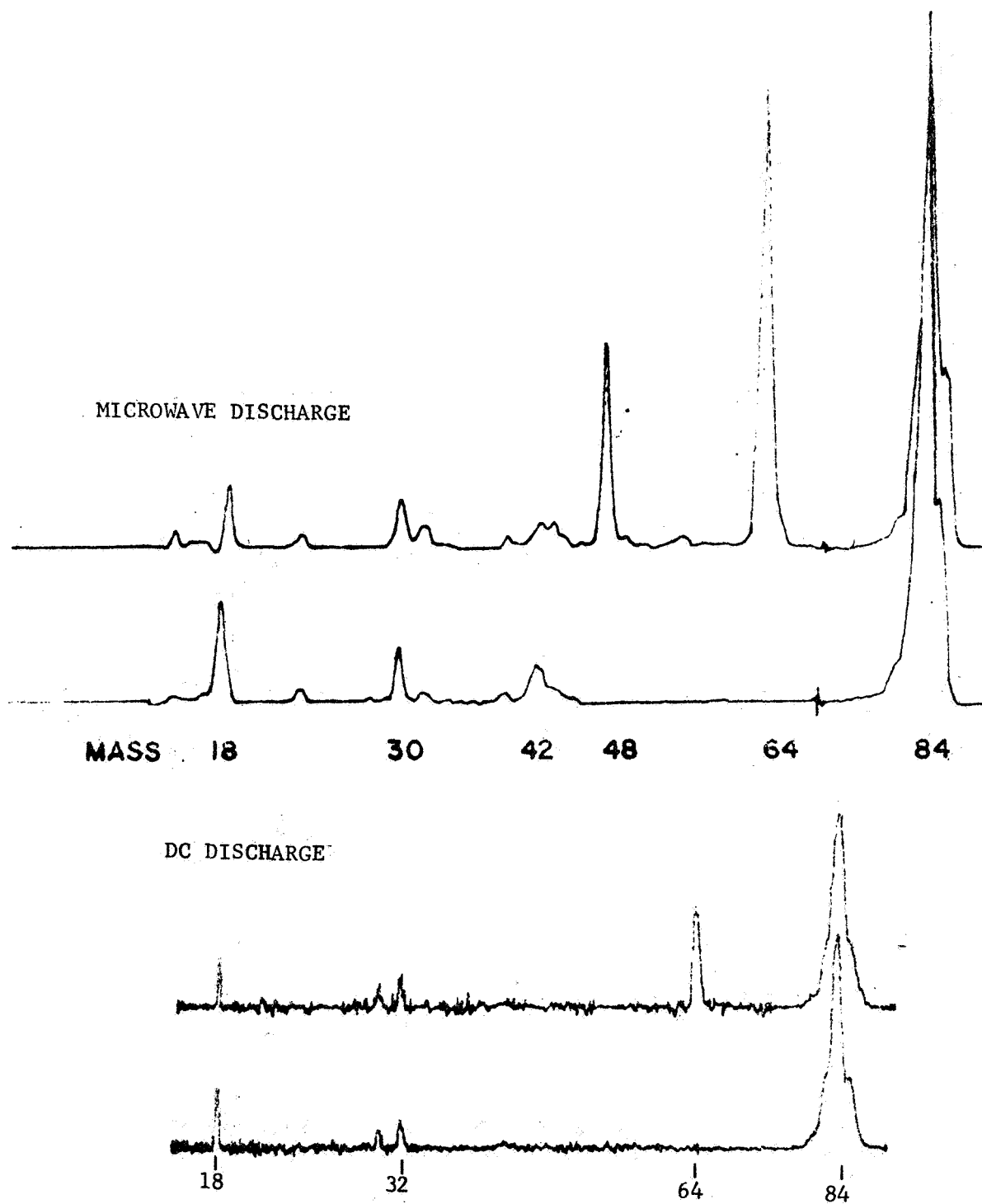


Figure 33. Comparison of mass spectra obtained with and without SO_2 sample gas for microwave and dc discharge conditions.

carrier gas. Accordingly, a number of experiments were performed with nitrogen and the krypton dc discharge.

For nitrogen as the sample gas, ionization by tertiary reactions, i.e., ionization by secondary ions, can be ruled out because of the high ionization potential of nitrogen. Indeed, in many respects, the observed N_2^+ ion current behaved similar to that of other secondary ions. For example, the N_2^+ intensity was linear with the nitrogen sample concentration in the charge transfer chamber. Figure 34 shows the variation of the N_2^+ current with the drift voltage applied to the charge transfer region. The observed functional behavior is identical to that of other secondary ions (viz. Figure 31), i.e., the N_2^+ intensity first reaches a maximum, then declines with approximately inverse proportionality to the drift voltage. This behavior is opposite to that expected if nitrogen were ionized by primary ions having gained kinetic energy from the electron field so that this process can be ruled out.

Figure 34 also shows an increase in the primary ion intensity with increasing drift voltage. These ions are known to have their origin in the discharge. Since the N_2^+ intensity decreases as the Kr^+ ion current increases, it is apparent that N_2^+ is not formed directly in the discharge. This conclusion argues against the significance of back diffusion into the discharge, but it does not preclude an interaction of N_2 with the boundary of the discharge. To test the second possibility, the influence of the pressure on the N_2^+ intensity was investigated. The results shown in Figure 35 demonstrate a decrease of N_2^+ formation with increasing pressure, in contrast to the behavior of O_2^+ and H_2O^+ which have been shown to occur by charge transfer involving Kr^+ . Also plotted in Figure 35 is the signal due to N^+ to indicate its co-variance with N_2^+ . The decrease of nitrogen ion intensities with increasing pressure is indicative of some back diffusion of sample gas into the discharge boundary region and a suppression of this effect with an increase in pressure. Since the concentration of sample diffusion along the orifice channel in opposite direction of the gas flow decreases markedly with the distance from the channel end, the 0.06-cm diameter and 0.06 cm long orifice was replaced by a similar orifice 0.5 cm long, and 0.1 cm in diameter. The wider channel permitted an equivalent gas flow. The results obtained with the second orifice were inconclusive. The N_2^+ ion currents were indeed smaller but so were the primary krypton currents, presumably due to a less efficient primary ion extraction. Thus, the N_2^+/Kr^+ ratio should be used as the appropriate indicator for any attained improvement. On the average, this ratio was by a factor of 1.7 lower when the long orifice was used in place of the short orifice. While the decrease of the N_2^+/Kr^+ ratio may be considered an improvement, it falls far short of the expected reduction by at least an order of magnitude. It is, however, difficult to predict the discharge boundary in the vicinity of the orifice with any accuracy due to the strong dependence on flow and field conditions which are unknown. As a consequence it appears that a reasonably effective elimination of the sample gas-discharge interaction can be achieved only by a differentially pumped gap separating the discharge from the charge transfer region. This feature would complicate the simple design of the present source, since it

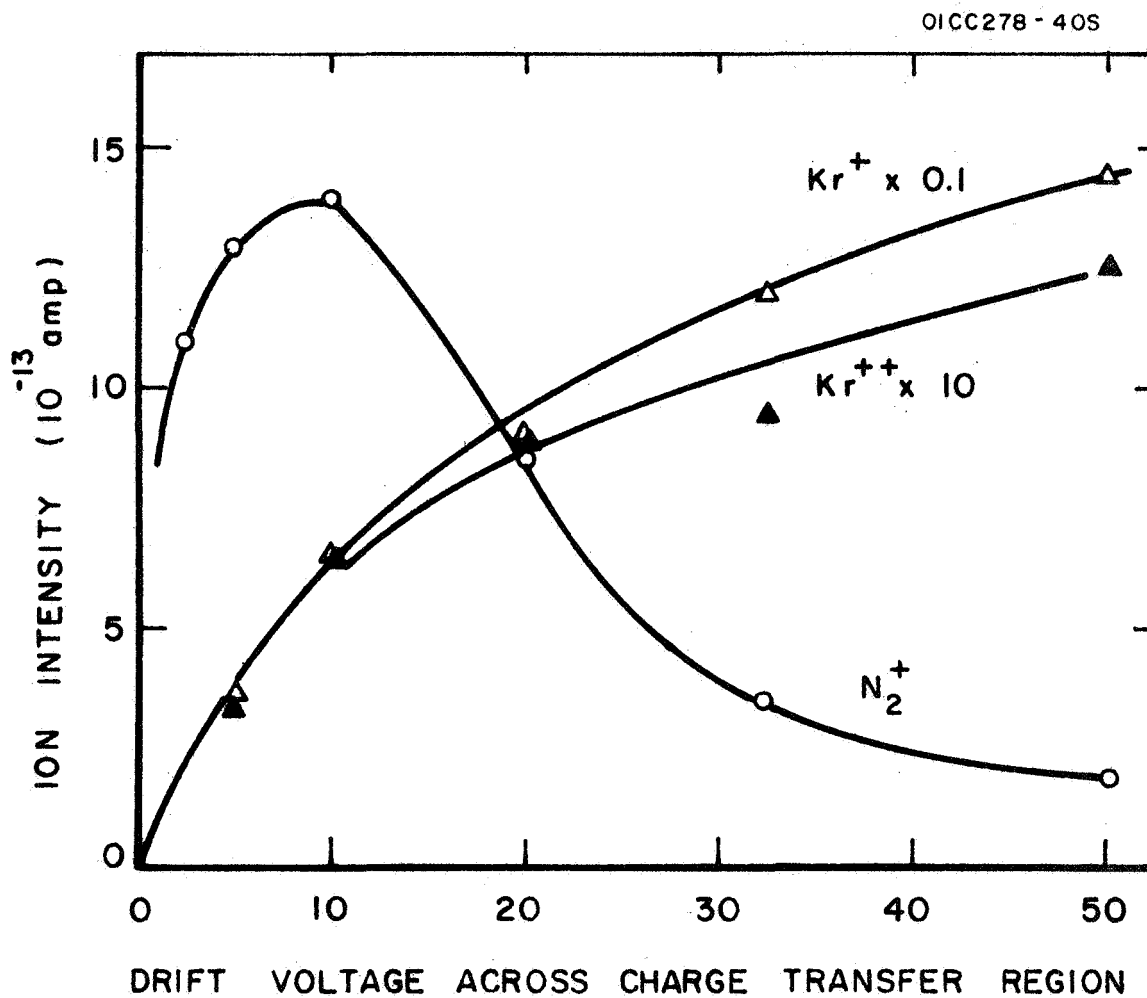


Figure 34. Dependence of ion intensities of N_2^+ , Kr^+ , Kr^{++} on drift voltage applied to charge transfer gap; krypton carrier and nitrogen sample gas.

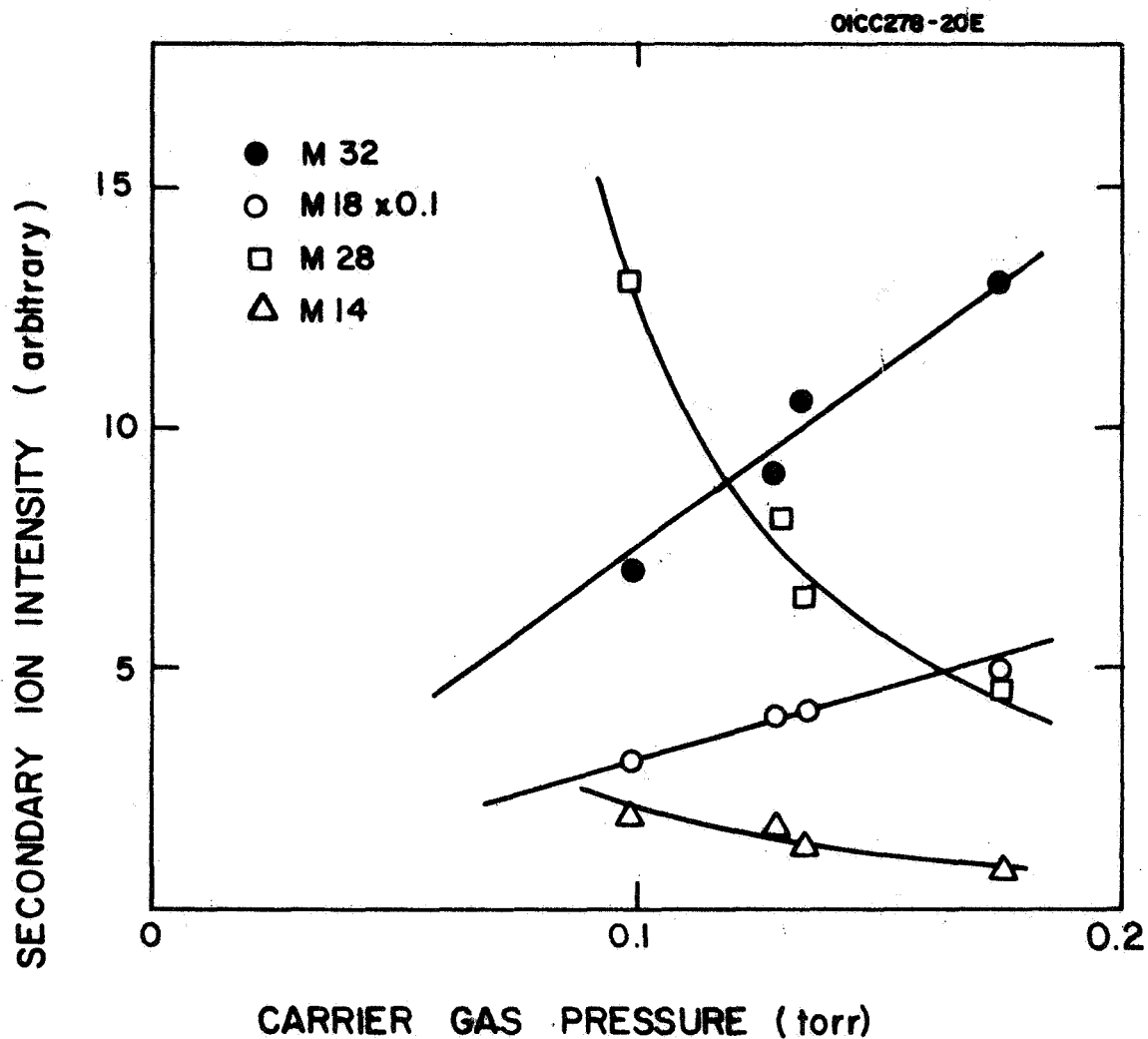


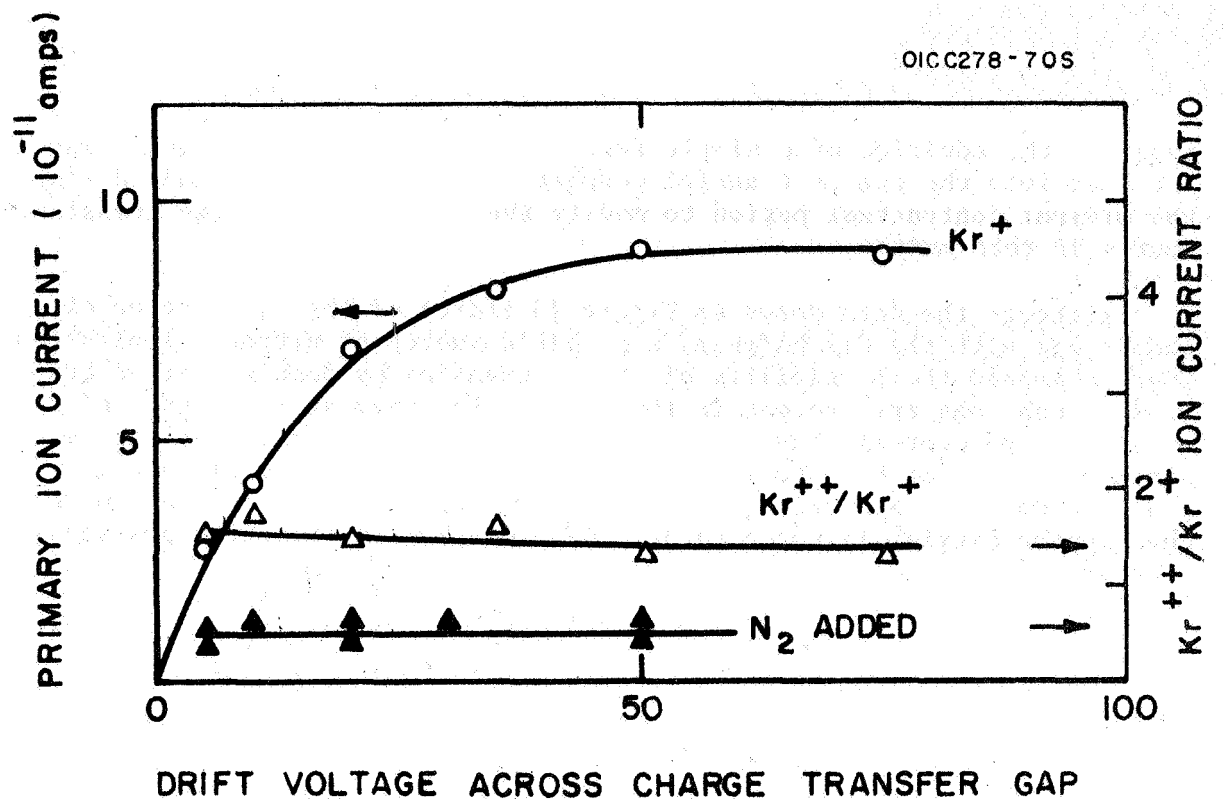
Figure 35. Dependence of ion intensities of O_2^+ (M32), H_2O^+ (M18), N_2^+ (M28) and N^+ (M14) on krypton carrier gas pressure in the charge transfer region. Nitrogen sample gas.

requires the addition of a simple focusing element to direct the primary ion beam into the charge transfer chamber. No attempts were made during the present contractual period to modify the feasibility charge transfer source in this manner.

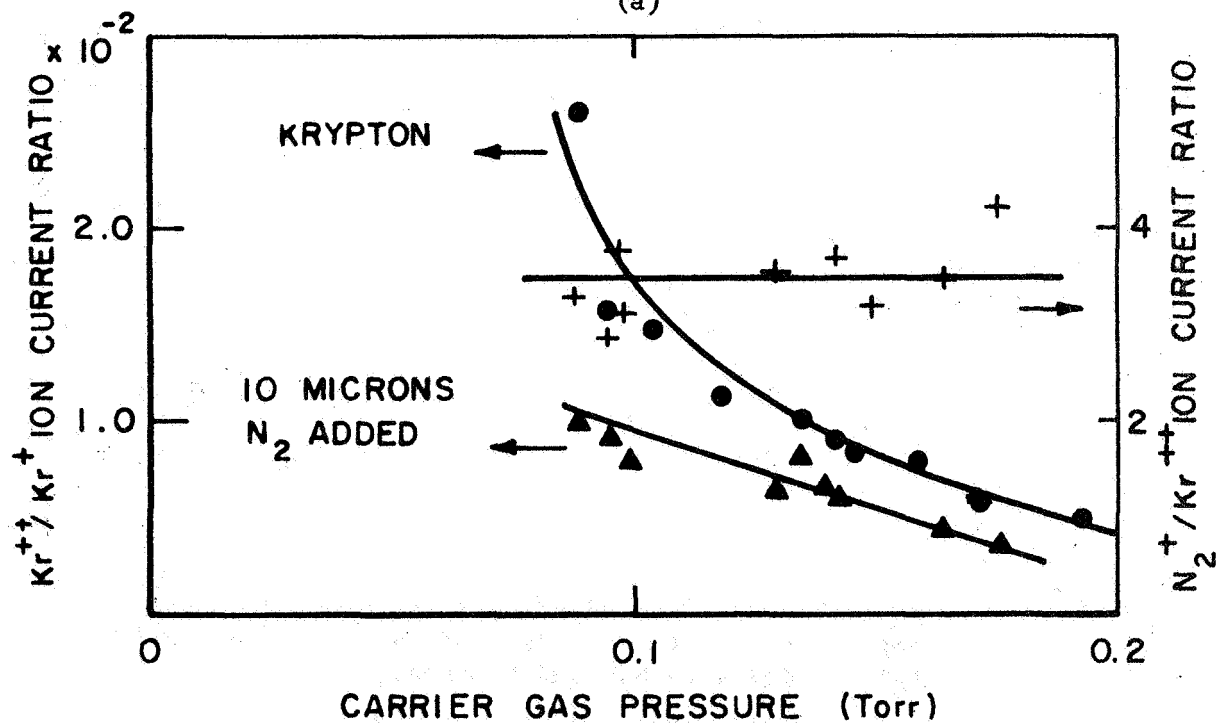
Although the data shown in Figure 35 indicated the interaction of sample gas with the discharge as a probable source of nitrogen ionization, there remained the possibility of charge transfer by doubly charged krypton ions. Such ions are present in the primary ion beam at a concentration of about 1 percent of that of singly charged krypton ions. The recombination energy of Kr^{++} to give Kr^+ is 24.6 eV which is sufficient to generate not only N_2^+ but also N^+ . In addition, a charge exchange with the krypton carrier is conceivable. Accordingly, the reaction possibilities are



This mechanism could conceivably explain the decrease of N_2^+ and N^+ with increasing pressure (Figure 35) either by the increasing influence of Reaction (23), or simply by a decreasing production of Kr^{++} in the discharge as the pressure is raised. Figure 36a shows the ratio of $\text{Kr}^{++}/\text{Kr}^+$ ion currents as a function of the applied drift voltage in the charge transfer chamber, with and without the presence of nitrogen. In both cases, the ratio remains constant despite the variation of the ion residence time with varying drift voltage. It is clear that this behavior excludes a significant influence of Reaction (23). Further data are given in Figure 36b to show that the $\text{Kr}^{++}/\text{Kr}^+$ ion intensity ratio decreases with increasing pressure so that indeed a decrease in the relative Kr^{++} production rate occurs. However, the ratio $\text{N}_2^+/\text{Kr}^{++}$ of the ion intensities remains essentially unaffected by the pressure variation, whereas it should increase with pressure, due to the increased Kr^{++} residence time if Reaction (21) were a significant source of N_2^+ . Clearly, the results in Figures 36a and 36b do not completely preclude the occurrence of Reactions (21), (22), and (23), but the preponderant process for nitrogen ionization must be different. Accordingly, it is concluded that the interaction of sample gas with the boundary of the discharge remains the principal cause for the observed N_2^+ and N^+ ions.



(a)



(b)

Figure 36. (a) Dependence of the Kr^{++}/Kr^{+} ion current ratio and the Kr^{+} ion intensity on the drift voltage applied to charge transfer gap with and without the addition of nitrogen sample gas. (b) Dependence of the Kr^{++}/Kr^{+} and the N_2^{+}/Kr^{++} ion current ratios on the krypton carrier gas pressure in the charge transfer space.

5. Conclusions and Recommendations

The results obtained with the charge transfer ion source can be briefly summarized as follows: Primary ions of krypton (or argon) produced in a discharge source enter into a reaction region where they drift in a weak electric field and are mainly discharged on the walls of the chamber. Charge transfer and proton transfer to a sample gas introduced to the reaction region create secondary ions which are extracted and analyzed with a magnetic mass spectrometer. The intensity of secondary ions increases with increasing primary ion currents, with increasing sample concentration and with increasing residence time of the primary ions in the charge transfer chamber. Sensitivities achieved are of the order of 10^{-8} amps/torr. This is several orders of magnitude lower than sensitivities observed with electron impact; however, no pronounced disadvantage results from the lower sensitivities, since the applicable sample pressures can be higher. The present source configuration requires extraction fields of 5 volts/cm or higher. At lower field strength the extraction efficiency decreases.

The present investigation has exposed two major problem areas associated with the test design. One is the perturbing influence of impurities in the carrier gas upon the composition of the primary ion beam; the other is the ionization of sample gas by processes occurring in addition to charge transfer, mainly the interaction of sample gas with the boundary of the discharge in the primary ion source.

To remedy this situation, it appears that a redesign of the charge transfer ion source is required. The improved ion source would have to be bakable so that off-gassing of impurities from the walls can be reduced, and a cleaner inlet system for the carrier gas should be installed. In addition, the ionization of sample gas by the fringe of the discharge must be eliminated. Implementation of these design changes is expected to result in an improvement of the primary and secondary ion mass spectra to the point where trace gas analysis becomes feasible.

IV. RESONANCE SCATTERING FOR HIGH AND ULTRA-HIGH VACUUM PRESSURE GAUGE CALIBRATION

1. Introduction

In the ultra-high vacuum region, at pressures below 10^{-8} torr, pressure measurements are customarily performed with ionization gauges. The operating principle of an ionization gauge is the ionization of residual gas molecules by electrons generated at a filament. The resulting ion current is measured at a collector electrode. To increase the electron path and thereby increase the collision probability at low gas pressures the electrons are made to oscillate across a grid which is kept at positive potential with respect to both, the filament and the ion collector. In the intermediate pressure range, the observed ion current is proportioned to the gas pressure, but nonlinearities are observed both at high and at low pressures. The high pressure nonlinearity is due to saturation effects. It becomes noticeable above 10^{-4} torr. At low pressures below 10^{-10} torr, the nonlinearity is caused by a residual current due to the interaction with the collector of X-rays produced at the grid by fast electrons. These factors, as well as the dependence of ionization efficiencies upon the type of gas present make it necessary to calibrate the ionization against a standard before use.

Absolute pressure measurements are customarily performed with the McLeod gauge. Unfortunately, it is an accurate instrument only at pressures greater than 10^{-3} torr, although useful accuracies are still available in the 10^{-4} torr range. In using the McLeod gauge as a standard for the calibration of an ionization gauge, it is clear that the range of overlap is small, and one has to rely upon an extrapolation to determine the calibration of the ionization gauge at pressures less than 10^{-4} torr. Although the extrapolation procedure is often used, it must be applied with caution in view of the nonlinear response of the ionization gauge in the pressure region overlapping with that of the McLeod gauge. Moreover, the nonlinearity of the ionization gauge at pressures below 10^{-10} torr invalidates the extrapolation to this low pressure regime, so that at low pressures an absolute calibration is precluded.

In searching for methods that could overcome these difficulties it has been suggested that a resonance scattering technique might provide a suitable secondary standard for the calibration of the ionization gauge. Owing to the comparatively large cross sections associated with atomic resonance absorption ($\sigma \approx 10^{-13}$ cm² in the center of the line), resonance scattering can be a very sensitive technique for the detection of atomic species. In the concentration range where losses of intensity by light absorption are negligible, the scattered signal is strictly proportional to the pressure of the scatterer. Thus, it is expected that compared with the ionization gauge, resonance scattering will provide a more

reliable linear extrapolation to low pressures, starting from the pressure range in which calibration with a McLeod gauge is feasible. Because its use is restricted to stable atomic species such as rare gases, resonance scattering cannot replace the ionization gauge; however, it would provide a very valuable calibration aid.

In this section of the report the feasibility of resonance scattering in the high and ultra-high vacuum region is explored. Xenon was selected as the scattering gas, because its first resonance line at 1470\AA lies in a wavelength region accessible by window materials and detectors. The other rare gases, with exception of krypton, have their resonance lines affected by the transmission cut-off of lithium fluoride. A schematic diagram of the resonance scattering geometry and the involved components is shown in Figure 37a. The setup incorporates a collimated xenon light source, and a uv photomultiplier detector viewing the scattering chamber so that direct exposure to the incoming radiation is avoided. Wood's horns are employed to eliminate back scattering from walls.

The efficiency of such a system is determined to a large extent by the efficiency of the light source. The requirements placed upon the light source, in fact, are unique in comparison to lamps for almost any other purpose in that one requires not only a high intensity but also an emission line width as narrow as possible in order to achieve a good overlap of the emitted line shape with that of the absorption line of the gas in the scattering chamber. Optimum conditions would be obtained, if the line width of the emitting line were narrower than that of the absorption line, but this situation usually cannot be accomplished in view of the elevated temperatures of the light source emitter gas and the resulting line broadening. In addition it is found that measures taken to reduce the line width of a light source also decrease the emitted intensity. Consequently, one has to determine empirically the optimum operating conditions for a given light source. This report discusses the results for three different sources: (1) a small dc cold cathode discharge source, (2) a mildly condensed ac discharge source and (3) a microwave powered discharge source. The characteristics of the dc discharge source were described in detail in a previous report (Ref. 9) and it is used here mainly for comparison. The following sections give first the theoretical background for resonance scattering, then describe the experimental apparatus and procedures. The results and their implications are discussed subsequently.

2. Theoretical Considerations

The two important parameters of a resonance light source are its intensity and the spectral distribution of the emitted resonance line. Both parameters are determined to a large extent by the number density of the resonance atomic species in the source. If excitation occurs by electron collision, the probability of excitation increases with the number density of the atoms. At the same time, however, a portion of the emitted radiation is trapped due to the increased self-absorption. The combination

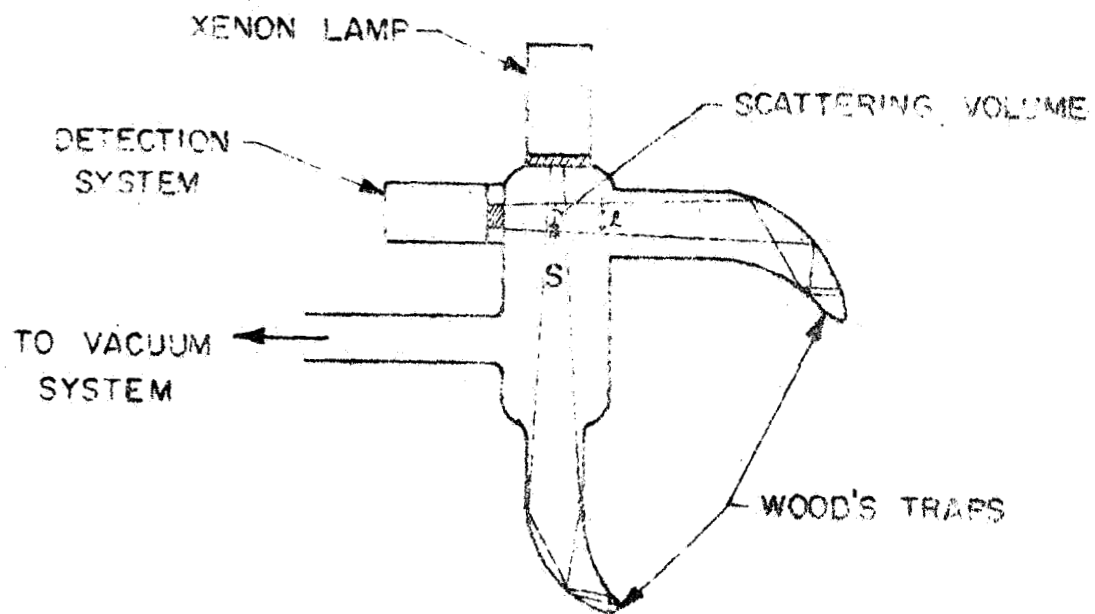


Figure 37a. Principle of resonance scattering.

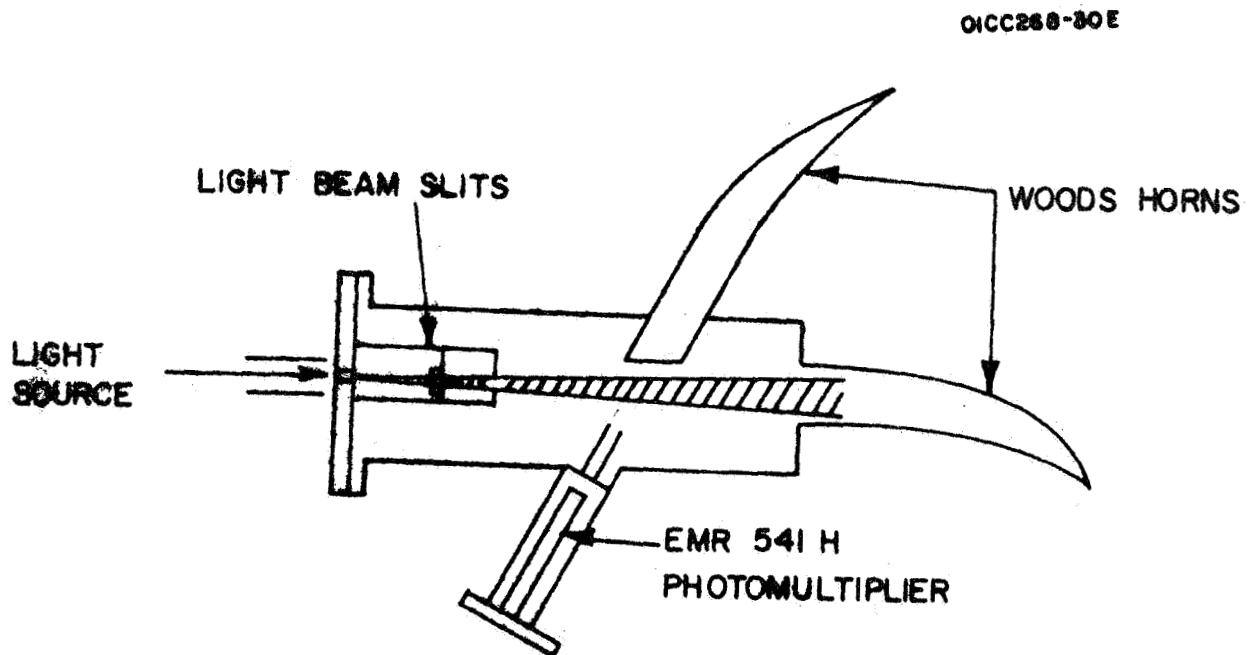


Figure 37b. Resonance scattering apparatus.

of both effects broadens the emitted line. The line shape is further determined by the thickness of the cool gas layer in front of the window from which the radiation emerges. A considerable absorption in the cool gas layer may reduce the emission in the line center to negligible levels. Since these factors cannot easily be estimated, it is convenient to represent the emission intensity of the resonance line as a product of the total line intensity I_0 in photons/cm²-sec and a normalized distribution frequency function $g(\nu)$ such that the intensity falling into the frequency interval $d\nu$ is given by

$$dI = I_0 g(\nu) d\nu \quad (24)$$

If it is assumed that the source emission falls into a narrow cone directed completely into the scattering chamber, and that the detector views a small volume given by the averaged geometric cross section of the light beam and the length ℓ as indicated in Figure 37a the amount of light absorbed is

$$dI_a = SI_0 \sigma(\nu) n \ell g(\nu) d\nu \quad (25)$$

where n is the prevailing number density of scatterer, and $\sigma(\nu)$ is the absorption cross section at frequency ν . Commonly, the absorption cross section is given by its Doppler shape

$$\sigma(\nu) = \sigma_0 \exp \left(- \left(\frac{\nu - \nu_0}{\nu_D} \right)^2 \right) \sqrt{\ln 2} \quad (26)$$

where σ_0 is the absolute cross section in the center of the line, ν_0 is the frequency at the line center, and ν_D is the Doppler width. It may be noted however, that far from the center, the absorption cross section given by the natural line width is greater than the Doppler cross section, so that the above expression holds only at frequencies close to the center of the line. If the overall number density in the scattering chamber is sufficiently low so that collisional quenching can be neglected, all of the absorbed radiation is emitted omnidirectionally as scattered radiation, so that $dI_a = dI_s$. Due to geometric factors, the detector will receive only a fraction α of the total scattered light. Thus, the intensity received by the detector is

$$dI_s = \alpha VI_0 n \sigma(\nu) g(\nu) d\nu \quad (27)$$

where $V = S \ell$ is the viewed scattering volume. The total scattering intensity received by the detector is that obtained by integrating over the frequency domain:

$$I_s = \alpha V I_0 n \int_0^{\infty} \sigma(\nu) g(\nu) d\nu = \alpha V I_0 n \bar{\sigma} \quad (28)$$

It can be seen that the integral represents an average over the absorption cross section $\sigma(\nu)$. Accordingly, the average or effective absorption cross section is denoted by $\bar{\sigma}$. With this representation, it becomes apparent that the most effective light source would be one that maximizes the product of the intensity and the line shape such that the product $I_0 \bar{\sigma}$ is a maximum. Therefore, the most effective light source conditions can be determined experimentally by observing the scattered light signal and locating its maximum as a function of discharge source parameters. This has been the main procedure in the present work in order to evaluate the three resonance sources under consideration.

3. Feasibility Calculations

The EMR 541 uv sensitive photomultiplier detector employed in the present studies features a cathode conversion efficiency γ of about $\gamma = 0.05$ at 1470\AA . This figure must be lowered however, when radiation losses due to additional windows occur, and when the photomultiplier is operated in the pulse counting mode and pulse height discrimination is used. With these conditions, the effective efficiency is $\gamma \approx 0.01$. The geometric factor α in Equation (28) can be estimated for the present system as $\alpha \approx 0.01$. Similarly, the viewed scattering volume is $V = 1 \text{ cm}^3$. The effective scattering cross section must be less than that valid for the center of the absorption line, $\sigma_0 \approx 2 \times 10^{-12} \text{ cm}^2$. Indeed, the previous study (Ref. 9) involving the dc light source indicated that $\bar{\sigma} \approx 10^{-14} \text{ cm}^2$. The light intensity for that source was estimated as $I_0 = 1 \times 10^{10} \text{ photons/cm}^2$ but it has since been found that the lithium fluoride windows in the scattering chamber had deteriorated to less than half their original transmittance. Accordingly, one can set $I_0 \approx 5 \times 10^{10} \text{ photons/cm}^2$ for the dc lamp. The count rate observed with the detector is then given by

$$N_c = \alpha \gamma V I_0 \bar{\sigma} n = 10^{-2} \times 10^{-2} \times 5 \times 10^{10} \times 10^{-14} \times n = 5 \times 10^{-8} n$$

For example, at a pressure of 1×10^{-7} torr the number density at 300°C is $3 \times 10^9 \text{ cm}^{-3}$. The corresponding count rate would be 150 counts/sec.

Consider now the detector noise level. It was observed that background scattering off the walls of the scattering chamber was negligible for the dc light source in comparison with the dark current of the detector

which amounted to 10 counts/sec when the pulse height discriminator was set to an optimum level. Accordingly, if a signal to noise ratio of unity is acceptable, the lower limit detectable xenon number density is about $2 \times 10^8 \text{ cm}^{-3}$, corresponding to about 6×10^{-9} torr. Evidently, with the use of the dc light source and the EMR 541 H photomultiplier, the ultra-light vacuum range cannot be covered. To do this, either the light source intensity, or the detector sensitivity, or both must be improved.

Recently, Bendix has made commercially available a unique device specifically suited for photon counting in the vacuum ultraviolet spectral region named the Channeltron UV Photon Counter. This unit features an amplification different from the customary dynode chain and produces essentially no dark current other than that from the photocathode. If operated at high gain (approximately 10^8) the quasiexponential pulse height distribution, characteristic for most multipliers, is changed to a Gaussian distribution displaced from the origin, so that a much more effective pulse height discrimination against the dark current can be achieved. In addition, the Bendix Channeltron Photon Counter is equipped with an opaque photocathode rather than a transparent one as featured by the EMR photomultiplier. The opaque photocathode achieves a higher conversion efficiency of about 10 percent. Both factors are estimated to result in an improvement by as much as a factor of one hundred over the EMR photomultiplier. This would place the lower limit pressure at 6×10^{-11} torr. Although this pressure is low enough to permit coverage of most of the ultra-high vacuum domain by resonance scattering techniques, it is not yet sufficient to allow an assessment of the low pressure nonlinearity of an ionization gauge. It is apparent that more intense and/or more effective light sources are required. The remainder of this report is devoted to an investigation into that aspect.

4. Apparatus

The scattering apparatus is shown in Figure 37b. Its detailed description was given previously. Briefly, it consisted of a stainless steel cylindrical chamber provided with a 5-inch flange for the attachment of a light source, an adjacent detector compartment, and two Wood's horns made of glass, one opposite the light source and one opposite the detector. The chamber was connected to a high vacuum system. The incident light beam passed two sets of confinement bars, the first of which carried a lithium fluoride window. The resulting dead space was evacuated with an auxiliary mechanical pump. The detector compartment was isolated from the chamber by another lithium fluoride window, and was pumped separately to a high vacuum so that absorption of air and possible arcing from high potentials were avoided.

The detector was an EMR 541 H photomultiplier. Its copper iodide photocathode is insensitive to visible light and has a maximum response in the vacuum uv spectral region. The applied cathode potential was -3000 volt. The detector was used either in the dc or in the pulse counting mode. In the former case the current was observed with a Keithley picoammeter; in the latter case the signal was processed with Hamner equipment and integrated with a rate meter. The signal for both systems was recorded with a Leeds and Northrup strip-chart recorder.

Three different types of pressure gauges were used to monitor pressures in the light sources and in the chamber: a conventional McLeod gauge covered the pressure range 1 to 10^{-4} torr; two calibrated thermocouple gauges were used in the 1 to 20 torr and the 10^{-3} to 10^{-1} torr regions; and a Veeco ionization gauge was used for the 10^{-3} to 10^{-6} torr range. The ionization gauge served mainly to monitor the progress in evacuating the chamber, because it was found that despite a calibration for xenon, its response was often sluggish and erratic. To achieve a better control of the xenon partial pressure in the scattering chamber, xenon was introduced as a xenon-helium mixture of 1/1000 ratio. Then pressures could be measured conveniently with the McLeod or a calibrated thermocouple gauge.

5. Light Sources

The three light sources examined were a small capillary dc discharge source, an ac triggered pulsed discharge lamp, and an electrodeless microwave discharge lamp. These sources will now be described.

The dc lamp had been investigated previously and was used mainly for comparison. It is shown schematically in Figure 38. This source features a capillary 25 mm long and 1 mm in diameter. The spacing between the capillary end and the sapphire window is 2.5 mm. The source is connected to a 1500 volt dc power supply via a 5 megohm variable resistor, and draws a current up to 1 milliamperes. The attractive features of this source are its compactness, simplicity of operation, and the small angular spread (approximately 10 degrees) of the emitted radiation. Its draw back is the relatively low level of emitted intensity.

The geometry and dimensions of the ac pulsed source are shown in Figure 39. This source has been used frequently by Tanaka. It features a water cooled capillary 16 mm long and 7 mm in diameter and is made entirely of quartz. The electrodes are made from high purity coiled aluminum wire connected to an appropriate quartz to metal feedthrough seal. The quartz body of the source is fastened to a brass flange with epoxy cement. A 7 mm i.d. glass tube sealed off with a sapphire to a second flange was used in conjunction with the first flange to reduce the dead space between the discharge and the sampling window. The gas flow through the source was maintained with a mechanical pump and regulated with needle

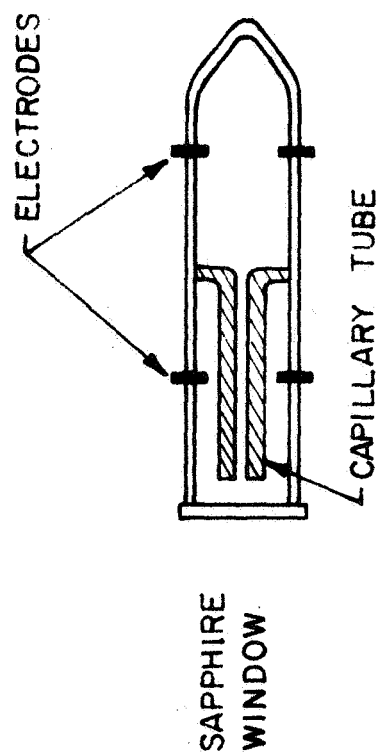


Figure 38. DC capillary discharge light source.

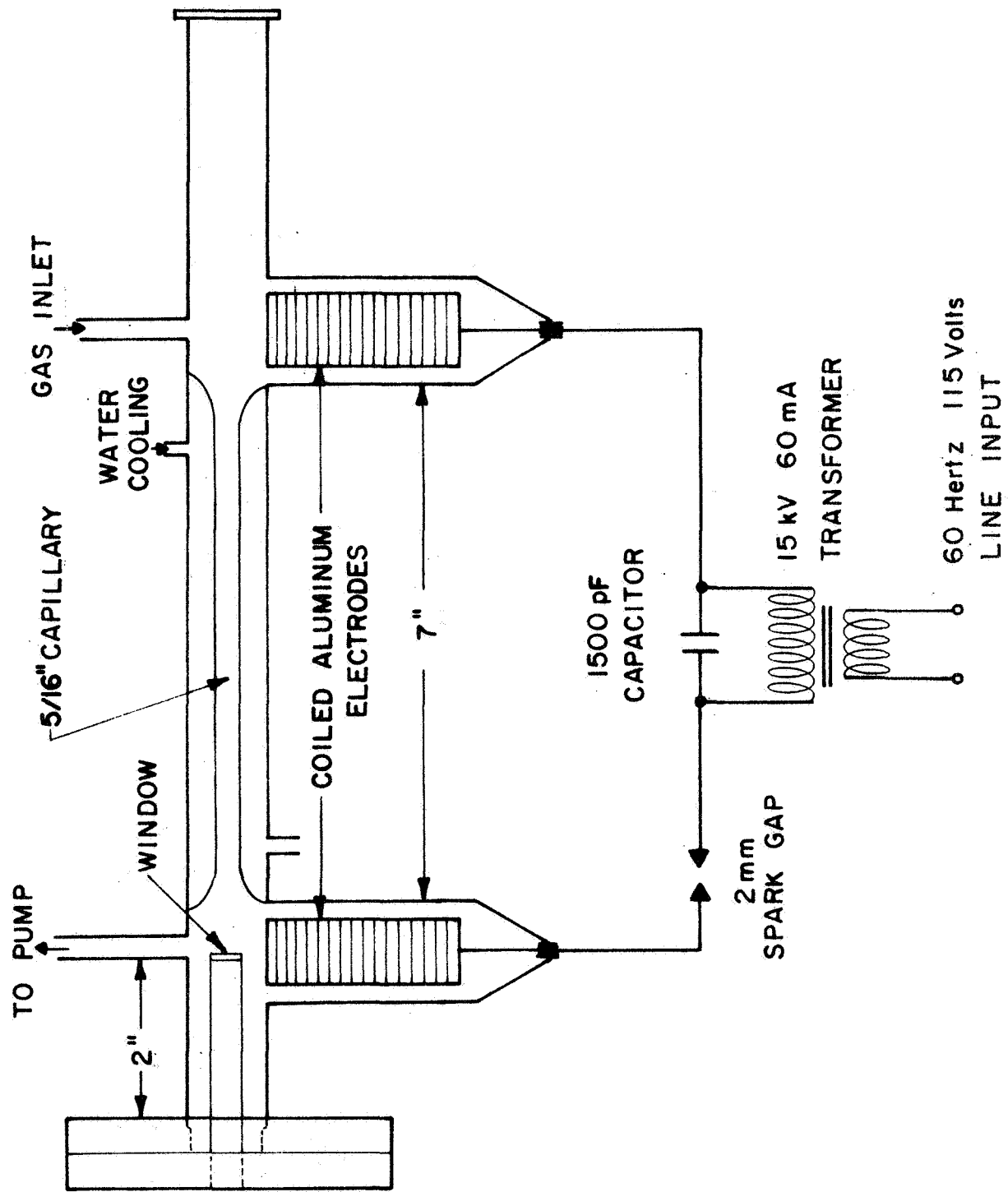


Figure 39. AC pulsed discharge light source.

valves. The ac source was powered by a 15000-volt transformer, acting on a bank of three 0.001-microfarad capacitors connected in parallel, and an adjustable spark gap in series with the discharge.

The microwave discharge source consisted of a 12.5 mm diameter quartz to pyrex graded seal attached to an appropriate brass flange with a swagelok coupling. It was powered from a 2450 megahertz Raytheon diathermic unit using an Evenson cavity clamped around the quartz section of the discharge tube. Cooling was effected by means of a compressed air stream. As with the ac source, the gas flow was maintained with a mechanical pump and controlled by needle valves. The microwave source was used in two ways; (1) with a window placed onto the flange, and (2) with a window at the end of a tube penetrating into the discharge region similar to its application with the ac source. In this manner the effect of the cool gas layer through which the radiation had to pass could be demonstrated. Both arrangements are shown schematically in Figure 40.

6. Results

On the basis of previous experience it was expected that the xenon pressure in the light source is a critical parameter in optimizing the source efficiency for resonance scattering experiments. In fact, since the xenon pressure determines to a large extent the degree of self-reversal present in the emitted line, a reduction of the amount of self-reversal requires relatively low pressures of xenon. Under these conditions the discharge must be stabilized by the addition of an inert carrier gas. In the present experiments helium was employed as the carrier. The determination of optimum conditions, therefore, required an investigation of the effect of the two gas pressures involved, that of xenon and that of helium. An additional parameter affecting the useful intensity of the light source is the discharge current or, in the case of the microwave discharge, the absorbed power.

To investigate the influence of these parameters, the xenon pressure in the scattering chamber was kept constant at approximately 1×10^{-5} torr, and the scattered light was observed with the photomultiplier detector operated in the dc mode. Figure 41 shows the variation of scattered light intensity with the helium pressure, all other parameters being kept constant. The optimum helium pressure is somewhat lower for the microwave and the ac pulsed light sources (1 to 3 torr) than for the dc lamp which maximizes at 8.5 torr, but the maxima are rather flat indicating that the helium pressure adjustment is not critical.

By contrast, the dependence of the optimum performance upon the xenon partial pressure is more pronounced as demonstrated in Figure 42. It is seen that for the microwave and the ac pulsed light sources the optimum xenon pressures are by about an order of magnitude higher than for the dc discharge. This behavior is probably related to a more

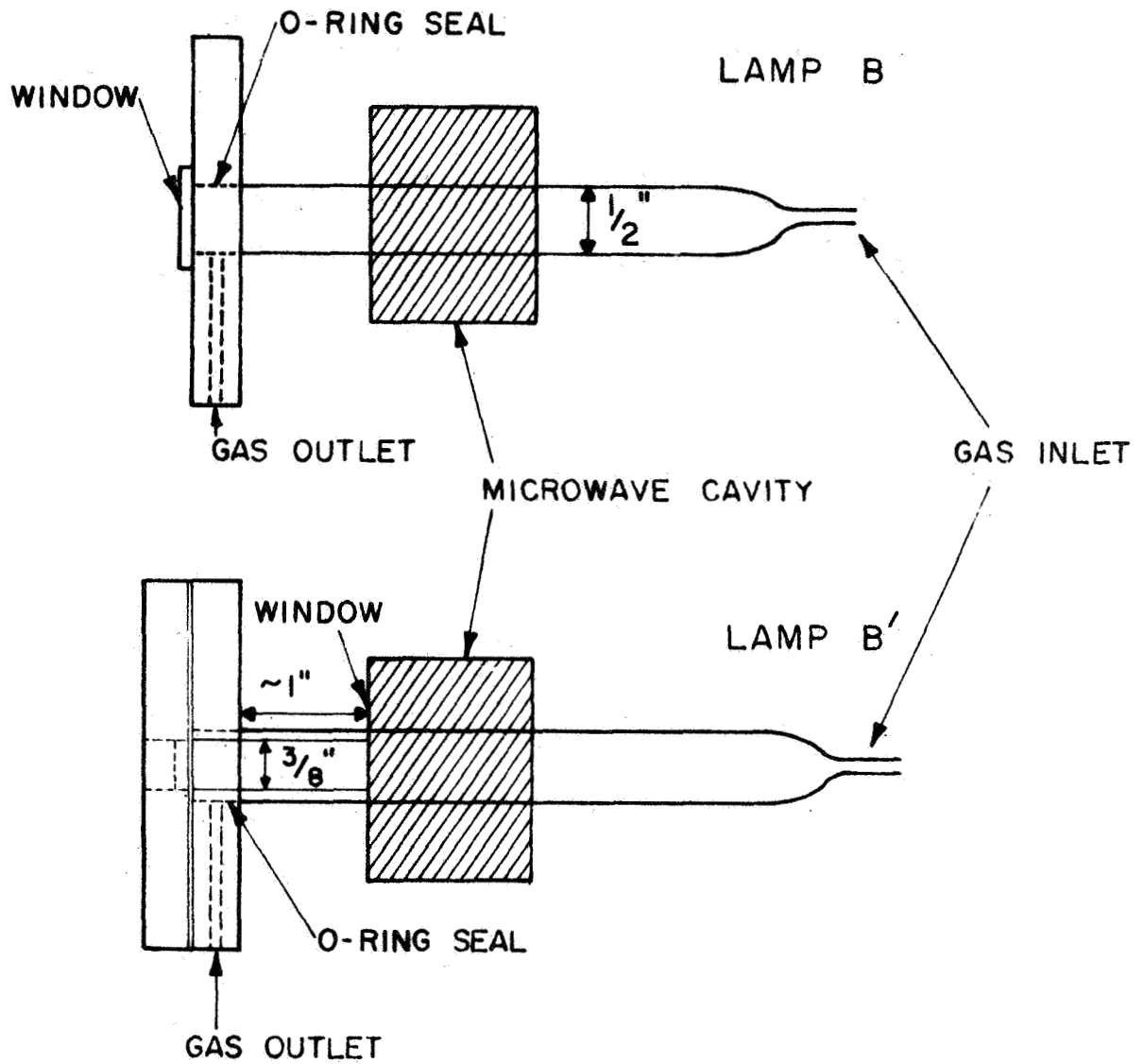


Figure 40. Microwave powered discharge source configuration.

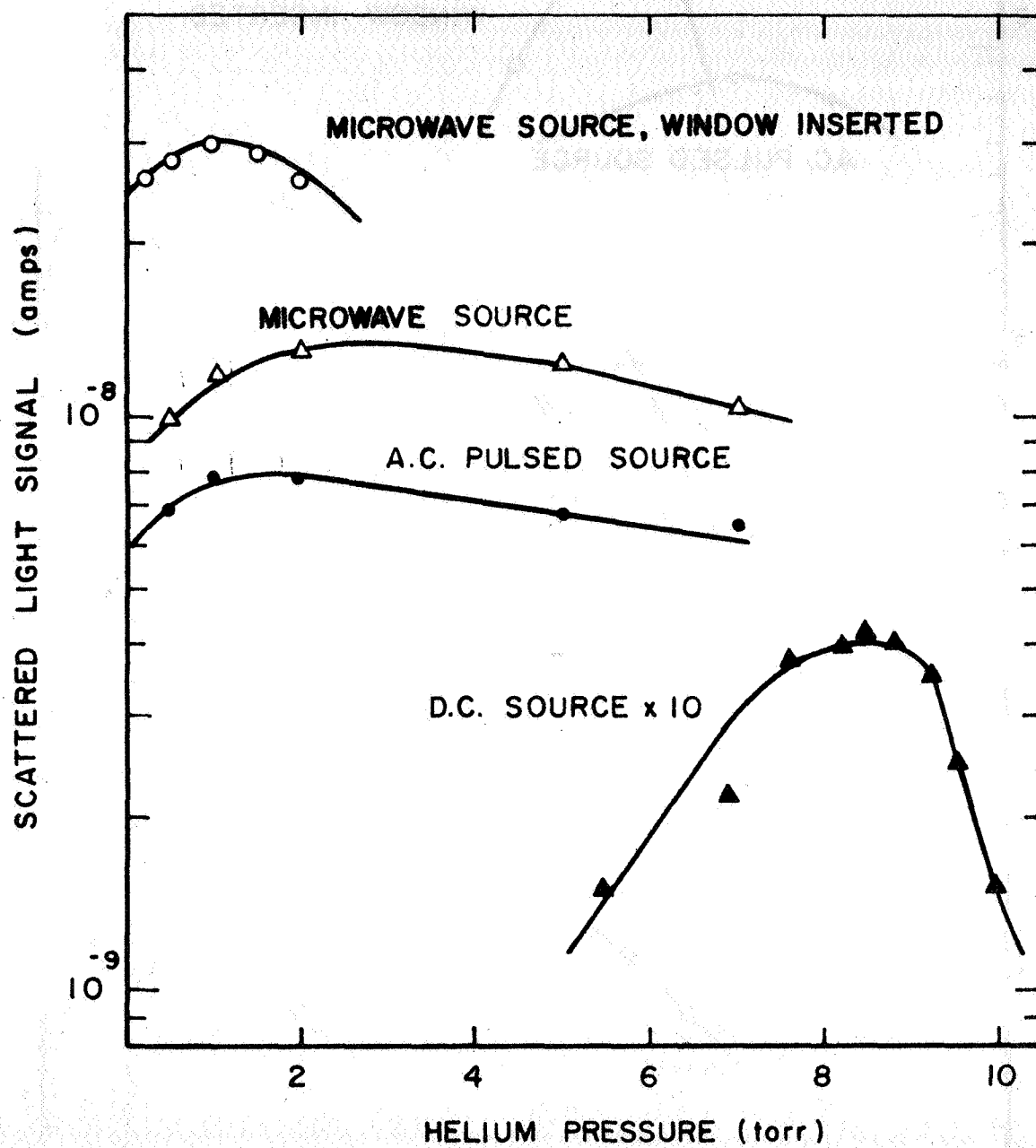


Figure 41. Dependence of observed scattered light signal on the helium pressure in the light sources.

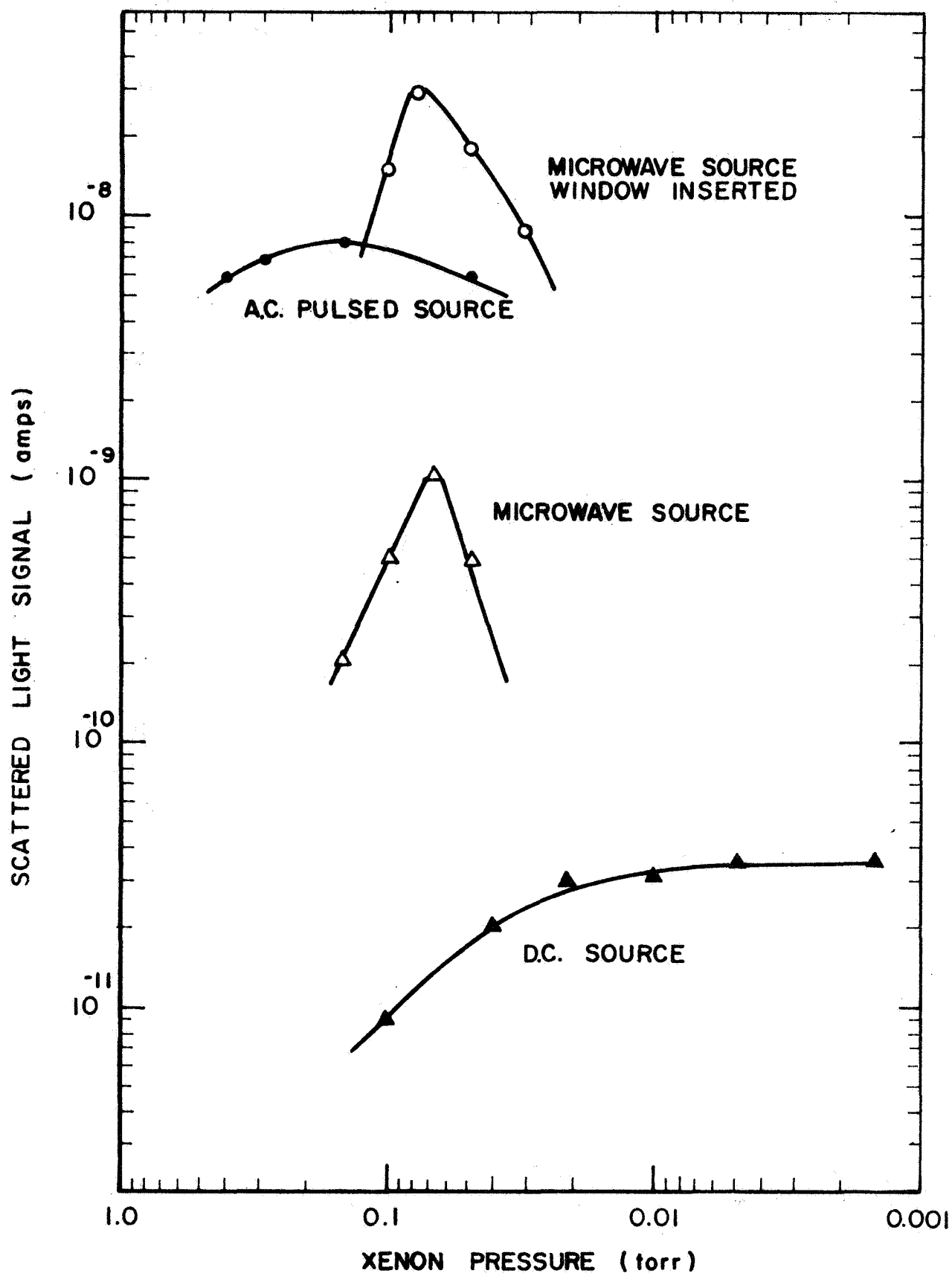


Figure 42. Dependence of scattered light signal on xenon pressure in light sources.

efficient excitation of xenon atoms due to higher current densities available in the first two types of discharges compared with the latter. In this respect it is of interest to note that the insertion of a window close to the microwave discharge increases the effective intensity without change in the optimum xenon pressure. The optimum pressure values for the various light sources are summarized in Table XII.

The effect of the discharge current is shown in Figure 43. For the dc source the intensity increases linearly up to the region where instabilities in the discharge current occur. The microwave light source intensity also shows a linear response with the applied microwave power except at very low power levels where the discharge would be unstable. The ac pulsed source could not conveniently be investigated with respect to current variation, but it was verified that a variation of the spark gap within the limits of operation (1.5 to 5 mm) did not have any effect on the observed intensity.

Although the results shown in Figures 41 and 42 provide already a qualitative indication of the efficiencies of the investigated light source it remained to determine their applicability in quantitative terms. Since a quantitative evaluation had already been made for the dc source studied previously, the effective intensities of the microwave source and the ac pulsed source were simply compared with that provided by the dc source. For this purpose, the individual source parameters were adjusted for maximum observed scattering intensity, and the scattered radiation was observed with the detector operating in the dc mode. The signal response was recorded as a function of the xenon pressure in the scattering chamber, employing the 1 to 1000 xenon-helium mixture to achieve sufficiently low partial pressures of xenon in a convenient manner. The results are shown in Figure 44 in a logarithmic plot. For each light source the observation points are found to lie on a straight line having a slope of unity, thus demonstrating a linear response of the scattered radiation as a function of pressure. The effectiveness of the various light sources increases as follows: dc lamp; ac pulsed source; microwave discharge source with window at flange; and microwave source with window inserted close to the discharge region. Although, the ac pulsed discharge source is more effective than the dc lamp, it is not as powerful as anticipated on account of the more powerful xenon excitation. The most suitable source is, undoubtedly, the microwave discharge source operated with the window close to the discharge region to reduce selfabsorption. Compared with the dc light source, the microwave lamp provides a gain by a factor of 400. Since with the dc source the lower limit detectable xenon pressure was 6×10^{-9} torr, when the EMR photomultiplier in the pulse counting mode was used, the microwave source will reduce this limit to a new value of 1.5×10^{-11} torr. This is clearly low enough to span three orders of magnitude of the ultra-high vacuum pressure domain, thus demonstrating the usefulness of resonance scattering for the calibration of an ionization gauge in the ultra-high vacuum pressure region. However, for a complete assessment of nonlinearities in the response of an ionization gauge in that pressure region it

TABLE XII

OPTIMUM LIGHT SOURCE PRESSURES (torr)

Light Source	Xenon Pressure	Helium Pressure
DC glow discharge source	0.005	8.5
AC pulsed source	0.150	2.0
Microwave discharge source	0.070	3.0
Microwave source with window inserted close to discharge	0.070	1.0

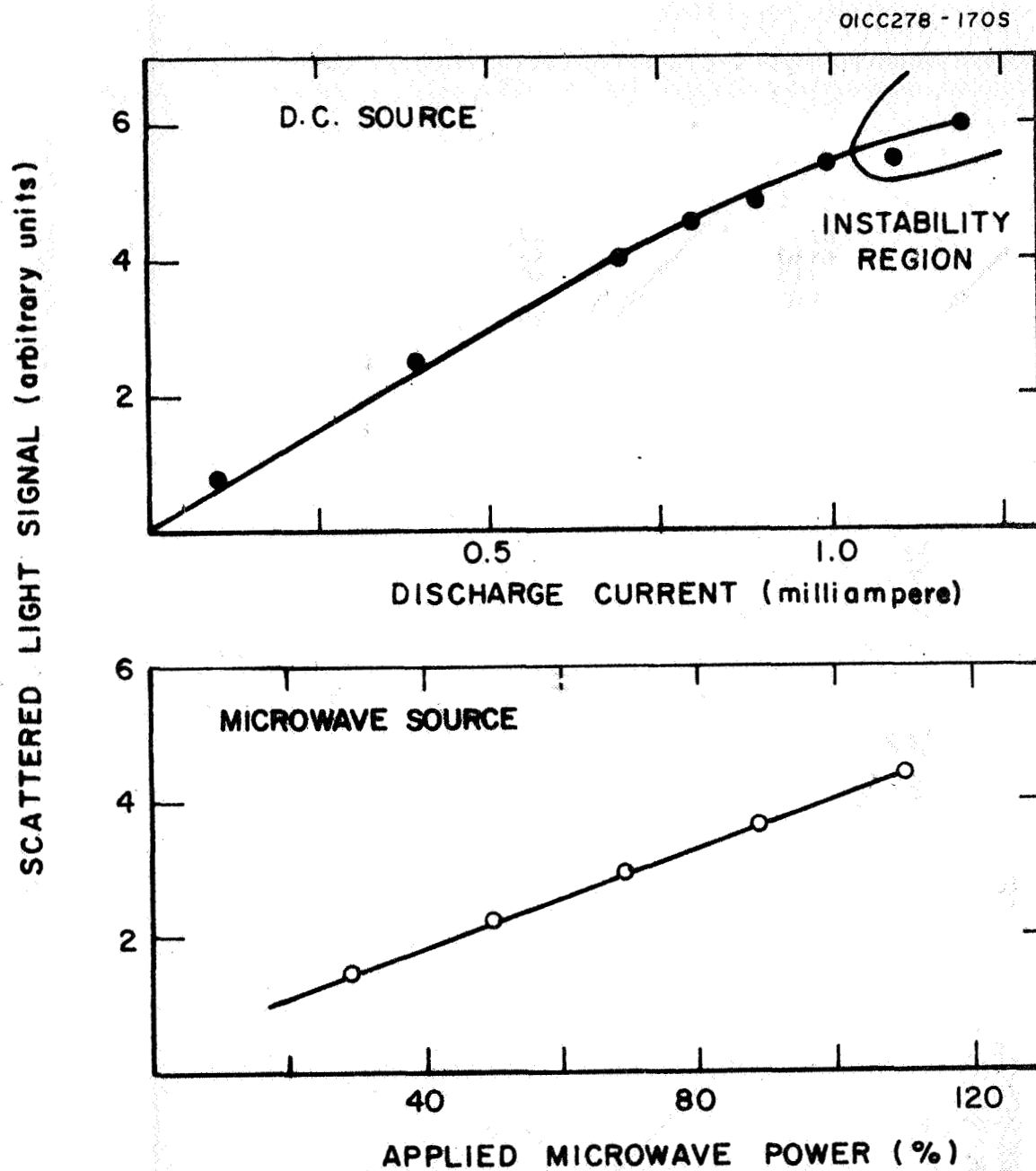


Figure 43. Dependence of scattered light signal on current in dc source, and microwave power applied to microwave source.

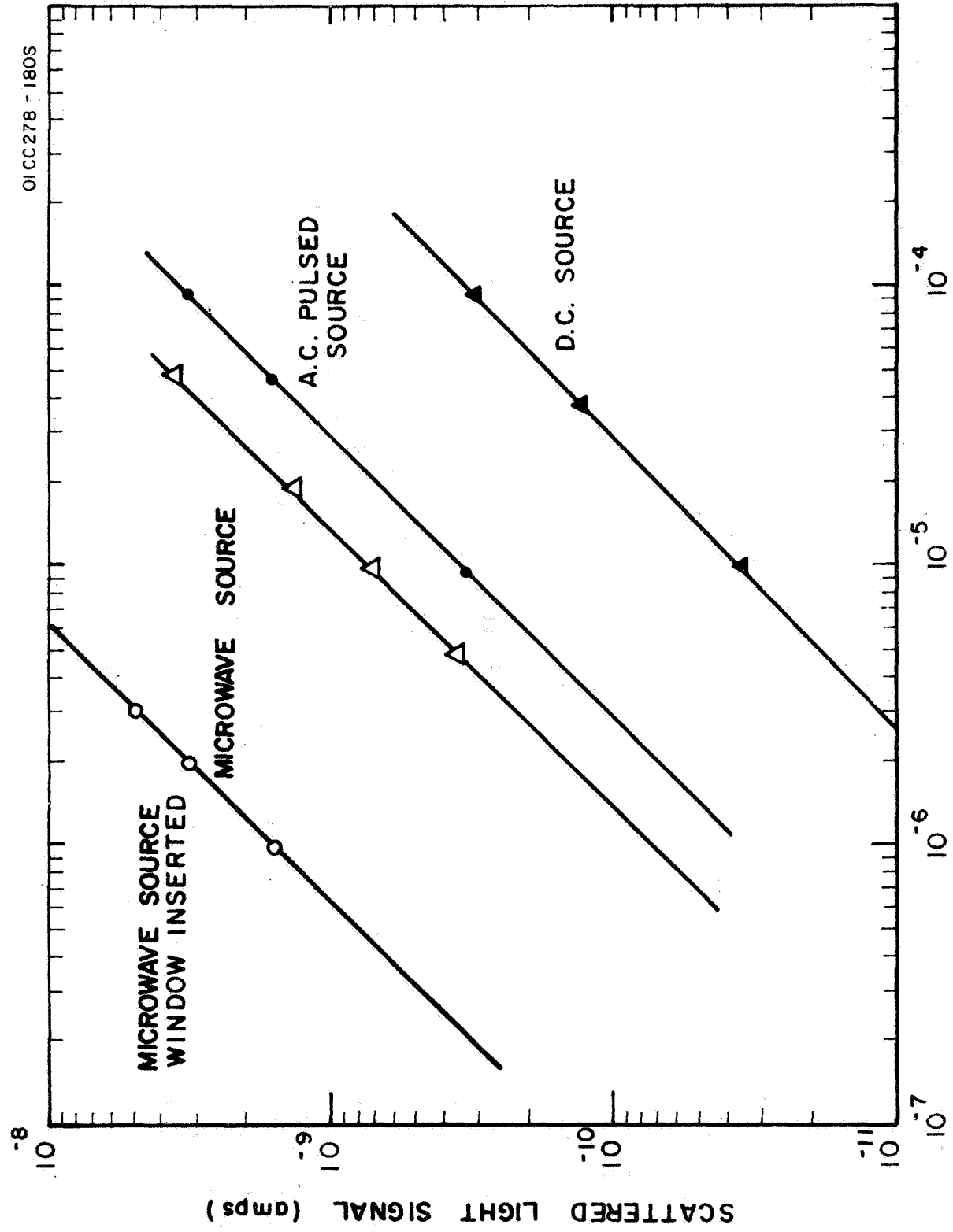


Figure 44. Scattered light signal observed as a function of partial pressure of xenon in the scattering chamber.

may be desirable to go to still lower pressures. In that case a more sensitive detector such as the Bendix Channeltron multiplier must be used.

While these results pertain to the empirical optimization of the employed light sources, it was also of interest to determine the remaining degree of selfabsorption. For this purpose, the line shape of the 1470 \AA emission produced by the microwave source was recorded spectrographically with the 21-foot vacuum spectrograph at the Air Force Cambridge Research Center and compared to a similar recording of the dc source emission. The results are shown in Figure 45 as densitometer traces of the obtained photographic plates. The dispersion is 0.06227 \AA per cm. It should be noted that the photographic process does not produce densities linear with the incident intensities, but rather proportional to the logarithm of the intensity. Thus, the intensity half widths are less than the half widths taken directly from the densitometer trace. It is estimated that the half width of the three lines are 0.065 \AA for the dc lamp, 0.050 \AA for the microwave light source with the window at the flange, and 0.015 \AA for the microwave source with the window placed close to the discharge region. In conjunction with Figure 44 these values demonstrate a decreasing line width with increasing efficiency of the source, in accordance with expectation. Moreover, Figure 45 also shows that the dc source, despite the small partial xenon pressure of 5×10^{-3} torr employed in the source, is still badly selfreversed. For the microwave source the degree of self-reversal is diminished, and it is essentially eliminated when the window is brought close to the discharge region.

7. Conclusions

A comparison of three different xenon light sources: a small dc glow discharge lamp, an ac pulsed capillary source, and a microwave excited light source, has shown that the atomic resonance scattering signal observed for optically thin conditions in the scattering chamber is highest for the microwave discharge source operated with a window close to the discharge region. This source also produces the least degree of selfreversal of the emitted xenon resonance line. A 400-fold improvement is thereby achieved when compared with the dc glow discharge source studied previously. If an EMR uv photomultiplier detector used in the pulse counting mode the lower pressure detection limit of xenon is derived to be 1.5×10^{-11} torr. This value can still be lowered by employing a Bendix Channeltron multiplier. It is estimated that the combination of a microwave light source and a Bendix Channeltron multiplier detector will make possible a lower detection limit of the order of 2×10^{-13} torr. From these conclusions, the application of xenon resonance scattering as a technique for the calibration of ionization gauges in the ultra-high vacuum region appears entirely feasible.

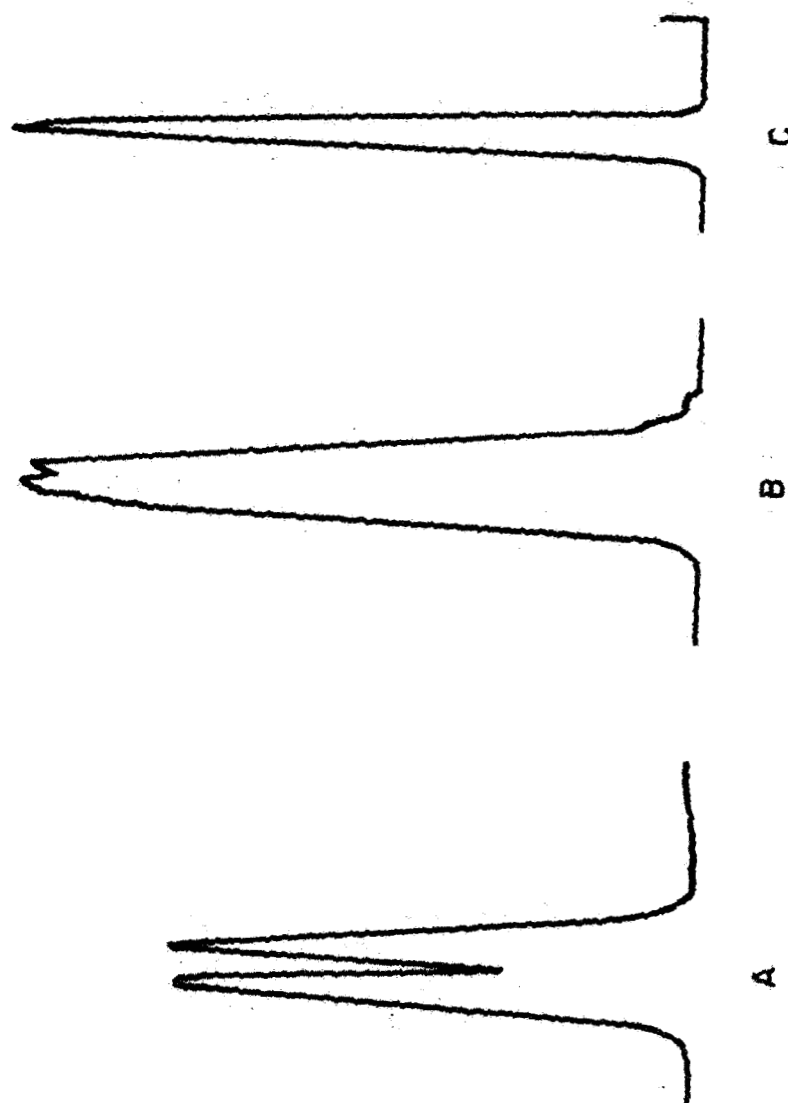


Figure 45. Densitometer traces of 1470 Å emission. A: dc light source, B: microwave source; C: microwave source with window close to discharge region; dispersion 0.06227 Å/cm.

The dc glow discharge source, because of its low intensity is not suitable for the ultra-high vacuum range. Its virtues are, however, low cost, stability, compactness, and ease of operation, so that it would provide a good resonance scattering light source under less stringent requirements. The ac pulsed source is considerably more intensive than the dc glow discharge lamp, but it is less stable, and due to the spark gap operation produces high frequency noise which is a draw back when pulse counting techniques are employed. The microwave discharge has a reasonable stability, and it delivers suitable intensities with a narrow line width. Its operation requires an appropriate microwave generator which is both costly and bulky. The present results indicate, however, that the microwave discharge source is the only one of the three investigated sources that may be suitable for resonance scattering experiments in the ultra-high vacuum range.

REFERENCES

1. Herzog, R.F.K., Poschenrieder, W.P., Satkiewicz, F.G., "Mass Spectrometer Analysis of Solid Materials with the Ion-Microprobe Sputter Source," Final Report, Contract No. NAS5-9254, GCA Technical Report TR-67-3-N (1967).
2. Milne, T. A., Greene, F. T., J. Chem. Phys. 47, 4095 (1967).
3. Narcisi, R. S., "Ion Composition Measurements and Related Ionosphere Processes in the D and Lower E Region," Aeronomy Report No. 10 -- Second Conference on Direct Aeronomic Measurements in the Lower Ionosphere (Dec. 1965).
4. Satkiewicz, F. G., Unpublished data on graphite and silicon carbide.
5. Lindholm, E., in Ion Molecule Reactions in the Gas Phase, Adv. Chem. Ser. 58, 1 (1966).
6. Fehsenfeld, F. C., Evenson, K. M, and Broida, H. P., Rev. Sci. Instruments 36, 294 (1965).
7. Gioumousis, G., and Stevenson, D. P., J. Chem. Phys. 29, 294 (1958).
8. Fehsenfeld, F. C., Schmeltekopf, and Ferguson, E. E., J. Chem. Phys. 45, 404 (1966).
9. Warneck, P., J. Chem. Phys. 46, 513 (1967).
10. Warneck, P., and Myer, J. A., "A Resonance Scattering Technique for Detecting Small Leaks," GCA Technical Report 68-19-N (1968).